IMPRIMATUR

Vu le rapport présenté par le jury d'examen, composé de

Président de la séance publique :	M. le Professeur Christian Kull
Président du colloque :	M. le Professeur Christian Kull
Directeur de thèse :	M. le Professeur Pietro de Anna
Expert interne :	M. le Professeur Niklas Linde
Expert externe :	M. le Professeur Christopher MacMinn
Expert externe :	M. le Professeur Luis Cueto Felgueroso

Le Doyen de la Faculté des géosciences et de l'environnement autorise l'impression de la thèse de
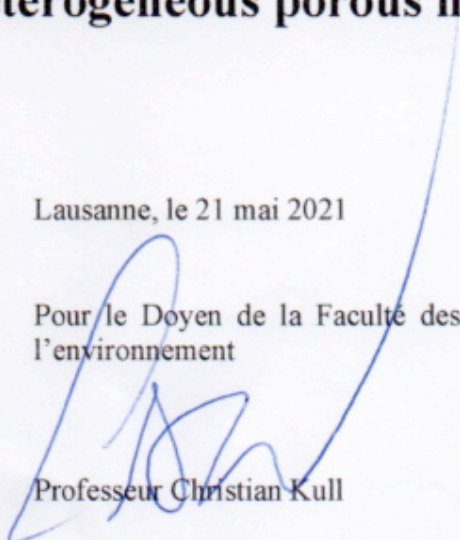
Madame Mayumi Hamada

Titulaire d'un
Master in Environmental Engineering
de l'ETHZ

intitulée

Mixing by confined and heterogeneous porous media

Lausanne, le 21 mai 2021

Pour le Doyen de la Faculté des géosciences et de l'environnement

Professeur Christian Kull

MIXING BY CONFINED AND HETEROGENEOUS POROUS MEDIA

Ph.D. thesis

Faculty of Geosciences and Environment,
Institute of Earth sciences,
University of Lausanne

Mayumi Hamada

Lausanne, May 2021.
Jury composed of:

prof. Christian **KULL**, UNIL Lausanne (President of the jury)
prof. Pietro **DE ANNA**, UNIL Lausanne (Thesis supervisor)
prof. Marco **DENTZ**, CSIC Barcelona (External expert)
prof. Luis **CUETO-FELGUEROSO**, UPM Madrid (External expert)
prof. Chris **MACMINN**, Univ. of Oxford (External expert)
prof. Niklas **LINDE**, UNIL Lausanne (Internal expert)

Acknowledgements

Résumé

Le mélange contrôle de multiples phénomènes naturels et industriels. De manière directe, lors du transport intracellulaire ou des échanges de gaz dans les poumons, ou indirectement, dans des processus entraînés par la rencontre de différentes entités: par exemple, les microbes et leurs nutriments ou les espèces impliquées dans une réaction chimique. Lorsque le mélange se produit dans des environnements confinés, caractérisés par la présence de barrières imperméables, tel que les systèmes poreux, l'organisation spatiale des espèces diffère de celle observée pour des systèmes non confinés. Cette thèse vise à étudier l'impact d'un tel confinement sur l'état et la vitesse du mélange: pour les systèmes poreux, le mélange est contrôlé par l'action combinée de i) l'advection, qui déplace les solutés tout en modifiant la forme de l'interface où les gradients sont distribués, et ii) la diffusion moléculaire, qui lisse les gradients de concentration par transfert fickien de masse. Comme il sera abordé dans cette thèse le confinement a un impact sur ces deux processus.

Nous utilisons la solution analytique de l'équation de diffusion unidimensionnelle pour un domaine spatial de taille fini afin de quantifier l'impact du confinement sur plusieurs mesures de mélange. Nous montrons que la solution dans un domaine confiné avec un flux nul comme conditions aux limites impose une nouvelle échelle de temps, caractérisant le mélange limité par le confinement et contrôlé par diffusion qui est nettement plus court que l'échelle de temps diffusive caractéristique dans un domaine non confiné. Ces observations montrent que le mécanisme d'homogénéisation par diffusion est renforcé par la présence de barrières imperméables.

Dans la seconde partie de la thèse, nous proposons une nouvelle méthode de mesure du coefficient de diffusion d'un traceur basée sur l'évolution spatio-temporelle du champ de concentration du traceur considéré. La mesure consiste à ajuster la solution analytique de l'équation de diffusion au profil mesuré, en prenant explicitement en considération la nature confinée du dispositif de mesure et en utilisant un unique paramètre d'ajustement: le coefficient de diffusion lui-même. La méthode proposée fournit une estimation pour D avec une intervalle de confiance de 3%.

Afin de prendre explicitement en considération le rôle joué par un champs d'écoulement hétérogène, nous utilisons des méthodes expérimentales (microfluidique, microscopie avec prise de vue à intervalles réguliers) ainsi que des simulation numériques afin d'étudier le transport par écoulement laminaire. Nous montrons que les modèles récents développés pour décrire le mélange d'un soluté transporté par des champs d'écoulement hétérogènes dans un milieu continu (ne tenant pas compte

du confinement) ne permettent pas de prédire nos observations à l'échelle du pore. En particulier ces modèles reposent sur l'hypothèse que le mélange est localement contrôlé par la diffusion dans un domaine non confiné qui, comme nous l'avons démontré dans cette thèse, est quantitativement et qualitativement différent de ce qui est observé dans les espaces confinés. Ce résultat démontre la nécessité de développer un modèle de mélange à l'échelle du pore qui tienne compte à la fois des barrières solides et imperméables et de cinématique locale de l'écoulement qui régit l'étirement local du fluide.

Abstract

Mixing controls a plethora of natural and industrial phenomena. Directly, as intracellular transport and gas exchange in the lungs, or indirectly, in processes that are driven by the encounter of different entities: e.g., microbes and nutrients or species involved in chemical reactions. This thesis focuses on the impact of physical confinement on mixing dynamics: for porous systems, mixing is controlled by the combined action of i) molecular diffusion, that smear these gradients by Fickian mass transfer and ii) advection, that displaces solutes modifying their interface where gradients are distributed. Confinement impacts both these processes as shown and discussed in this thesis.

We use the analytical solution of a one-dimensional diffusion equation for a finite spatial domain to quantify the impact of confinement on several mixing measures. We show that the solution in a confined domain with no-flux boundary conditions imposes a new timescale characterizing confinement-limited mixing controlled by diffusion which is significantly shorter than the characteristic diffusive timescale in an unconfined domain. These observations indicate that the diffusive homogenization mechanism is enhanced by the presence of impermeable boundaries.

Then, we propose a novel method to measure the diffusion coefficient D of tracers, based on the spatio-temporal evolution of the concentration field of the considered tracer. The measurement consist in fitting the analytical solution of the diffusion equation to the measured profile, taking into explicit consideration the confined nature of the setup and having as sole fitting parameter the diffusion coefficient itself. The proposed method provides estimation for D with uncertainty down to 3% and it has been validated with a tracer of known D.

To take into explicit consideration the role played by heterogeneous advection, we use experiments (microfluidics, time-lapse video-microscopy) and numerical simulations to study solute transport by laminar flow. We show that recent models developed to describe mixing by heterogeneous and continuous flow fields (neglecting confinement) fail to predict our pore-scale observations. In particular, the building block of these models lies on the assumption that locally mixing is controlled by diffusion in a unconfined domain that, as we demonstrated in this thesis, is quantitatively and qualitatively different from the one taking place within confined spaces. This result indicates that pore-scale models for mixing must consider the presence of solid impermeable boundaries and the detailed flow kinematics that governs the local fluid stretching.

Contents

Chapter 1

Introduction

1.1 Porous media structure and flow heterogeneity

Water flowing through the subsurface originates from various sources such as rainfall precipitations, snow melt or bed seepage from rivers and open-water reservoirs. It travels through a succession of solid matrix typically porous or fractured media (Fig. 1.1.a.). While fractured media are typically consolidated and low permeability rocks that underwent fracturing due to natural (e.g. seismic) or induced (as fracking) stresses, porous media are composed of aggregated materials, often sediments, separated by void spaces, also called pores. Flowing water naturally contains dissolved or suspended compounds, that are either inert and thus passively transported or they can react between them or with the solid substrate. It is in the pore space that transport and mixing processes occur controlling chemical and biological reactions such as ion-exchange, dissolution and precipitation, bio-mineralization or biofilm growth. Figure 1.2.d. shows an example of biofilm development in the pore space.

Natural substrates exhibit a wide spectrum of pore sizes λ with typical values ranging between $10^{-6} - 10^{-2}$ m [2]. The amount of water that can be stored in the pore space is defined by the porosity of the host medium:

$$\phi = \frac{\text{volume of pores}}{\text{total volume of solids and pores}} \tag{1.1}$$

which spans from few percent in some metamorphic rocks up to 70% in clay deposits [3, 4]. Subsurface layers, often classified as a function of their saturation degree, are distinguished between: the *vadose zone* where pores are filled with both air and water, and the *saturated zone* where the pore are filled with water only (Fig. 1.1.b.). Usually water in the saturated zone is referred to as

groundwater [3, 5]. In porous media, such as soils or sediments, the solid matrix is composed of grains (made of organic and/or mineral material) more or less packed together. The heterogeneity of the grain size distribution heavily impacts porosity value ϕ: as illustrated in Fig. 1.2.b. poorly sorted deposits typically results in low porosity while well sorted material in higher values [3].

Very often, grains themselves are porous (Fig. 1.2.a.) and their own porosity is negligible with respect to the one of the ensemble [8, 9]; in some other scenario it increases the total porosity of the deposit [10]. Solutes and organic material diffuse into individual grains due to the concentration gradient between pore and intragranular water. It has been shown that for sorbing / reacting materials the intragranular surface represents a significant fraction of total reaction site available, leading to a stronger dispersion with respect to non-reactive solutes [10, 9].

At macroscopic scale the average flow velocity value can vary from 10^{-6} (e.g. crystalline rock) to 2 m/day (e.g. gravel) [3] depending on the substrate type. Those values are much smaller than the one observed in turbulent systems, typically of the order of 1 m/s [11]. Traditionally flow is classi-
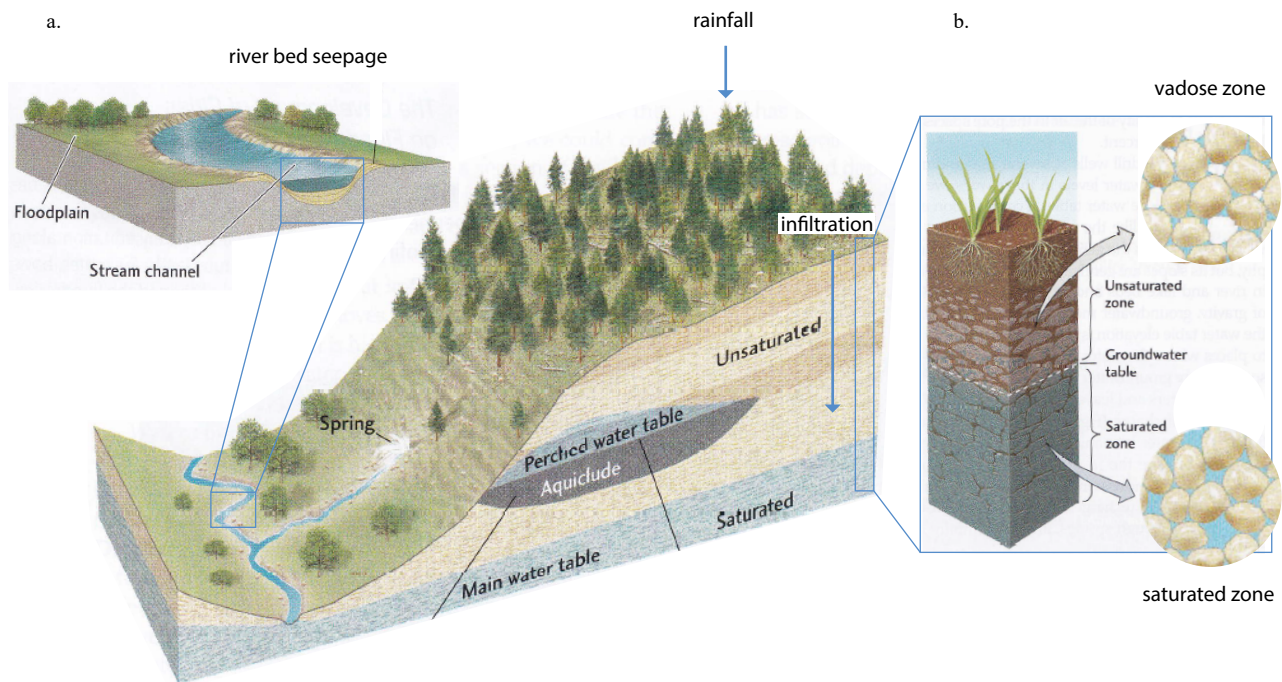
Figure 1.1: *a*. Example of water pathway to the subsurface: rainfall infiltration and river bed seepage, once it has reached the subsurface water travels through the saturated and unsaturated zone. *b*. Porous medium is a typical subsurface substrate, it is composed of an ensemble of *grains* more or less packed together, the void between the grains is called the *pore space*. In the vadose zone pores are filled with both air and water, in the saturated zone with water only. Figure adapted from [1]

fied between laminar regime, where viscous forces dominates with respect to inertia and turbulent one in which inertia is more important. The ratio between viscous and inertial forces driving fluid motion is quantified by the Reynolds number $Re = \rho \bar{u} \lambda / \mu$, with $\bar{u}$ the flow velocity magnitude, ρ and μ the fluid density and viscosity. Laminar flow regimes, typical for porous media flow, are characterized by low Reynolds number $Re < 10^{-1}$ and thus exhibit low flow velocity and small characteristic length λ. Therefore in confined media fluid motion is bound by the host matrix structure and solute transport by the impermeable boundary it imposes. **In the following we define confined media as systems in which the host medium sets the characteristic scale of fluid flow and mass flux**. Recently developed technology, such as X-ray tomography [12] or microfluidics [13, 14, 15] and numerical schemes [16] allowed researchers to study flow structure at microscopic scale. They show that fluid transported through such heterogeneous material experiences flow velocity values that spans over several order of magnitude and variations are observed at the sub-millimeter scale and
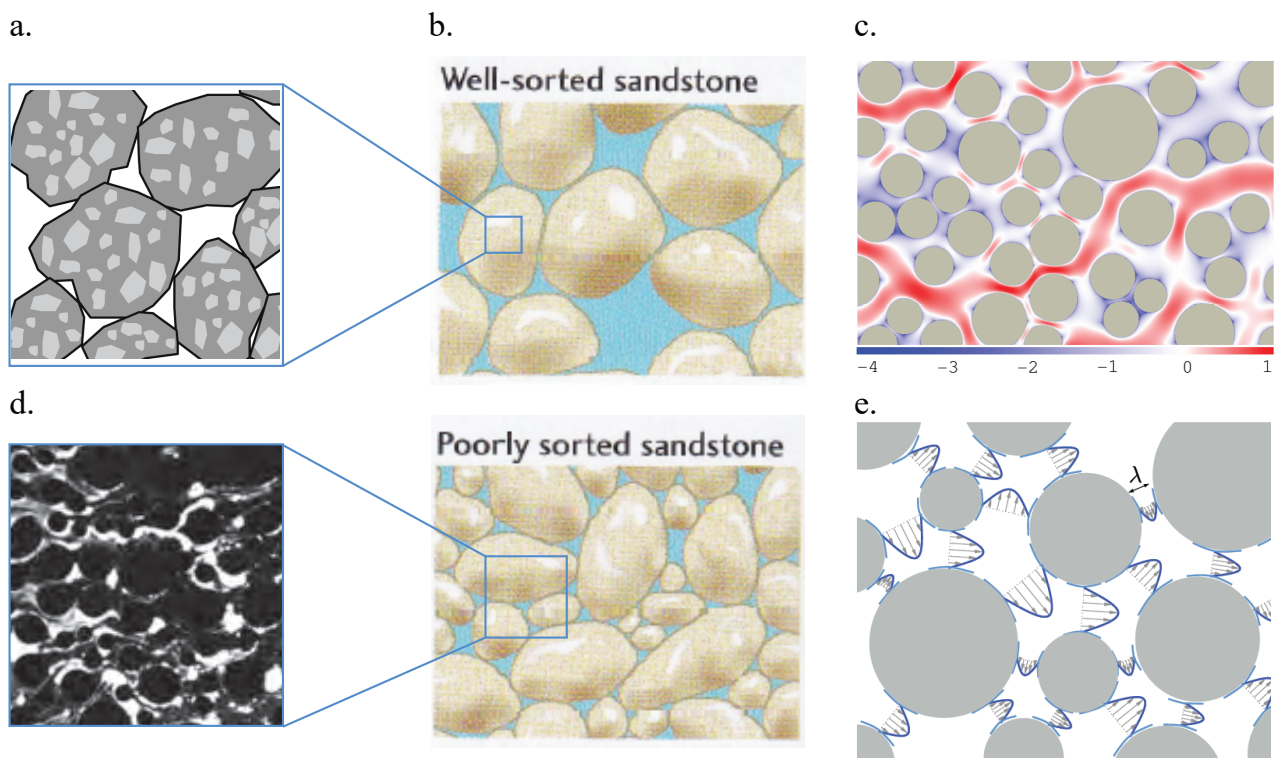
Figure 1.2: *a*. Intragranular porosity provides reaction sites for ion-exchange, species access inner grain area by diffusion, it can also contribute to the total porosity (adapted from [6]); *b*. Porosity value is highly dependant on grain size distribution, narrow distribution is characteristic of high porosity, while large variability of grain sizes leads to a lower porosity (adapted from [1]); *c*. Simulated velocity field magnitude rescaled by the average velocity $\bar{u}$ is shown in a logarithmic scale log10(u/u): in white $u = \bar{u}$, in red $u > \bar{u}$ and in blue $u < \bar{u}$ (adapted from [7]); *d*. Pore space colonized by *P.Putida* bacteria, fluorescent microscopy image; *e*. Conceptual model of porelet: each pore throat has a velocity field with a parabolic profile, as in a tube (adapted from [7]).

for very low Reynolds number [17, 18, 19, 20, 21]. Figure 1.2.c. shows, in a logarithmic scale, a numerical simulation of a pore-scale velocity field magnitude, in this case the computed velocity spans over five orders of magnitude. Micro-scale heterogeneity of the flow field has a dramatic impact on numerous subsurface phenomena such as solute transport and mixing [22, 23], distribution of the electrical conductivity field [24], reactive transport [25], filtration [26], oxygen distribution [27], bacteria growth and motility [15, 28] or biofilm architecture [29].

Complexity of flow pattern increases when fluids of different phases, viscosity or density coexist: this plays a critical role in an extensive range of processes such as water infiltration [30], displacement of aqueous and non-aqueous phase pollutant [31, 32, 33, 34], chemical reaction rates [35] or methane [36, 37] and CO_2 [38] migration. In several of these examples the presence of different fluid phases can trigger time-dependant flow patterns.

The thesis aims to study the role of confinement on transport and mixing dynamics, to do so in a systematic and rigorous way we consider a simplified view of porous medium diversity exhibiting only the features that characterize confinement. Therefore, the processes approached in this thesis are described for systems where the pore space is fully filled with water, usually referred to as **saturated flow conditions**, the porous medium matrix has **impermeable grains** and the flow field is invariant in time, referred to as **steady state flow**.

1.1.1 Darcy scale

The basic equation governing groundwater flow is given by the Darcy's law [39] which states that the flow rate through a porous medium Q is proportional to the the headloss Δh divided by the length of the flow path L also called the hydraulic gradient:

$$Q = -K A \frac{\Delta h}{L}, \tag{1.2}$$

where K, the hydraulic conductivity, has unit of m/s and is a property of both the medium and the fluid, A is the cross-section area of the domain considered and δh the difference of water elevation between two observation wells separated by a distance L. The hydraulic conductivity defines the ease of water to move through a porous or fractured medium: the diversity of substrate in the subsurface offers a wide range of hydraulic conductivity values from 10^{-13} to 1 m/s [3]. We define an average flow velocity over the domain, the Darcy velocity, as $q = Q/A$ in m/s. The hydraulic conductivity K has been shown to be related to intrinsic permeability k, a property of the medium

only, through $k = K \mu / (\rho g)$ [4] with g the gravitational acceleration.

This formulation has been extended [2] to describe heterogeneous flow systems in which at each location x the fluid velocity $\vec{q}(x)$ is proportional to the local pressure gradient $\nabla p(x)$ through an effective medium permeability $k(x)$. For a given set of physical boundary conditions, the pressure p, related to the hydraulic head through $p = \rho g h$, can be numerically solved in terms of mass balance and the fluid velocity derived from the extended Darcy law.

Within this framework the scale at which the system is resolved assumes a Representative Elementary Volume (R.E.V) over which host medium properties, such as porosity and permeability, are considered homogeneous enough to be represented by an averaged value. This assumption is valid for studies considering averaged flow properties, however in many cases it oversimplifies the description of flow pattern and, as mentioned in the previous section, leads to wrong predictions for processes that depends on local velocity values.

The porous medium structure and morphology are lumped into the definition of a permeability field for which heterogeneity and correlation degree is set a priori. However, it is defined for a continuous domain, and so is the derived flow field: the intrinsic pattern of pore space and grains organization is therefore lost. In particular, description of continuous flow field cannot consider the no flow and no flux conditions prevailing around the grains of the matrix. **The work presented in this thesis aims to investigate the effect of such obstacles on solute diffusion and mixing processes.**

1.1.2 Pore scale

Taking into account the presence of solid obstacles one must solve the flow velocity field at the scale that specifically considers zero flow velocity, in other words no-flow (or no-slip) boundary conditions, at the water-grain interface: from now on we will refer to that as the pore scale. In this framework, flow equations are set in terms of momentum and mass conservation, for Newtonian fluids they are formulated by the Navier-Stokes equations [2] a set of partial differential equations where inertia is balanced by the sum of forces acting on a fluid particle. For fluid flow characterized by low Reynolds number, i.e. dominated by viscous effects ($Re < 1$), inertia can be neglected and the formulation reduces to the so called Stokes equations:

$$\nabla p = \mu \nabla^2 \vec{u}. \tag{1.3}$$

The above expression is valid for an horizontal plane, thus neglecting gravity, with $\vec{u}$ the local velocity.

Stokes equations can be analytically solved for the case of flow in a single tube of radius R, referred to as Hagen-Poiseuille flow, the symmetry of the problem along the main flow direction reduced Eq. (1.3) to an integrable form. The solution defines the characteristic parabolic profile:

$$u(r) = \frac{\nabla p}{4\,\mu}\,(R^2 - r^2), \tag{1.4}$$

with v the fluid velocity along the tube radius. Velocity is maximum at the center of the tube and zero at the tube walls ($r = R$). This simple parabolic profile actually describes also the flow profile within a single pore throat, as schematically represented in Fig. 1.2.e.

Starting from this observation, novel approaches led to a new family of models, called pore-network models, where the flow field breaks down to an ensemble of flow within tubes whose average is controlled by the tubes radius distribution and their connectivity [40]. Following the same approach a recent study [21] modeled low velocities in a porous medium as a collection of parallel pores, the porelet, in which Poiseuille flow is solved. It has been shown that the distribution of low velocities is controlled by the distribution of the pore size, directly linking flow heterogeneity to the medium structure. Figure 1.2.e. illustrate the concept of porelet and its characteristic parabolic profile.

1.2   Solute transport

Within the context of porous media dissolved and suspended compounds are transported through two main physical mechanisms: advection, where the mass is transported *with* the fluid at moving velocity v and diffusion where the mass is transported *through* the fluid by the random motion of compound molecules due to thermal agitation. Transport measurement and modelling aim to determine the spatio-temporal dynamics of a concentration $c(x,t)$, defined as the mass of solute per volume of fluid in [kg/m^3], in a given flow field, it have been used to monitor and asses underground physical properties such as permeability, pore or fracture size orientation and connectivity [23, 41] as well as to study processes such as mixing [42, 43] or infiltration [44, 45].

We defined in the previous section the different flow description used to model the velocity field in

porous media. We will now describe the second mechanism of transport: diffusion.

Diffusion

Molecular diffusion of a given dissolved or suspended compound originates from the individual molecules (or particles) motion that is associated to their thermal agitation, as observed by Brown for the motion of pollen [46]: the macroscopic consequence of this microscopic phenomenon is that the mass of that compound spreads in space as time passes.

The detailed description of molecular diffusion in terms of a mechanistic and physics-based model, was revealed independently by Einstein [47], von Smoluchowski [48] and Sutherland [49] who show that the thermal agitation of molecules results in a random walk whose statistics is reflected by the first Fick's law describing the macroscopic mass flux. This statistical and physics-based model of random walk can be summarized as follows. The system is composed by a large number of molecules (or particles) that:

1. step every τ with a velocity v at a distance $\delta = v \tau$;

2. the direction of each jump is equally probable (for isotropic diffusion);

3. the motion of each molecule (or particle) is independent on the others.

The velocity v can be related to the kinetic energy and the system temperature as $E = \frac{1}{2} k T = \frac{1}{2} m v^2$, where k is the Boltzmann constant (expressed in [J/K]), m is the mass of the individual molecule (or particle, expressed in [kg]) and T the absolute temperature (expressed in [K]). It is possible to show [50] two main properties of such a defined system. The first is that the average displacement of an ensemble of particles undergoing these three rules (the ones defining a random walk [51]) is zero at all times (after any number of steps), in other words the center of mass is not changing. Then, the second centered spatial moment after n steps scales as $n \delta^2 = 2Dt$, where $t = n \tau$ and $D = \frac{\delta^2}{2\tau}$ is a constant fixed by the system properties (molecule/particle size, but also fluid viscosity and temperature) and it has units of [m^2/s].

Considering the kinetic energy associated to the thermal agitation of molecules/particles and the viscous drag they experience moving within a fluid of viscosity μ, it has been theoretically estimated the value of the diffusion coefficient in terms of the well-known Stokes-Einstein relation [53]. For spherical objects of radius r it reads:

$$D = \frac{k T}{6 \pi \mu r}. \tag{1.5}$$

From these microscopic rules for the motion of each individual molecule (or particle) composing the diffusing substance, it is possible to compute its mass flux $J(x)$ at location x as the difference between the number N of particles moving from a location to the next one passing through the surface A in a unit time as:

$$J(x) = \left(\frac{N(x)}{2} - \frac{N(x+\delta)}{2} \right) \frac{1}{A\tau} = -\left(\frac{c(x+\delta)}{2} - \frac{c(x)}{2} \right) \frac{\delta^2}{2\tau} = -D\frac{\partial c}{\partial x}, \tag{1.6}$$

where we introduced the concept of substance concentration c, as the number of molecules (or particles) per unit volume $c = N/(A\delta)$, and we approximated the first spatial derivative (gradient) at first order. Equation (1.6) is the well-known first Fick's law that describes the macroscopic mass transfer, stating that the diffusive mass flux is locally proportional to the concentration gradient. The negative sign implies that mass moves from locations with higher concentration towards areas of lower concentrations.

There are two main consequences of the first Fick's law. First, in case of an homogeneous con-

a.
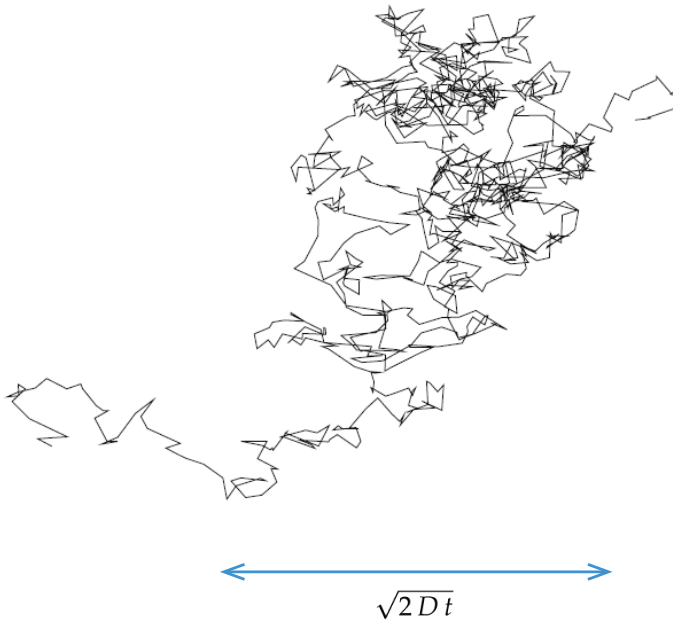
b.
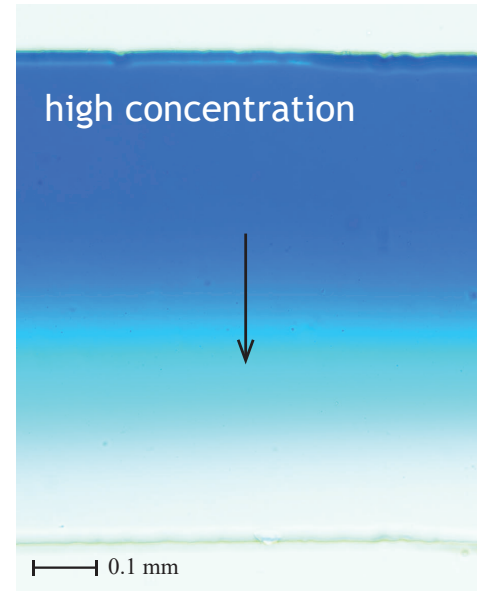
Figure 1.3: *a*. Diffusion at microscopic scale: trajectory of a particle experiencing Brownian motion, random displacement of the particle due to thermal agitation, the center of mass is invariant in time and the variance of the displacement after n steps is given by $\delta = \sqrt{2Dt/n}$ with D the diffusion constant (adapted from [52]); *b*. At macroscopic scale: microscopy image of a tracer diffusing front in a rectangular cross-section channel, mass is displaced towards low concentration area until the system reach homogeneity, black arrow indicates the direction of the mass flux, the temporal evolution of the concentration is given by Fick's law Eq. (1.8).

centration distribution in space, there is no mass flux: this means that even though the individual molecules (or particles) are moving due to thermal agitation, the net effect of their motion is not detectable since it does not produce any change in the overall mass distribution. Second, if there is a concentration gradient different from zero, a non-zero mass flux takes place: thus, the substance concentration changes also over time. To capture this dynamics it is necessary to invoke the substance mass conservation that can be expressed as:

$$\frac{\partial c}{\partial t} = -\nabla \cdot \vec{J}, \tag{1.7}$$

which is known also as the second Fick's law: to every spatial change in mass flux is associated a temporal change in concentration. In other words, if the concentration at location x varies, this is due to a spatial variation in mass flux (mass that leaves or joins the location x). Combining the two Fick's laws we obtain the well known diffusion equation describing the spatio-temporal distribution of a diffusing substance:

$$\frac{\partial c}{\partial t} = -D \, \nabla^2 c. \tag{1.8}$$

Knowing the value of D is very important to describe the fate of a diffusing substance and all the diffusion-related phenomena, like mixing or reactions. **We will discuss a novel experimental method to determine its value in Ch.3**.

Transport equations

Considering advection and diffusion at the pore scale the spatio-temporal evolution of a solute concentration $c(x, t)$ in a flow field $\vec{v}$ is controlled by mass conservation principle, Eq. 1.7, where the mass flux is given by the sum of an advective term $-\vec{v} \cdot \nabla c$ and a diffusive one $D \, \nabla^2 c$ as expressed by the well-known advection-diffusion equation [54, 2]:

$$\frac{\partial c}{\partial t} = -\vec{v} \cdot \nabla c + D \, \nabla^2 c, \tag{1.9}$$

with D the molecular diffusion coefficient. The ratio of advection and diffusion effects is quantified by the Péclet number $Pe = \lambda \, \overline{v} / D$ with λ a characteristic length of the system considered (e.g the average pore size) and $\vec{v}$ the average flow velocity at the scale considered. Typically systems characterized by high Pe are controlled by advection, while a small Pe describes diffusion dominated situations.

Describing transport at the larger scale, it is not possible to resolve the detailed structure of the

grains organisation while also capturing the porous system heterogeneity across a wide range of spatial scales. Thus, the discrete and confined structure of the host medium is replaced by a continuous permeability field and the solute spreading around the mean position of its front is described by an effective dispersion coefficient $D^\star$ that lumps together the effects of molecular diffusion and velocity contrasts. In this effective framework and for a homogeneous porosity the mass flux $\vec{J}$ is given by an advective Darcy term $\vec{q} \cdot \nabla c$ and a dispersive one $D^\star \nabla^2 c$ leading to the well-known advection-dispersion equation (ADE) [54, 2]:

$$\frac{\partial c}{\partial t} = -\vec{q} \cdot \nabla c + D^\star \nabla^2 c. \tag{1.10}$$

Also in this scenario a Pe number can be defined as $Pe = \lambda \, \bar{q}/D^\star$ where λ is the correlation length of the permeability field and $\bar{q}$ the average Darcy velocity. This upscaled and macroscopic picture proved to capture well average properties of transport such as breakthrough curves and concentration profiles, but it fails to describe phenomena that depends on small scale concentration values as chemical reactions or biological activity, which depend on the ability of the system to bring compounds close enough to interact: the mixing process.

1.3   Mixing

Mixing in porous media is relevant for numerous processes that involve passive or reactive transport: such as contaminant transport [5], remediation of contaminated aquifer [55, 56, 57], groundwater age determination [58, 59] or biofilm growth and bacterial colonization [60].

In a more general context, mixing is the result of mass transport and it is defined as the ensemble of processes that brings, originally segregated substances, within the same volume [61, 62] by smoothing concentrations, dissipating gradients [63] and increasing the system entropy [64]. The key mechanisms controlling mixing in liquid systems are: i) advection, transport by the surrounding fluid motion and ii) molecular diffusion, random displacement due to thermal fluctuation, which tends to smooth concentration gradients [65, 66].

Mixing dynamics are connected to the observation support scale, defined as the size of the domain for which medium properties and variables of interest values are considered. In the subsurface the heterogeneous flow field spreads the transported solutes by contrast of velocities and typically, interactions between heterogeneous advection and diffusion is lumped into an effective dispersion

coefficient to describe solutes spreading, considered as a proxy for an effective mixing [67, 68, 69]. However, spreading, resulting from the processes that modify the spatial extend of a concentration field, is not mixing and so models based on dispersion measures proved to over predict the degree and rate of mixing [70, 71]. It has been shown that small scale velocity fluctuations control mixing in both confined media [65, 72, 63, 33, 73] and open-flow systems [74]. Other studies proved that such property of porous media flows is responsible for the so called anomalous transport, characterized by non-Fickian dispersion or long temporal tailing of breakthrough curves [68, 69, 43].

The question of support scale is particularly relevant when considering processes involving chemical or biological reactions: the species must be mixed at their own scale for the reaction to happen and information about mixing state at such micro-scale cannot be solved when considering bulk medium properties and effective dispersion coefficient. Figure 1.4 gives examples, visualized at two different scale of reactive fronts displacing in porous media: they illustrate well that the product formation is not homogeneous within the pore space. Figure 1.4.a. shows the concentration field
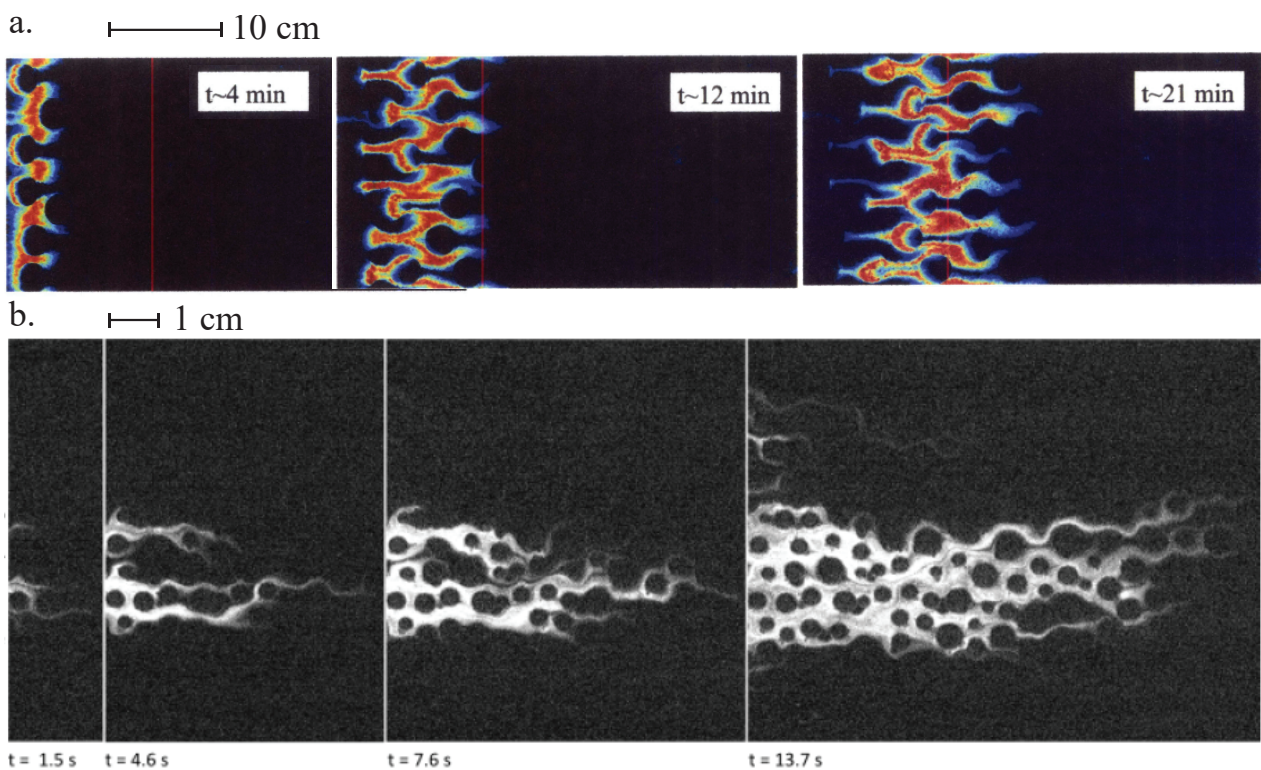
Figure 1.4: *a*. Reactive front from a chemi-luminescent reaction displacing in a stokes flow field, light intensity is a measure of mass of product, we note that product is heterogeneously distributed within pores; *b*. Darcy scale visualization of a reactive front displacing in a heterogeneous porous medium; product concentration increases from black to red; the transverse average of product, as computed in classical ADE models, cannot represent the pore-scale value (adapted from [75]).

of the reaction product between an invading reactant and a resident one [75]. The host medium is composed by fine glass beads (the pore space is too small to be visualized) with enclosures of even one among which flow is stagnant. The authors show how while ADE reproduces well the macroscopic (observed) transport of the invading reactant, it overpredicts the amount of reaction product wrongly assuming an advanced degree of mixing at the pore level. Figure 1.4.b. shows the light emitted by a chemi-luminescent reaction between an invading and a resident solute. The pore space is fully resolved and we observe that the reaction product (the light) is heterogeneously distributed at the micro-scale. The reactive front has a complex topology and dymanics that depend on the detailed interplay between pore-scale advection and molecular diffusion.

The problem of pore-scale flow heterogeneity, incomplete mixing and its impact on reaction rate is the topic of extended studies since the last 30 years, boosted by the constant development of laboratory and numerical tools that allows to dive progressively within the micro-scale world. In homogeneous geometries several studies considering transverse [71, 76] and longitudinal [77, 25] mixing-controlled reactions showed that ADE framework for the macroscopic description of concentration fields overestimates the amount of product due to the prevailing non well-mixed conditions at pore-scale. In [71] the authors investigated the effect of grain size on mixing, in [76] they used the concept of dilution as a measure of mixing and quantified its effect on reaction rates, in [77, 25] they measured the reaction rate product of a bimolecular reaction and confront it with the prediction of models assuming well-mixed conditions. For heterogeneous porous medium structure, similar studies demonstrated that the micro-scale velocity fluctuations observed within the pore space induce local stretching dynamics that triggers persistent concentration gradients, which leads to a faster reaction rate, but smaller amount of reaction product, compared to the predictions made for a continuous domain [78, 79].

1.4 Heterogeneous advection induces complex stretching kinematics

To characterize the stretching mechanism in a heterogeneous flow field let's consider the concept of lamella. Originally developed to define folding and stretching of a concentration blob in a turbulent flow field [80, 81], it was later applied to describe mixing in laminar flow systems [82, 72] leading to the development of cutting-edge models for mixing in porous media [22].

A lamella is defined as a strip of concentration, aligned with the flow direction, of width $s(t)$ and

length $l(t)$ (Fig. 1.5.b.). The strip is displaced by advection and because different points on the strip move at distinct speed, the lamella experiences stretching in the longitudinal direction and, to conserve its volume, compression in the transverse one. Considering diffusion, which tends to spread the strip along its own transverse direction, we can describe the dynamics of the lamella width $s(t)$ as a balance between compression and diffusion rate [82]:

$$\frac{1}{s(t)} \frac{ds(t)}{dt} = \frac{D}{s(t)^2} - \frac{1}{l(t)} \frac{dl(t)}{dt}, \tag{1.11}$$

with D a diffusion coefficient. Figure 1.5.c. illustrates this dynamic: the lamella is compressed under the effect of stretching until Eq. 1.11 balances, this is usually called the mixing time t_s and is defined as a function of the Pe through:

$$\gamma\, t_s \sim \beta\, Pe^{1/(2\beta+1)}, \tag{1.12}$$

with γ the lamella stretching rate and β a positive number. Once mixing time is reached, the strip width starts to grow diffusively and the concentration within the lamella decreases.

Finally, the global concentration field is defined as an ensemble of lamellae each experiencing a different stretching and diffusion rate. Figure 1.5.a. gives an example of a plume of concentration displaced in a Darcy flow field: one distinguish well the lamella topology and the stretching dynamic as the plume moves forward. As the lamellae grow under diffusion their concentration field can overlap, at this point the system enters in the final phase of mixing process when the different lamellae of the domain aggregates by diffusion.
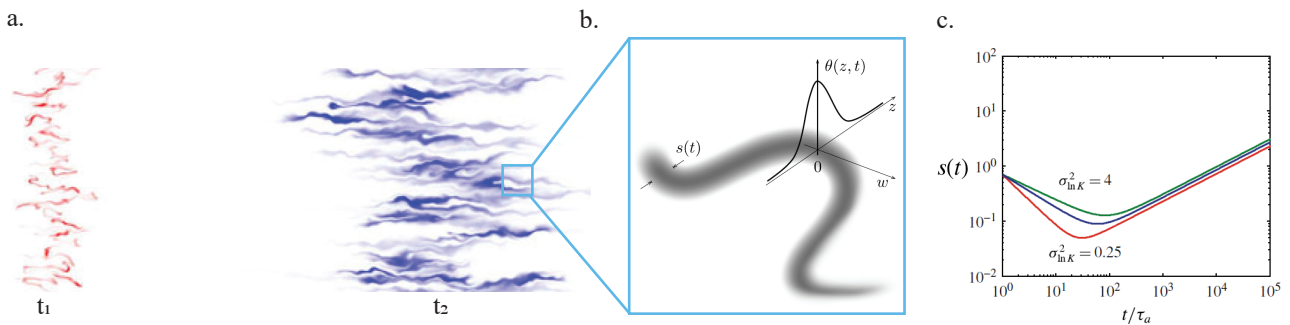
Figure 1.5: *a*. Snapshot at two time steps of a concentration field displaced in a heterogeneous flow field (adapted from [22]); *b*. The conceptual model of lamella: a strip of concentration defined by a width $s(t)$ and a Gaussian transverse profile (adapted from [82]); *c*. Temporal evolution of a lamella width $s(t)$ for different permeability field variance σ, we note the compression (typically follows a t^{-1} decrease) and diffusion regime (follows a $\sqrt{t}$ increase) (adapted from [22]).

The concept of lamella width is very important since it also defines a gradient scale, because it gives the distance over which locally concentration varies: in other words the average concentration gradient for each lamella can be defined as $|\nabla c| = c_0/s(t)$ (with c_0 the concentration of the injected solute), therefore the dynamic of $s(t)$ controls $|\nabla c|$ and, thus, mixing and other mixing related metrics such as scalar dissipation rate [83] or dilution index [64].

This lamellar description of mixing was rigorously defined at Darcy scale by [22], where starting from the description of the temporal evolution of a single lamella, diffusion coupled to stretching, and adding rules of lamellae aggregation, the authors describe the temporal evolution of the whole concentration and gradient field distribution.

In order to move a step forward and describe the concentration field at pore scale, necessary to correctly predict reaction rate and product, one must consider an intrinsic property of porous media: their confinement as previously introduced.

This thesis aims to investigate the role played by the presence of solid and impermeable walls on diffusion and heterogeneous flow kinematics. We hypothesize that confinement impacts the fundamental mechanisms of diffusion and stretching and that this will affect local concentration values and, thus, concentration gradients and mixing driven processes.

1.5 Thesis organisation

In the second chapter we approach the question of one-dimensional diffusion, building block of mixing process, by a theoretical analysis of the impact of no-flux boundary condition on the diffusion dynamic. Then, in chapter three, we suggest a novel laboratory method to measure the diffusion coefficient value of a solute (or a particle suspension), that requires no beforehand knowledge on either the molecule of interest or the fluid. We move to more complex systems in chapter four, where we developed a novel experimental set-up to visualize and measure the concentration field at the pore scale of a displacing tracer in a heterogeneous porous medium structure. Finally, in chapter five we confront our experimental results by means of flow and transport numerical simulations at both Darcy and pore-scale and we analyse the local flow kinematics using particle tracking simulation results.

Chapter 2

Diffusion limited mixing in confined media

The work presented in this chapter was published as a regular article in Physical Review Fluids:
M. Hamada, P. de Anna, and L. Cueto-Felgueroso. **Diffusion limited mixing in confined media**,
Phys. Rev. Fluids, 5:124502, 2020

2.1 Introduction

In both natural and industrial systems, and across scales, the ability of dissolved compounds to react is controlled by the efficiency of the system to mix them, promoting their physical encounter. In a quiescent fluid the mixing process is driven by the sole action of diffusion. In the presence of advection (e.g a stirred mixture or a flowing solute) the mixing front stretches, due to heterogeneity in flow velocities, while it diffuses, leading to the complex competition between these two effects, the first increasing and the second reducing solute concentration gradients [84, 85]. This combined action results in a mixing mechanism by which initially segregated substances are led to occupy the same volume [61, 86]. Classical mixing measures, such as the scalar dissipation rate [87], the degree of mixing [88] or the dilution index [64, 22] (a measure of the system entropy), are based on the detailed knowledge of the spatial distribution of the solute concentrations and their gradients.

A mass conservation equation controls the spatio-temporal distribution of a passive tracer concentration, c, through the well-known advection-diffusion equation [54, 85]:

$$\frac{\partial c}{\partial t} = -\vec{u} \cdot \nabla c + D \, \nabla^2 c, \tag{2.1}$$

where D is the diffusion coefficient and $\vec{u}$ is the velocity field experienced by the tracer. Solving Eq. (2.1) across several temporal and spatial scales is necessary to understand important scientific questions (e.g. kinetics of reactions or microbial growth) and to address industrial (e.g. bioremediation, filtration) and societal issues (e.g. efficient design of water treatment solutions). In most practical applications, it is challenging to solve Eq. (2.1) via numerical simulation or measuring c across relevant spatial/temporal scales. Thus, upscaling techniques that focus on the controlling physical mechanisms to predict their larger scale impact have been developed, including volume averaging methods [89] or statistical models, such as the continuous time random walk [65], multirate-mass-transfer [65] or the lamellar framework [22]. The latter has been successfully applied to a wide range of flow systems characterized with a different flow kinematics, as turbulent [90], chaotic [86] or laminar flows [78, 79, 22].

In a lamellar framework, a transported scalar field is characterized by a displacing front organized as an ensemble of thin and elongated structures, called lamellae, which are stretched and folded by the background heterogeneous flow field and typically characterized by their length $l(t)$ and width $s(t)$ [80]. An individual lamella undergoes the following geometrical changes, as it is moves: i) it is displaced and stretched by the flow kinematics, ii) it diffuses along the front transverse direction and iii) it eventually merges with another lamella to form larger lamella bundles [80, 86, 22]. The model, then, solves Eq. (2.1) for a single lamella in a Lagrangian framework:

$$\frac{\partial c}{\partial t} = -\frac{n}{s}\frac{ds}{dt}\frac{\partial c}{\partial n} + D\frac{\partial^2 c}{\partial n^2}, \tag{2.2}$$

where n denotes the spatial coordinate in the direction perpendicular to the lamella, along which diffusion takes place. Using the Ranz transform [80, 81], space is normalized by the lamella width $s(t)$, $\bar{n} = n/s(t)$ and time is expressed in terms of diffusion time $s(t)^2/D$, $\bar{t} = D\int_0^t 1/s(t')^2 dt'$. Thus, mixing reduces to a one-dimensional diffusion problem:

$$\frac{\partial c}{\partial \bar{t}} = \frac{\partial^2 c}{\partial \bar{n}^2}. \tag{2.3}$$

The mixing driven by these processes is then modeled considering the dynamics of the average between several lamellae thicknesses that individually takes place only along the direction transverse to the local front. This diffusion equation controls mixing-driven phenomena also in many other situations where a mixing front is steady (as in micro-reactors where solutes are injected side-by-side) and the kinematics of fluid motion can be neglected. For continuous systems where a tracer can

freely diffuse across space, an initial pulse or front of tracer would result in a diffusive profile with Gaussian- or error function-like shape. However, several mixing-driven processes happen in media characterized by confinement, such as capillary tubes, batch reactors or porous systems (as filters or soils): in such scenarios the walls defining the confined domain, e.g. a capillary tube surface or porous media grains, are considered impermeable. As a consequence, solutes within such confined systems cannot diffuse freely, as they will experience the impermeable walls where no-flux boundary conditions must be honored.

The goal of the present work is to describe the impact on mixing of the spatial distribution and temporal evolution of a diffusive tracer in a quiescent fluid (no flow) within a system characterized by confinement, such as reactors [80], porous or fractured media [79], and microfluidics [13, 15]. To do so we solve the one-dimensional diffusion equation with no-flux boundary conditions and we assess the impact of the presence of boundaries on the following classical mixing measures: the scalar dissipation rate $\epsilon(t)$, the concentration c and gradient ∇c (whose value we denote by g_c), their corresponding probability density functions (PDFs), $p_c(c)$ and $p_g(g_c)$ and the dilution index $E(t)$. Their results are all quantitatively and qualitatively different from the unconfined case. Our results represent the building block of mixing models for more complex systems involving distributed confinement size and fluid velocity heterogeneity.

2.2 Results

We study a one-dimensional system in which a tracer undergoes molecular diffusion, for two initial configurations: at $t = 0$ the tracer is distributed either as a front or a pulse. These two initial conditions are paradigmatic cases of interest since many, more complex, configurations can be interpreted as a properly weighted statistical superposition of them. Furthermore, we consider two scenarios: i) the system has infinite size, $x \in (-\infty, +\infty)$, also called an unconfined case and ii) the system has finite size, $x \in [0, \lambda]$, also called a confined case. We introduce the following normalized space, time and concentration:

$$\hat{x} = \frac{x}{\lambda}, \quad \hat{t} = \frac{t}{\tau_D}, \quad \hat{c} = \frac{c}{c_0}, \tag{2.4}$$

where λ is the characteristic confinement length scale, $\tau_D = \frac{\lambda^2}{D}$ is the characteristic time for diffusion and c_0 is the maximum solute concentration at $t = 0$. Dropping hats for simplicity of notation, the spatio-temporal concentration distribution of a passive solute undergoing molecular diffusion is described by Fick's first law [91], stating that the mass flux is locally proportional to the concentration

gradient and mass conservation, which together lead to the diffusion equation, here expressed in terms of dimensionless quantities:

$$\frac{\partial c}{\partial t} = \frac{\partial^2 c}{\partial x^2}. \tag{2.5}$$

In addition to metrics involving explicitly the spatial extent of the diffusing tracer, a way to quantify and characterize the system mixing is in terms of the tracer concentration distribution, or PDF. We introduce it in terms of $p_c(c,t)\,dc$, the probability of sampling a concentration value between c and $c + dc$ when the spatial domain is sampled uniformly, as equal to the probability $p_x(x,t)\,dx$ to find a given location between x and $x + dx$ when sampling mass uniformly. We derive $p_c(c,t)$ by inverting, when possible, and differentiating the spatial dependence of the scalar profile $c(x,t)$ obtaining:

$$p_c(c,t)\,dc = p_x(x,t)\,dx, \quad \text{thus} \quad p_c(c,t) = p_x(x,t)\left|\frac{\partial x(c,t)}{\partial c}\right|. \tag{2.6}$$

In the configurations considered here, the profiles are invertible either on the full domain or on half of it. In that case they are also symmetrical and, thus, the PDF on half of the domain is equal to the one for the whole. The total probability of inspecting a point at any location with uniformly random sampling $p_x(x,t) = p(t)$ within the considered domain V is $P = \int_V p(t)\,dx = 1$ by definition, thus $p = 1/V$. However, in an unconfined domain with infinite size this probability is identically zero. Therefore, for an unconfined domain, we must consider a portion of it $x \in]-N, N[$ or $x \in]0, N[$, with arbitrarily large, but finite, N so that outside this domain the concentration is too small to be detected, $c < c_m$ where c_m represents the smallest concentration that is distinguishable from zero. In general, the size N of such domain must be time dependent $N = N(t)$, since the concentration is spreading. For a profile invertible on the full domain we consider $x \in]-N, N[$ and thus

$$P[-N(t) < x < N(t)] = \int_{-N(t)}^{N(t)} p(t)\,dx = p(t)\,2\,N(t) = 1, \quad p = \frac{1}{2\,N(t)}, \tag{2.7}$$

if the profile is invertible only on half of the domain we have $x \in]-N, 0[$ and

$$P[-N(t) < x < 0] = \int_{-N(t)}^{0} p(t)\,dx = p(t)\,N(t) = 1, \quad p = \frac{1}{N(t)}. \tag{2.8}$$

In the following we are going to solve the dimensionless diffusion equation (2.5) and compute different mixing measures and their scaling laws for an initial front/pulse for unconfined and confined scenarios.

2.2.1 Unconfined case

For an unconfined domain, $x \in (-\infty, +\infty)$, the partial differential equation (2.5) can be solved considering the Fourier transform along the spatial variable x, reducing Eq. (2.5) to an ordinary differential equation in the Fourier space, that can be solved and anti-transformed. The well-known general solution of Eq. (2.5) is given by:

$$c(x,t) = \frac{1}{\sqrt{4\pi t}} \int_{-\infty}^{+\infty} f_0(y)\, e^{-(x-y)^2/4t} dy, \tag{2.9}$$

where $f_0(x) = c(x, t = 0)$ is the initial concentration profile.

Initial concentration front

Assuming that the mass is initially distributed as a sharp front located at $x = 1/2$, we represent the initial condition as $f_0(x) = \theta(x - 1/2)$ (shown as a black solid line in Fig. 2.1.a), invoking the Heaviside step function θ. Thus, the solution of (2.9) for this initial condition is:

$$c(x,t) = \frac{1}{2} \left[1 + \text{erf}\left(\frac{x - 1/2}{\sqrt{4t}} \right) \right], \tag{2.10}$$

which is shown, at different times ($t = 0.0045, 0.016, 0.12$ and 0.43, from light to dark), in Fig. 2.1.a as pink solid lines. As time passes, the initially sharp concentration profile evolves towards a smoother profile, spreading across the unconfined domain.

The spatial distribution of concentration $c(x, t)$ can be mapped into its PDF $p(c)$, as defined by Eq. (2.6). We denote by $N(t)$ the distance from $x = 1/2$ to the location where concentration attains the smallest detectable value c_m, $c(x = -N, t) = c_m$ and, by symmetry, it is also the distance from $x = 1/2$ where concentration is higher than $1 - c_m$, $c(x = N, t) = 1 - c_m$. Thus, the normalization of the PDF is $p(t) = 1/(2N(t))$ and

$$N(t) = -\sqrt{4t}\, \text{erf}^{-1}(2c_m - 1), \quad \text{therefore} \quad p(t) = -\frac{1}{4\sqrt{t}\, \text{erf}^{-1}(2c_m - 1)}. \tag{2.11}$$

Note that $\text{erf}^{-1}(2c_m - 1)$ is negative, ensuring that p is positive. Finally, using Eq. (2.11), inverting and differentiating Eq. (2.10) we get:

$$p_c(c) = -\frac{\sqrt{\pi}}{2\,\text{erf}^{-1}(2c_m - 1)}\, e^{\text{erf}^{-1}(2c-1)^2}. \tag{2.12}$$

We observe that under unconfined conditions a diffusive solute of concentration c has a PDF which is independent of time. This is also shown in Fig. 2.2.a where $p_c(c)$ is plotted as solid pink lines, with color ranging from light to dark with increasing time (all solutions collapse on a single curve).
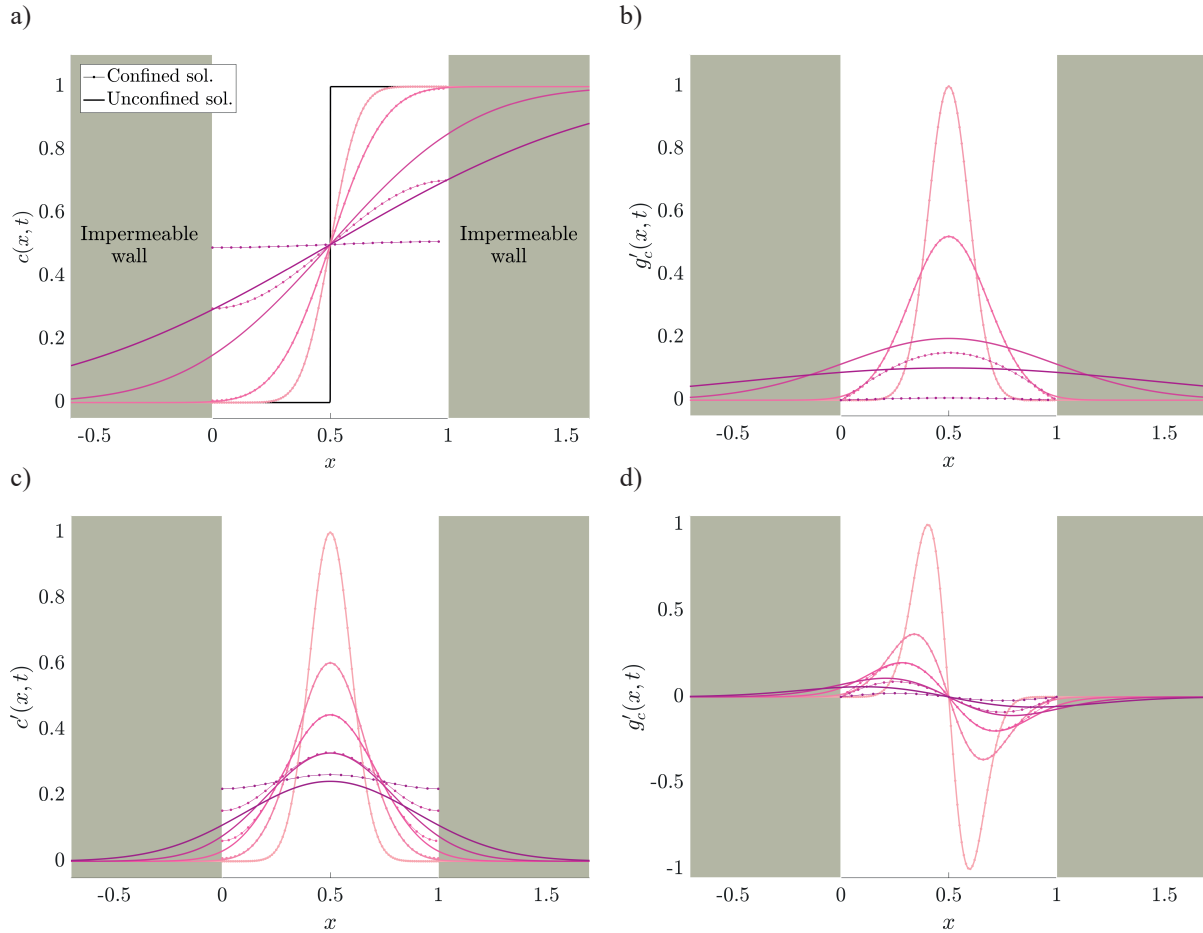
Figure 2.1: Profile of concentration c and its gradient ∇c predicted by the analytical solution of one-dimensional diffusion equation in an unconfined, Eq. (2.9) (solid line), and confined, Eq. (2.31) (dotted line), domain. a Concentration profile for a front concentration initial condition (black line), in unconfined Eq. (2.10) and confined Eq. (2.31) domain, b concentration gradient normalized by its maximum value at time $t = 0.0045$ for the profiles in a: each line in both plots corresponds to the normalized time $t = 0.0045, 0.016, 0.12$ and 0.43. c Concentration profile for a pulse initial condition in unconfined domain, Eq. (2.18), normalized by its maximum value at time $t = 0.0047$ and confined domain, Eq. (2.31), d concentration gradient for the profiles in c: each line corresponds to a different normalized time $t = 0.0047, 0.013, 0.023, 0.043$ and 0.079.

The degree of mixing reached by the diffusing system at a given time can be measured in terms of the system entropy or dilution index [64], defined as:

$$E(t) = \exp\left(-\int c(x,t)\ln[c(x,t)]\,dx\right). \tag{2.13}$$

Inserting Eq. (2.10) into the previous expression we obtain:

$$E(t) = \exp(\sqrt{2t}\, I), \quad \text{where} \quad I = -\int_{-\infty}^{\infty} \frac{1}{2}\,[1 + \text{erf}(y)] \ln\left(\frac{1}{2}[1 + \text{erf}(y)]\right) dy, \qquad (2.14)$$

having introduced the coordinate $y = \frac{x}{\sqrt{2Dt}}$. The previous exact analytical expression is shown in Fig. 2.3.*a* in a double logarithmic plot versus time and in Fig. 2.3 *b* as a semi-logarithmic plot versus $\sqrt{t}$, as pink dots: from its initial value $E(0) = 1$ (note that at $t = 0$ the concentration has value either 0 or 1) it keeps increasing as $e^{\sqrt{t}}$ for all times as result of the infinite space where the concentration can mix (and dilute) indefinitely.

The spatial variability of the concentration solution, Eq. (2.10), is quantified by its gradient, i.e. its spatial derivative, that is:

$$\nabla c = \frac{1}{\sqrt{4\,\pi\,t}}\, e^{-(x-1/2)^2/4\,t}. \qquad (2.15)$$

The previous expression is shown in Fig. 2.1.*b* as a solid pink line ranging from light to dark as time increases with the same steps of the associated concentration profile ($t = 0.0045, 0.016, 0.12$ and 0.43). As time passes the gradient maximum value g_M reached at $x = 1/2$ decreases as $g_M = 1/\sqrt{4\pi t}$ (as shown in Fig. 2.4 *a* in a semi-logarithmic plot and in Fig. 2.4.*b* in a double-logarithmic plot), while it broadens as measured by the square root of its variance, that scales as $\sqrt{2t}$. The rate at which the considered diffusive system is mixing is, then, quantified by the scalar dissipation rate as:

$$\epsilon(t) = \int_{-\infty}^{+\infty} \nabla c^T \nabla c\, dx, \qquad (2.16)$$

which quantifies the spatial availability of concentration gradients that allows the Fickian mass flux to take place. It is a measure of mixing because it is related to the time derivative of the square of concentration [88] and therefore is related to a measure of the concentration fluctuations. In the case where the considered system is finite, boundary terms appear: however, if no-flux boundary conditions apply ($\nabla c|_S = 0$), these boundary terms are identically zero and play no role at all times. Defining the change of variable $y = (x - 1/2)/\sqrt{4\,t}$, we obtain:

$$\epsilon(t) = \frac{1}{\sqrt{4\,\pi^2 t}} \int_{-\infty}^{+\infty} e^{-2y^2}\, dy = \frac{1}{\sqrt{8\,\pi\,t}}, \qquad (2.17)$$

as shown in Fig. 2.4 *c* and *d*, where it is displayed through a semi-logarithmic and double-logarithmic plot, respectively. The scaling of the scalar dissipation rate reflects that of the average gradient that can be approximated by the ratio of $g_M \approx t^{-1/2}$ and its spreading rate $t^{1/2}$, so that $\overline{\nabla c} \sim t^{-1/4}$.
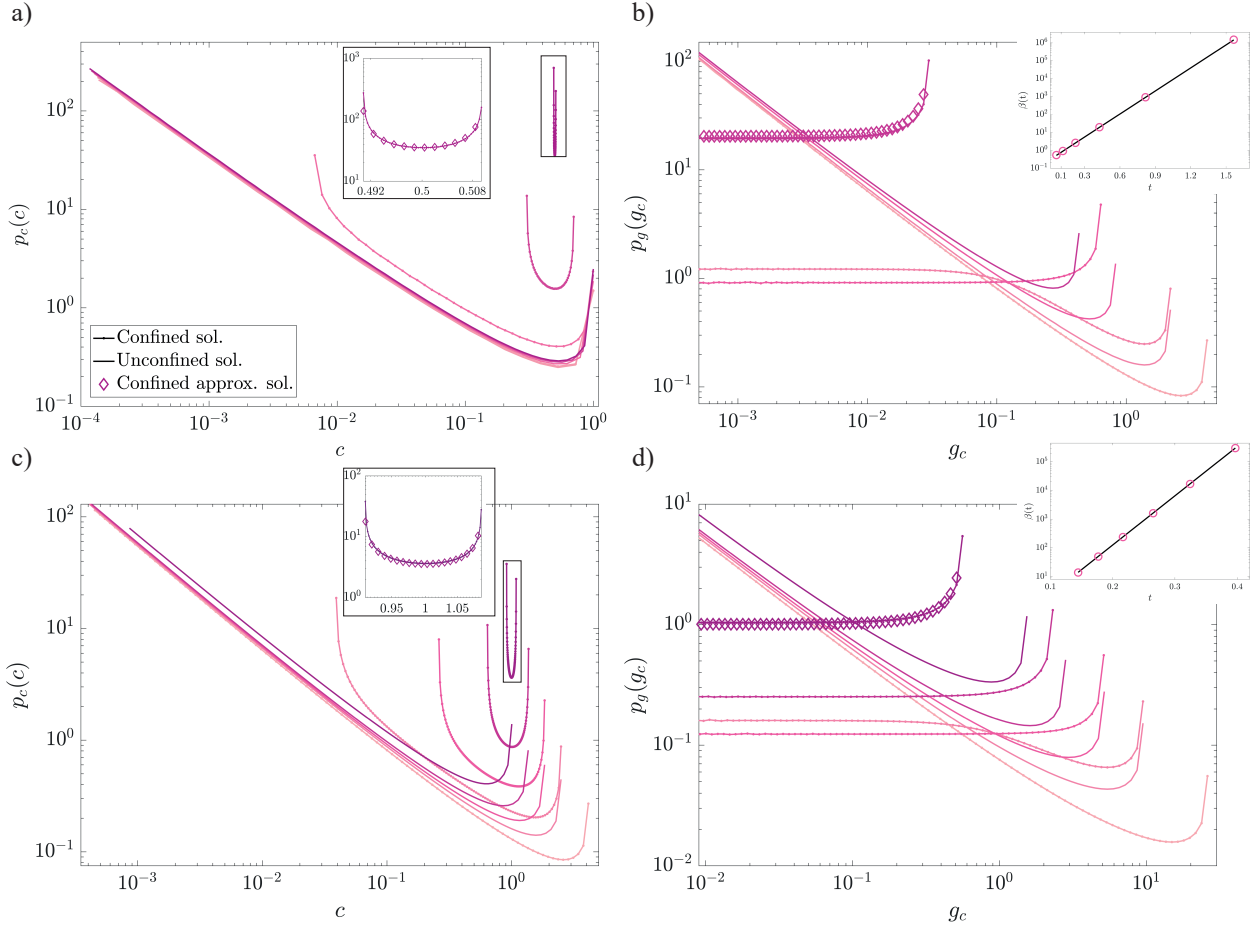
Figure 2.2: Probability density function (PDF) p_c and p_g of concentration c and gradient g_c values, shown in Fig. 2.1, for confined (solid line) and unconfined (dotted line) cases: each line corresponds to the same rescaled times as in Fig. 2.1: color scale goes from light to dark as time increases. a and b are concentration and gradient PDF for a front initial condition while c and d are concentration and gradient PDF for an initial pulse. Diamonds represent the approximated solutions derived for the confined cases. The insets in a and c are zoomed-in views of the PDF for the last time step. Insets of b and d represent the temporal evolution of the plateau value β.

Initial concentration pulse

If we consider the paradigmatic case of a pulse initial condition, for which all the mass is initially located at $x = 1/2$, as described by $f_0(x) = \delta(x - 1/2)$, the concentration profile is the well known Gaussian function:

$$c(x,t) = \frac{1}{\sqrt{4\pi t}}\, e^{-(x-1/2)^2/4t}, \quad c_M = c(x = 1/2) = \frac{1}{\sqrt{4\pi t}}, \tag{2.18}$$

which is characterized by the decay of its maximum value c_M and its lateral spreading. In Fig. 2.1 $c'(x,t) = c(x,t)/c(x,t_0)$, where $t_0 = 0.0047$, it is shown at four times steps ($t = 0.0047, 0.0128, 0.0234, 0.04.3$ and 0.0788), as a pink solid line ranging from light to dark as time increases. We notice that the con-

centration profile for a pulse initial condition Eq. (2.18) is exactly the gradient of the concentration profile of a front: this is a consequence of the linearity of the diffusion equation and the fact that an initial pulse corresponds to the gradient of an initial front. Below we show that it is not the case in a confined domain.

The PDF of this profile can be derived from Eq. (2.6). The profile is invertible only on half of the domain $x \in]0, N[$ so $p = 1/N$, computing N as described above, inverting and differentiating Eq. (2.18), we get:

$$p_c(c) = \frac{1}{2\,c\,\sqrt{\ln(c_m/c_M)\ln(c/c_M)}}. \tag{2.19}$$

which is shown in Fig. 2.2.c. Since the solution Eq. (2.18) shown in Fig.2.2 c is the same as the gradient of a diffusing front, the previous expression also represents the PDF of a front gradient $p_g(g_c)$, shown in Fig. 2.2 b, that scales as $1/g_c$ for small values and its maximum value g_M decays with time (due to mixing), as $t^{-1/2}$.

The dilution index for an unconfined diffusing pulse is computed combining Eq. (3.12) with Eq. (2.18), to get

$$E(t) = \exp[\ln(\sqrt{4\pi t}) + 1/2] = \sqrt{4\pi t}. \tag{2.20}$$

The previous exact analytical expression is shown in Fig. 2.3 c in a double logarithmic plot versus time, as pink dots: from its initial value it keeps increasing at all times (slower than the initial front) as result of the infinite space that the concentration can explore. The concentration gradient is obtained differentiating (2.18):

$$\nabla c(x,t) = -\frac{1}{\sqrt{4\,\pi\,t}}\frac{x-1/2}{2\,t}\,e^{-(x-1/2)^2/4t}, \tag{2.21}$$

and it is shown in Fig. 2.1 d at four time steps ($t = 0.0047, 0.013, 0.023, 0.043$ and 0.079), as pink solid lines ranging from light to dark as time increases. Its maximum value (equal to the opposite of its minimum value) is reached at the moving location $x = 1/2 + \sqrt{2t}$ and its absolute value decreases with time as:

$$g_M = \frac{e^{-\frac{1}{2}}}{\sqrt{8\pi}\,t}, \tag{2.22}$$

which is shown in Fig. 2.5 a in a semilogarithmic plot and in Fig. 2.5.b in a double logarithmic plot. We cannot invert and differentiate Eq. (2.21) since the spatial variable x appears within the exponential argument as well as in prefactor. Thus, we compute numerically the occurrence of the values g_c from the analytical expression Eq. (2.21), to derive the gradient distribution $p_g(g_c)$, as a

normalized histogram: the result is shown as pink solid line in Fig. 2.2.*d*, ranging from lighter to darker as time increases, for the same steps as the profiles of Fig. 2.1.*c* and *d*. As for the concentration profile, the distribution of gradient values g_c scales as $1/g_c$ for small values and it increases towards its maximum value Eq. (2.22).

The scalar dissipation rate defined in Eq. (2.16), measuring the rate of the diffusing pulse mixing, is:

$$\epsilon(t) = \frac{1}{\sqrt{32\,\pi\,t^3}}, \tag{2.23}$$

and it is shown as pink dots in Fig. 2.5 *c* as semilogarithmic plot and *d* as double-logarithmic plot.

Classical measures of mixing for unconfined diffusive systems are power law of time: this implies that for these mixing phenomena a rigorous timescale cannot be defined. However, it is common to refer to $t = 1$ (in dimensional form to λ^2/D) as the characteristic diffusive timescale. We introduced it as the timescale allowing one to make the diffusion equation dimensionless; it can also be invoked from the second centered moment of a diffusing plume as the time needed for its spreading to cover the length scale of 1.

2.2.2 Confined case

Let us now consider a system where a tracer is confined within impermeable boundaries, $x \in [0, 1]$ with imposed no-flux boundary conditions. The diffusion problem is mathematically formulated as:

$$\frac{\partial c}{\partial t} = \frac{\partial^2 c}{\partial x^2} \quad \text{for} \quad x \in [0, 1] \quad \text{with} \quad c(x, 0) = f_0(x) \quad \text{and} \quad \left.\frac{\partial c}{\partial x}\right|_{x=0,1} = 0, \tag{2.24}$$

with c, t and x defined in Eq. (2.4). Using the method of separation of variables, we can express the problem solution as:

$$c(x, t) = X(x)\,T(t), \tag{2.25}$$

which can be differentiated with respect to time and space, providing:

$$\frac{\partial c}{\partial t} = X(x)\,T'(t) \quad \text{and} \quad \frac{\partial^2 c}{\partial x^2} = X''\,T(t). \tag{2.26}$$

We then rewrite Eq. (2.24) as:

$$X(x)\,T'(t) = X''(x)\,T(t). \tag{2.27}$$
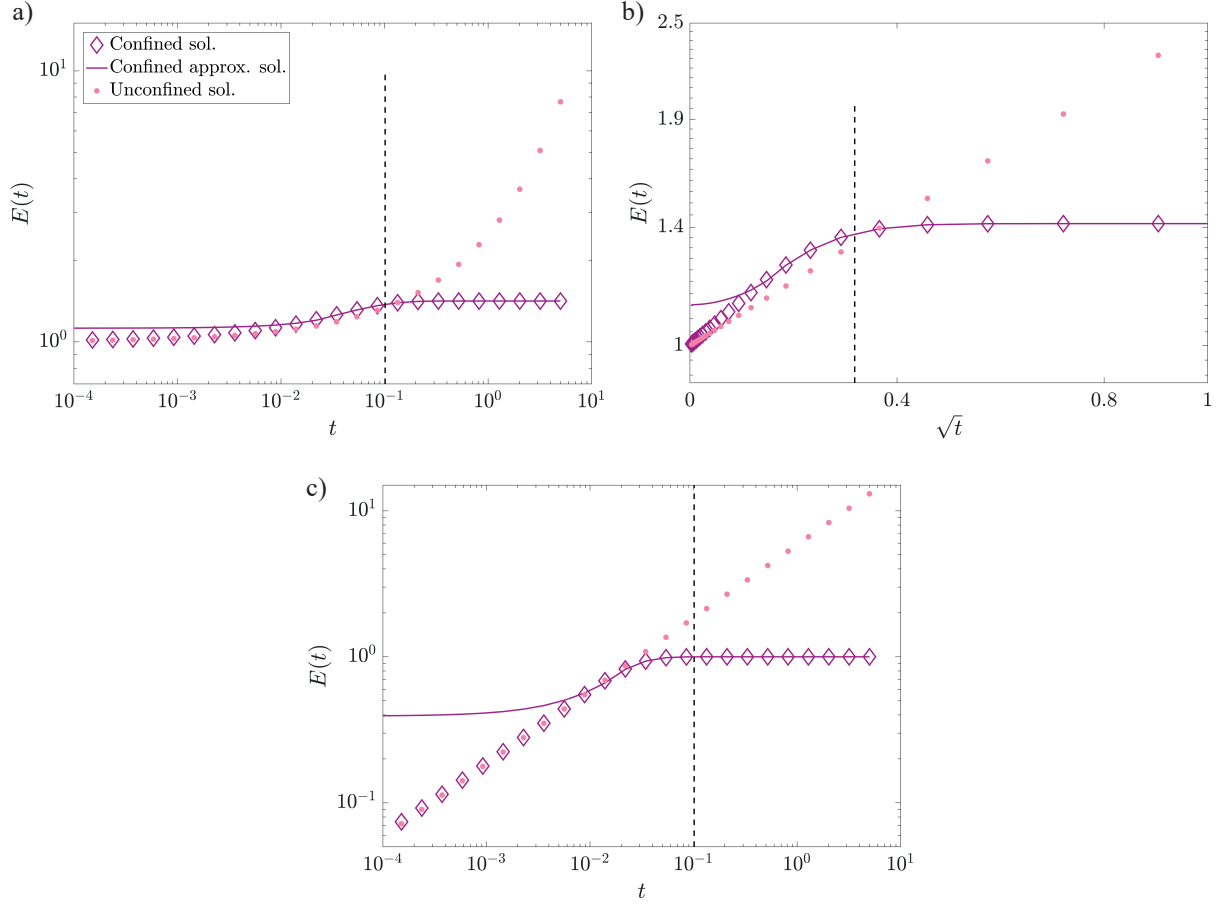
Figure 2.3: Temporal evolution of the dilution index $E(t)$, Eq. (3.12). *a* and *b* show the front initial condition: in *b* the semi-logarithmic representation of E versus $\sqrt{t}$ emphasizes the scaling $e^{\sqrt{t}}$ for early times. *c* pulse initial condition. For all initial condition, the unconfined case (pink dots) grows indefinitely, while the confined case (diamonds) reaches its maximum value (complete mixing) earlier than $t = 1/\pi^2$ (vertical dashed black line). The solid line represents the approximated analytical solution computed.

Collecting time on the left-hand side and space on the right-hand side of the equation, we obtain:

$$\frac{T'(t)}{T(t)} = \frac{X''(x)}{X(x)} = -\alpha, \tag{2.28}$$

where α is a positive constant that ensures mass conservation. We have now a system of two ordinary differential equations to be solved simultaneously:

$$X''(x) + \alpha\, X(x) = 0, \tag{2.29}$$

and

$$T'(t) + \alpha\, T(t) = 0. \tag{2.30}$$

Solving Eq.(2.29) for $X(x)$, we find the family of solutions $X_m(x) = A_m \cos(\sqrt{\alpha}\, x)$: applying the boundary condition $X'(0) = X'(1) = 0$ the only non-trivial solution is given by $\alpha = m^2\, \pi^2$. Thus, Eq. (2.30) becomes $T'(t) = -\pi^2\, m^2\, T(t)$: integrating on both sides we get $T_m(t) = P_m\, e^{-\pi^2 m^2 t} + C$. The general solution is a linear combination of the obtained sets of solutions:

$$c(x,t) = \sum_{m=1}^{\infty} B_m\, \cos(\pi\, m\, x)\, e^{-\pi^2 m^2 t} + c_f, \tag{2.31}$$

with c_f the homogeneous concentration reached at $t = +\infty$ and B_m a coefficient that depends on the spatial initial distribution $f_0(x) = c(x,0)$:

$$B_m = 2 \int_0^1 f_0(x)\, \cos(\pi\, m\, x)\, dx. \tag{2.32}$$

The derived solution Eq. (2.31) expresses the concentration profile as the superposition of modes m (functions that do not change shape as the system diffuses) that are periodic and fluctuating in space between the domain boundaries, while temporally decaying exponentially fast with characteristic scaling $\exp(-m^2\pi^2\, t)$.

Initial concentration front

For an initial front $f_0(x) = \theta(x - 1/2)$, the profile in Eq. (2.31) is shown in Fig. 2.1 (as a pink dotted line ranging from light to dark as time increases) at the same time steps, shown for the unconfined case. At early times the confined and unconfined profiles exactly overlap, while at later times they do not. On the one hand, the confined solution, due to the no-flux boundary conditions imposed, keeps a flat profile at the boundaries ($x = 0, 1$) and, thus, a steep gradient providing a strong diffusive mass flux responsible for mixing. On the other hand, the unconfined solution spreads across space smoothing its gradient, reducing dramatically the Fickian mass flux and, thus, the overall mixing.

For times larger than $t > 1/(m^2\pi^2)$ the exponential time dependence of the mode m cannot be neglected. Since for the mode $m = 1$ the coefficient $B_1 = 2/\pi$ is non-zero, it dominates the solution, Eq. (2.31), for times larger than $1/\pi^2$. For such times, the concentration profile is well approximated by:

$$c(x,t) \approx c_f - 2/\pi\, \cos(\pi\, x)\, e^{-\pi^2 t}, \tag{2.33}$$

with the value of c that is bounded between its minimum and maximum values $c_m < c < c_M$, that

a)

b)

c)

d)

Figure 2.4: Temporal evolution of the maximum gradient g_M and scalar dissipation rate ϵ for a front initial condition. The semi-logarithmic plot in a and c emphasizes the exponential cut-off due to confinement that takes place around $t = 1/\pi^2$; the double logarithmic plot in b and d emphasizes the power law decay for early times, taking place when the confinement has no impact on diffusive mass transfer.

are taken at the impermeable walls $x = 0, 1$ where they vary to conserve the total mass, as:

$$c_m = c(x = 0, t) = c_f - 2/\pi\, e^{-\pi^2 t}, \quad c_M = c(x = 1, t) = c_f + 2/\pi\, e^{-\pi^2 t}. \tag{2.34}$$

At early times, $t < 1/\pi^2$, several terms of the expansion, Eq. (2.31), must be taken into account and we cannot invert and differentiate it to compute its PDF, $p_c(c)$. However, at such short times the solution for $c(x, t)$ is not affected by the presence of the impermeable boundaries at $x = 0$ and $x = 1$ and it is well approximated by (2.10) and thus also $p_c(c)$ is known and given by Eq. (2.12). For $t > 1/\pi^2$ we can invert and differentiate Eq. (2.33) to derive the probability density function. The profile is invertibe on the full domain $x \in]0, 2N[$, in the confined case $N = 1/2$ so $p = 1/(2N) = 1$,

and we get:

$$p_c(c,t) \approx \frac{1}{2} \frac{\exp(\pi^2 t)}{\sqrt{1 - \left[(c_f - c)\frac{\pi}{2}\exp(\pi^2 t)\right]^2}}, \tag{2.35}$$

which is shown in Fig. 2.2*a* as a pink dotted line from light to dark, for increasing time. As time overcomes $1/\pi^2$ the concentration PDF becomes time dependent and it deviates from the unconfined case: for low concentrations it deviates from the scaling $\sim 1/c$ towards a U-shaped function, characterized by peaks at the smallest and largest value, Eq. (2.34), and it is exactly described by Eq. (2.35), as shown in Fig. 2.2 *a* (diamonds).

We were not able to derive an analytical expression for the dilution index for this case and, thus, it has been computed numerically inserting Eq. (2.31) within the definition of E Eq. (3.12). This is shown in Fig. 2.3 *a* where the confined case from its initial value $E(t = 0) = 1$ rises up to its final plateau for times larger than $t > 1/\pi^2$ corresponding to:

$$E(t) = \exp\left[-\int c_f \ln(c_f)\,dx\right] = \exp[-1/2\ln(1/2)] = \sqrt{2}, \tag{2.36}$$

implying that the macroscopic mixing state of the diffusing system stops evolving, while the unconfined case grows indefinitely. Moreover, the semilogarithmic plot of E versus $\sqrt{t}$ shown in Fig. 2.3.*b* highlights the higher degree of mixing of the confined case for times even shorter than $\sqrt{0.1}$ corresponding to times shorter than 0.01.

For large times, $t > 1/\pi^2$, we compute the gradient of Eq. (2.33):

$$\nabla c \approx 2\sin(\pi x)\,e^{-\pi^2 t}. \tag{2.37}$$

The above expression for ∇c, whose value we denote by g_c, can be inverted and differentiated to compute its probability density function as:

$$p_g(g_c) = \frac{1}{2\pi} \frac{\exp(\pi^2 t)}{\sqrt{1 - \left[\frac{1}{2}g_c\exp(\pi^2 t)\right]^2}}, \tag{2.38}$$

shown in Fig. 2.2 *b* (diamonds). We remark that for a front initial condition the concentration is dissipated very quickly and the values c_m and c_M approach exponentially fast the asymptotic value c_f, flattening the spatial profile: this is reflected on the concentration PDF $p_c(c)$ that deviates from the unconfined $1/c$ to become flat at low c values where it gets the value $\beta \approx \frac{\exp(4\pi^2 t)}{4\pi}$, as shown in Fig. 2.2.*b* and its inset. The concentration gradient reaches its maximum value, g_M, at location
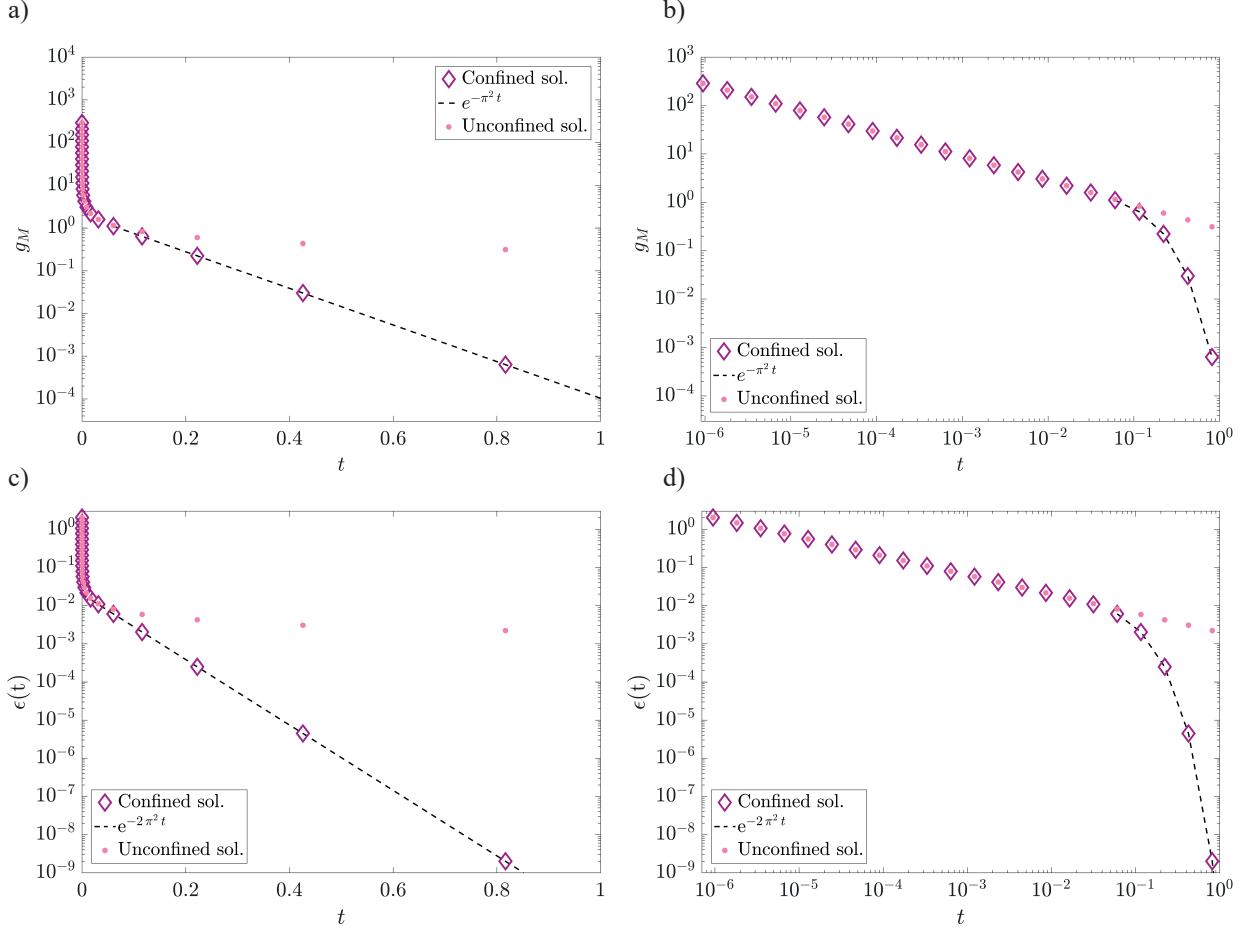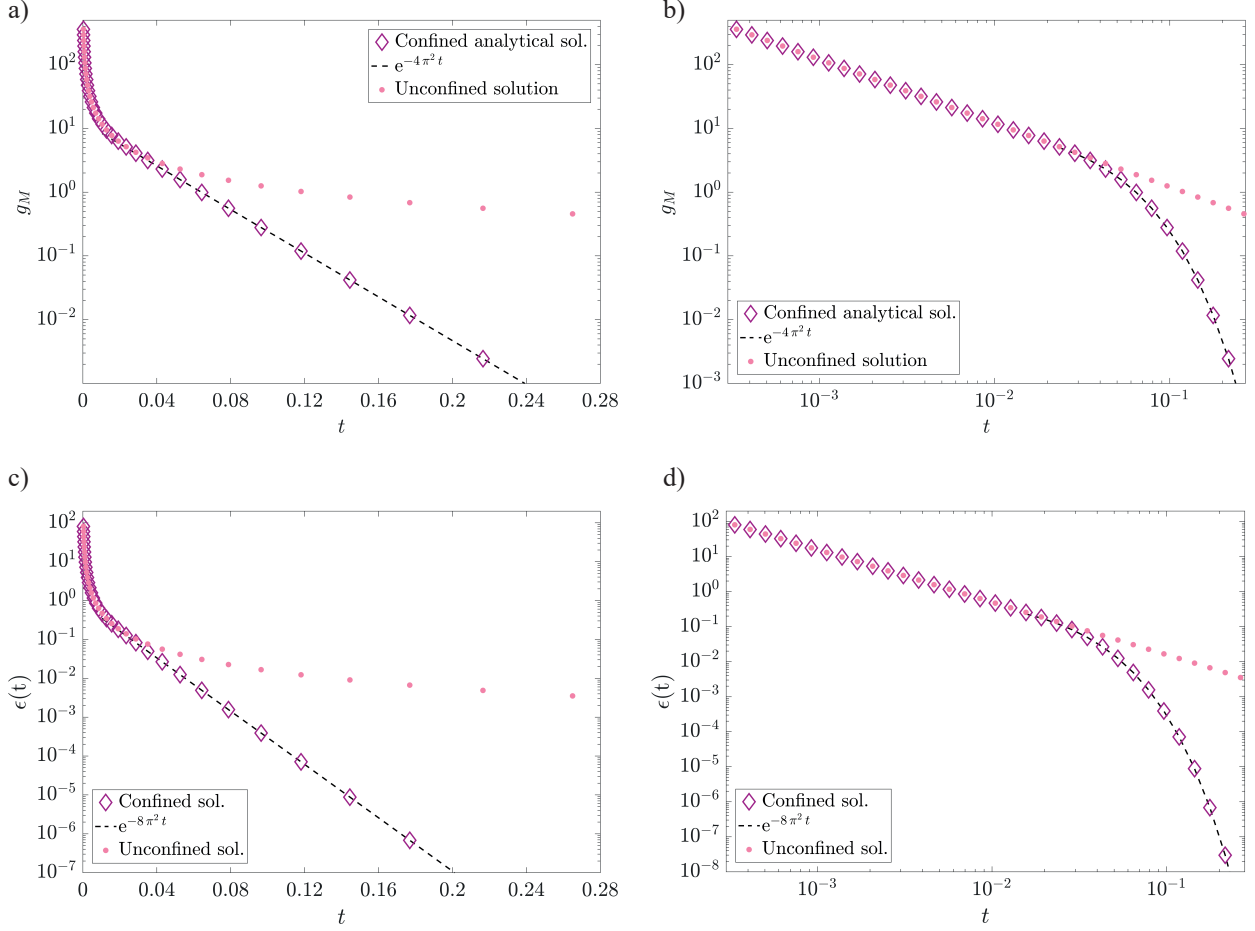
Figure 2.5: Temporal evolution of the maximum gradient g_M and scalar dissipation rate ϵ for a pulse initial condition in unconfined (dots) and confined (diamonds) cases. The semi-logarithmic plot in *a* and *c* emphasizes the exponential cut-off (dashed black line) due to confinement that takes place around $t = 1/\pi^2$; the double logarithmic plot in *b* and *d* emphasizes the power law decay for early times, taking place when the confinement has no impact on diffusive mass transfer.

$x = 1/2$:

$$g_M = \nabla c(x = 1/2, t) = 2\,e^{-\pi^2 t}, \tag{2.39}$$

and decays much faster (exponentially fast) than the power law decrease of the unconfined case, as shown in Fig. 2.4.*a* and *b*. This change in temporal decay is due to the fact that to conserve mass the concentration value at the boundaries vary exponentially fast (see Eq. (2.34)) as the tracer gets accumulated there due to the spatial confinement.

From the spatial profile of the concentration gradient Eq. (2.37), we compute the analytical expression of the scalar dissipation rate for $t > 1/\pi^2$ as:

$$\epsilon(t) \approx 2\,e^{-2\pi^2 t}, \tag{2.40}$$

whose exponential decay, shown in Fig. (2.4) c and d superposed to the slower power-law decay $1/\sqrt{8\pi t}$ of the unconfined case, has the characteristic time $1/(2\pi^2)$.

Initial pulse

We now consider an initial pulse $f_0(x) = \delta(x - 1/2)$. Since $B_1 = 0$, for times larger than $1/(4\pi^2)$, the leading mode of Eq. (2.31) is $m = 2$ (and $B_2 = -2$) so that:

$$c(x, t) \approx c_f - 2\cos(2\pi x)\,\exp(-4\,\pi^2\,t), \qquad (2.41)$$

with the concentration value bounded between its minimum and maximum values c_m and c_M, respectively, which are:

$$c_m = c(0, t) = c_f - 2\,e^{-4\pi^2 t}, \quad c_M = c(1/2, t) = c_f + 2\,e^{-4\pi^2 t}. \qquad (2.42)$$

We observe that, unlike in the unconfined case, the concentration profile for the pulse initial condition differs from the gradient of a diffusing front. The former decays exponentially with a characteristic time which is four times shorter: $1/(4\pi^2)$ instead of $1/\pi^2$. Moreover, the two spatial profiles are different since the front gradient is zero at the boundaries ($x = 0$ and $x = 1$) to ensure no flux at impermeable walls, while the pulse solution, to conserve the mass, is always above zero and it increases at both boundaries with time.

For early times $t < 1/(4\pi^2)$ several terms of the sum in (2.31) must be taken into account and we cannot invert it to compute $p_c(c)$. However, at such short times the solution for c is not affected by the presence of the impermeable boundaries at $x = 0$ and $x = 1$ and it is well approximated by (2.18) and thus also $p_c(c)$ is known. At large times, we invert and differentiate the concentration spatial profile Eq. (2.41) on half of the domain, $x \in]0, N[$ so $p = 1/N = 2$, to derive the probability density function $p_c(c)$ as:

$$p_c(c, t) \approx \frac{\exp(4\pi^2\,t)}{2\pi\,\sqrt{1 - \left(\frac{(c - c_f)\,\exp(4\pi^2\,t)}{2}\right)^2}}, \qquad (2.43)$$

shown in Fig. 2.2.c (diamonds). We remark that for a pulse initial condition the concentration is dissipated very quickly and the values c_m and c_M approach exponentially fast the asymptotic value c_f, flattening the spatial profile: this is reflected on the concentration PDF $p_c(c, t)$ that deviates from the scaling $1/c$ towards a U shape.

As for the front case, we were not able to derive an analytical expression for the dilution index in a confined domain, thus, it has been computed numerically inserting Eq. (2.31) within the definition of E Eq. (3.12). This is shown in Fig. 2.3.*c* where the confined case deviates from the unconfined one at times even shorter than $1/(2\pi^2)$ to reach its final plateau. This shorter mixing time can be understood analyzing the scalar dissipation rate, discussed below.

We compute the corresponding concentration gradient considering only the dominant term $m = 2$, and we have:

$$\nabla c(x,t) \approx 4\,\pi \sin(2\,\pi\,x)\,e^{-4\,\pi^2\,t}. \tag{2.44}$$

The above expression for the concentration gradient, whose value is denoted by g_c, can be inverted and differentiated to compute its probability density function as:

$$p_g(g_c) = \frac{\exp(4\pi^2\,t)}{8\pi^2\,\sqrt{1 - \left[\frac{1}{4\pi}\,g_c\,\exp(4\pi^2\,t)\right]^2}}, \tag{2.45}$$

where its minimum and maximum values are reached at the steady locations $x = 1/4$ and $x = 3/4$, respectively:

$$g_m = \nabla c(x = 1/4, t) = 4\pi\,e^{-4\pi^2 t} \quad \text{and} \quad g_M = \nabla c(x = 3/4, t) = -4\pi\,e^{-4\pi^2 t}. \tag{2.46}$$

Note that for the unconfined case the locations where $\nabla c = g_m$, g_M are moving as $\sqrt{t}$ away from x_0. As for the concentration, also the gradient profile flattens at large times and its PDF $p_g(g_c)$ deviates from the unconfined $1/c$ scaling to become constant at low c values where it gets the value $\beta \approx \frac{\exp(4\pi^2\,t)}{8\pi^2}$, as shown in Fig. 2.2.*d* and its inset. From the spatial profile Eq. (2.44), we compute the scalar dissipation rate as:

$$\epsilon(t) \approx 8\,\pi^2\,e^{-8\,\pi^2\,t}, \tag{2.47}$$

which is shown in Figs. 2.5 *c* and *d* in a semi-logarithmic and double logarithmic plots, respectively, to highlight its exponential decay which is much faster than the power law scaling of the unconfined case. We note that the exponential decay characteristic time is $1/(8\pi^2)$ and it is shorter than the $1/(2\pi^2)$ characteristic of mixing for the front case, as observed also in the dilution index analysis, discussed above.

Numerical solutions as control

We tested all our analytical derivations against numerical solutions of the diffusion equation in a confined domain. We adopted a backward finite difference simulation scheme for the diffusion equation in a one-dimensional and confined domain, with no-flow boundary condition. The initial conditions we impose to the front and pulse initial conditions are defined as Eqs. (2.10) and (2.18) for $t = t_0 = 10^{-8}$, respectively, which corresponds to the two theoretical initial configurations that underwent a little diffusion. The numerical results show that our derived solutions accurately describe the physical problem (the mean-squared error between the two profiles is below $10^{-8} c_0$ at all times). All expressions we derived for concentration profiles and mixing measures are in excellent agreement with the numerical simulations.

2.3   Impact

We showed that diffusion in a confined domain is qualitatively and quantitatively different from diffusion in an unconfined and continuous domain. To illustrate the potential impact of the discussed results on mixing within confined media, we simulate, as a proof of concept, the displacement of a mixing front in a porous material. We run a numerical simulation for Stokes flow in a 1 mm × 3 mm porous medium with a prescribed geometry, no-slip boundary conditions at grains walls (gray disks in Fig. 2.6), characterized by an average pore throat size of $l = 0.05$ mm, resulting in an average fluid velocity of 1 mm/s (Reynolds number $Re = l\,u/\nu = 0.05$). In this flow we solve the transport of a passive solute Eq. (2.1) continuously injected from the left-hand side of the system, with no-flux boundary conditions at the grain walls. A snapshot of the concentration field transported within a porous medium for a Péclet number $Pe = \tau_D/\tau_A = u\,l/D = 2500$ (a measure of the relative importance of advective and diffusive mechanisms) is given in Fig. 2.6a after 40 advective time steps ($t = 40t_A$). For the $Pe = 2500$, this corresponds to $\approx 1.5\%$ of the diffusive time, which would imply a very sharp front where diffusion has not had the time to play a role at the scale of a pore. Instead, the figure shows that diffusion had the time to smear the pore-scale concentration gradients within the pores. This would be consistent with the much smaller $Pe = t_\epsilon/\tau_A = 250$, defined with respect to the confinement-limited diffusion time scale t_ϵ, defined in terms of the scalar dissipation rate, for which 40 advective time scales correspond to $\approx 15\%$ of it.

The concentration field is heterogeneously distributed across the pores and along the fluid displacement front, which is stretched and elongated resulting in a lamellar structure. In Fig. 2.6.b we show

a zoom-in view of mixing at a single pore throat, to highlight the pore scale non-mixed condition, which is quantified in Fig.2.6.*c* where the interpolation of the concentration field across the pore throat is shown in red. We observe that the concentration profile confined in a pore is qualitatively different from its unconfined counterpart (blue line); indeed the presence of an impermeable boundary i) prevents the solute from diffusing freely, ii) enhances the diffusive flux decreasing the scalar dissipation rate, iii) resulting in a rise of the small concentration values (left-hand side of the red line in Fig. 2.6.*c*). This example qualitatively illustrates the potential impact of the impermeable boundary conditions on mixing state and rate in confined environments. To properly capture the mixing dynamics taking place in these porous systems, the derived confined solution for diffusion must be incorporated with the stretching dynamics in a lamellar framework, where the distribution of the confinement length scale *l* and the stretching of the front associated to the host medium heterogeneity are coupled in a non trivial way. A detailed study of mixing in such a complex and confined flow system goes beyond the research presented in this article, but must incorporate the results presented here for diffusion alone.
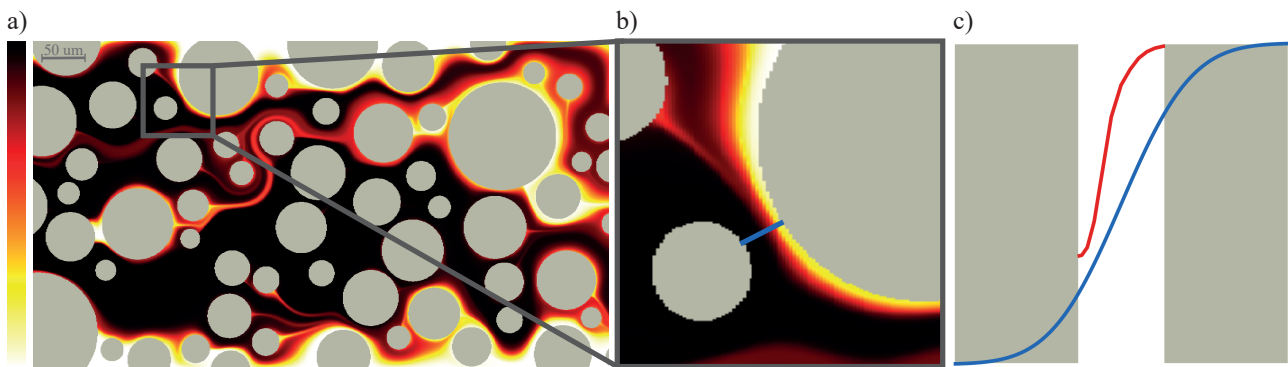
Figure 2.6: *a* Concentration field in a porous medium composed of round grains (gray disks) for *Pe* = 2500 after rescaled time t/τ_A = 40. *b* Zoom-in of the same concentration field in a pore. *c* The blue line shows a diffusive unconfined concentration profile; the red line represents the interpolated concentration profile along the blue segment in *b*).

2.4   Conclusions

Diffusion is the key mixing mechanism in fluid systems, since it ultimately homogenizes concentrations, also in the presence of stretching and compression by velocity heterogeneity. We present analytical results of the one-dimensional diffusion equation in a confined domain, characterized by the presence of no flux boundaries, separated by a distance λ, that prevent the solute concentration from diffusing freely and explore wider areas of space. We show how diffusion is affected by the confined nature of the considered spatial domain and we quantify its impact on mixing.

The general solution of the diffusion equation in a confined domain, Eq. (2.31), expresses the concentration profile of a diffusive tracer as the superposition modes m (functions that do not change shape as the system diffuses) that are periodic and fluctuating in space between the domain boundaries, and temporally decaying exponentially fast, scaling as $\exp(-m^2\pi^2 t)$. As far as the diffusing tracer does not experience the presence of the impermeable boundaries (e.g. right after the injection of a pulse in the middle of the domain $t < 1/(m^2\pi^2)$) the exponential decay of the modes is not substantially changing their amplitude and a large number of modes must be taken into account to describe the tracer concentration profile, recovering the solution of the unconfined case. In such conditions space and time are coupled and the concentration profile can be expressed in terms of the classical dimensionless coordinate for diffusion, $\xi = x/\sqrt{2Dt}$, making the profile self-similar and scale independent, which is reflected in the slow, power law decay of several mixing measures. However, as soon as a single mode m dominates the sum, space and time are decoupled and the exponential decay of the solution defines a characteristic time scale $(1/(m^2\pi^2))$, as reflected by the exponential decay of the mixing measures considered.

Physically, in a confined space the no-flux boundary condition $\nabla c(0,t) = \nabla c(\lambda,t) = 0$ imposes a flat profile at the domain edges leading to an overall steeper gradient and higher mass flux compared to the unconfined case where mass can freely diffuse exploring wide areas of space, slowly dissipating the concentration gradients. Therefore local and global measures of mixing display significantly different dynamics. We show that, maximum concentration gradients and scalar dissipation rate drop exponentially fast and the dilution index E reaches a plateau, while they typically follow a slower power law decrease in an unconfined domain and E grows indefinitely. Also the concentration and gradient distribution (PDF) significantly change their shape and dynamics. This exponential time scaling of mixing measures in confined conditions leads to the definition of a new characteristic time scale for diffusion, which depends on the initial condition and it is fixed by the leading mode (e.g. $m = 1$ for a front and $m = 2$ for a pulse), $\lambda^2/(m^2 D \pi^2)$, which is much shorter (one order of magnitude shorter) than the characteristic λ^2/D defined to re-scale the diffusion equation.

These observations show that the homogenization dynamics (mixing) is significantly faster under confinement, i.e. no-flux boundary conditions. In more complex scenarios, where the host medium heterogeneity must be taken into account, diffusion must be coupled with flow and fluid stretching variability [84, 22] as well as confinement scale λ that can change considerably [21]. For example, in a lamellar framework [72, 22], the local confinement scale λ should be normalized by the

lamella width $s(t)$ and time is rescaled by the characteristic diffusive time over a lamella width $\bar{t} = D \int_0^t 1/s(t')^2 dt'$, since fluid stretching affects the local diffusion process by keeping the gradients steep. In such scenario, the boundary conditions become time dependent and given by:

$$\left. \frac{\partial c}{\partial \bar{n}} \right|_{\bar{n}=0,\lambda/s(\bar{t})} = 0. \tag{2.48}$$

Furthermore, in a heterogeneous medium λ must be defined locally, leading to a space-dependent characteristic time scale. Implementing a full mixing model taking into account no-flux boundary conditions at domain boundaries is non-trivial and requires further work. However, neglecting confinement-limited diffusion to describe mass transport phenomena may lead to an incorrect description of mixing.

Chapter 3

Novel method to measure diffusion coefficient of tracers

3.1 Introduction

Molecular diffusion of substances in liquids is a key process in numerous natural and engineering systems. It is often the reaction rate limiting factor in biological or chemical reaction. Generally, it is the ultimate mechanism by which concentration get homogenized and, thus, mixing and dilution occur. Since the beginning of the 20th century chemists and biologists were interested in developing laboratory methods to accurately assess this process. Molecular diffusion of a given dissolved or suspended compound originates from the individual molecules (or particles) motion that is associated to their thermal agitation: a famous example is the early observation of pollen grains movement in water by Brown [46]: the macroscopic consequence of this microscopic phenomenon is that the mass of that compound spreads in space as time passes.

The description of this macroscopic spreading is given by Fick's first law: it states, in analogy with Fourier's law of thermal conductivity, that the diffusive mass flux $J(x)$ at a location x is proportional to the concentration gradient, it gives in one dimension and for a proportionality constant D:

$$J(x) = -D\frac{\partial c}{\partial x} \tag{3.1}$$

where the constant of proportionality D is the so-called diffusion coefficient. The negative sign implies that mass moves from locations with higher concentration towards areas of lower concentrations. Since their gradient changes with time as the substance diffuses, mass conservation must be considered to described the concentration spatio-temporal dynamics:

$$\frac{\partial c}{\partial t} = -\frac{\partial}{\partial x} J(x), \tag{3.2}$$

which states that for a given location x a change in the mass flux is associated to a change of concentration in time. Combining the two Fick's laws we obtain the well-known diffusion equation describing the spatio-temporal distribution of a diffusing substance:

$$\frac{\partial c}{\partial t} = -D \frac{\partial^2}{\partial x^2} c(x). \tag{3.3}$$

Knowing the value of D is crucial to describe the fate of a diffusing substance and all the diffusion-related phenomena, like mixing or reactions. For spherical object of radius r the value of the diffusion coefficient can be theoretically derived from the well-known Stokes-Einstein relation [53] which couples the kinetic energy associated to the thermal agitation of particles and the viscous drag the particle experiences while moving within a fluid of viscosity μ leading to:

$$D = \frac{kT}{6\pi\mu r}, \tag{3.4}$$

with k the Boltzmann constant in [J/K], T the temperature in [K], μ the dynamic viscosity in [Pa s] and r the particle radius in [m].

For objects of approximately spherical shape (e.g. many type of molecules, colloids or bacteria) for which the radius is known, several methods have been developed in the past decades to measure the value of D based either on the microscopic (individual motion) or macroscopic (concentration distribution) properties of the process. Dynamic Light Scattering (DLS) measures intensity fluctuation of light scattered by particles and relates it to the particle velocity. It is a technique in physics that is typically used to determine the size distribution of small particles in suspension; it is based on the Mie theory that describes the scattering of light by a homogeneous set of spherical objects of same (or similar) size. Knowing the size of the diffusing objects composing the substance under investigation, based on Eq. (3.4) the diffusion coefficient can be calculated [92].

Other methods to measure D in liquids are based on macroscopic mass transfer. For instance the one based on Taylor dispersion within a Poiseuille flow, where a pulse of a substance is injected within a tube stream and the concentration measured at the outlet. The obtained profile is then fitted to the solution of dispersion equation where the proportionality constant D_t is Taylor diffusivity. The value of the diffusion coefficient D can be then back computed knowing the tube radius

r and mean flow velocity u through $D_t = r^2 u^2 / (48 D)$ [93, 94].

Another method exploits the diaphragm cell [95, 96, 97]: two reservoirs of volume V are separated by a porous membrane and a solute diffuses from one to the other through the membrane, the concentration is measured in one reservoir at time interval dt and thus the rate of change of solute concentration $dc/dt = (c_2 - c_1)/(t_2 - t_1)$ in the reservoir is given by Fick's law and depends on the membrane width l and effective porosity A as $V \, dc/dt = -D \, A \, (c_{t1} - c_{t2})/l$ from which the value of D is determined. A calibration with a solute of known diffusion coefficient is required to determine A.

All these widely used methods are either based on indirect measurements (DSL and Taylor dispersion) or require previous knowledge on both solute and solvent (for the diaphragm cell knowledge on the solute, its approximate molecule size are necessary to choose the proper membrane). We propose, here, a method to measures the diffusion coefficient D, the proportionality constant appearing in the Eq. (3.3), that requires no beforehand knowledge on neither the target substance nor on its solvent. It also do not depends on the initial condition of the concentration profile, it only requires two profiles and the time separating them. The method has an uncertainty of 3 % on the measured value of the diffusion coefficient. To the best of our knowledge, and considering the properties described above, the method is new.

3.2   Method

Let's consider a tracer of concentration c dissolved, or suspended, in a given liquid. The main idea behind our method is to measure the spatio-temporal evolution of the concentration profile $c(x,t)$ with optical techniques, under initial and boundary conditions for which an analytical solution of the diffusion equation Eq. (3.3), depending only on D, is known. By fitting this analytical solution $c(x,t)$ to the measured concentration profile will provide an estimate of the diffusion coefficient D. To validate our experimental set-up we use a tracer for which the diffusion coefficient can be predicted by the Stokes-Einstein relation [53]: we choose fluorescent polyethylene micro spheres whose density can be matched by the liquid medium. We will, then, apply the same methodology to a colored tracer whose molecule is non spherical. In separate experiments, both tracers are optically visualized and we relate the signal detected by a camera to their local concentration value.

3.2.1 Fluorescent particles tracer

We use polystyrene fluorescent micro-spheres (Fluoro-Max, Thermo Fisher B150) of radius $r = 0.075\,\mu m$ that are provided at 1 % solid concentration, from which we prepare a 20 times diluted in a milliQ water and heavy water mixture of density 1.05 g/ml, matching the one of the micro-spheres to avoid their sedimentation. When fluorescent molecules are excited by incoming light at given wavelength, their electronic cloud get excited for a very short time scale and, then, it relaxes to its ground state by emitting photons at a larger (and less energetic) wavelength. The emission signal is distinguished from the excitation one by the use of a filter and it is detected by a camera. The amount of light recorded is proportional to the one emitted by the tracer and, thus, to its concentration. Excitation and emission light are selected using a filter-cube (Nikon, DAPI, excitation bandpass 395 ± 10 nm and emission bandpass 475 ± 11 nm).

The light detected by the camera is recorded into a gray-scale image and stored as a matrix im of integer values between 0 (black) and $2^{bit} - 1$ (white), where bit represents the color-depth of the camera. We used a Nikon DS-Qi2 which is equipped with a CMOS full-frame sensor recording at 12-bit. If the tracer is not so concentrated to block part of the incoming and its own emitted light, the value of this matrix im is proportional to the tracer concentration as $im = s\,c + im_0$, where s is a proportionality constant and im_0 represents the background noise, or the signal detected in absence of tracer. Thus,

$$c = \frac{1}{s}\,(im - im_0),\tag{3.5}$$

where the value of s can be found via a calibration procedure collecting pictures of samples of known concentration. We verified via a calibration that the tracer at the adopted concentration satisfies the Eq. (3.5): however, to avoid propagation of error associated to the estimation of the parameter s, we express the concentration c relative to its initial value c_0:

$$\frac{c}{c_0} = \frac{im - im_0}{im_1 - im_0},\tag{3.6}$$

where im_1 is the matrix representing the image collected when only the tracer at concentration c_0 is present, so that c/c_0 does not depends on the estimation of the parameter s.

3.2.2 Colored tracer

The second tracer we use is a solution of methyl blue dye (Sigma Aldrich) of concentration $c_0 = 0.15$ mg/l. The solution is prepared with a mixture of milliQ water (80%) and glycerol (20%) whose

viscosity is $\mu = 0.0019$ Pa s. Once a sample of this solution is irradiated with light, only a portion of the signal passes through it while portion of it is absorbed: the more concentrated is the tracer, the more light is absorbed and the less of it is transmitted. The light absorbance, the logarithm of the ratio between incoming and transmitted light, is a linear function of the tracer concentration according to the Beer-Lambert law [98]. The exponential dependence of the transmitted light to the concentration can be simplified as linear for low concentrations, so that:

$$\frac{c}{c_0} = \frac{im_0 - im}{im_0 - im_1},$$

(3.7)

where $im = im(c)$ is the transmitted light intensity through the tracer at concentration c (and detected by the camera), $im_0 = im(c = 0)$ and $im_1 = im(c = c_0)$. To increase the light contrast between the light passing through the tracer and the light passing through the water-glycerol solution, we filter the irradiating light with a customized filter (Semrock single-band band pass filter 662 ± 11 nm), so that only near-blue light reaches the sample.
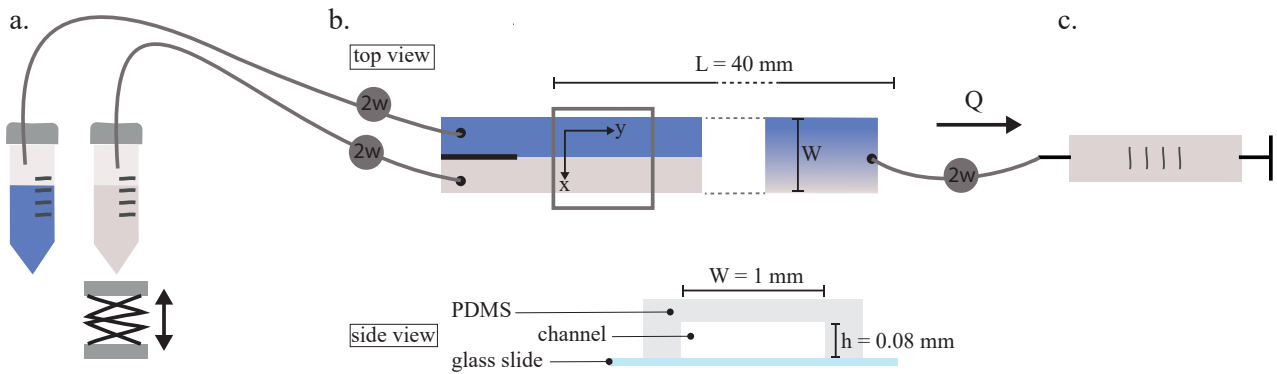
Figure 3.1: Set-up for diffusion experiment where we optically measure the diffusion profile of a solute tracer in a microfluidic channel. *a*. Reservoirs for tracer and blank solution, one reservoir is placed on a laboratory jack to adjust water level and ensure equal head between the two; *b*. Side view: cross-section of a microfluidic chip male of a PMS channel sealed to a microscopy glass slide, the channel dimensions are height $h = 0.08$ mm, width $w = 1$ mm; top view of the channel: length $L = 40$ mm, the gray rectangle indicates the position of image acquisition, in the y direction fluids have a velocity u_y, in the x direction $u_x = 0$ and molecules are displaced by diffusion only, close to the inlet the front between the tracer and blank is sharp while further downstream it is more diffused; *c*. Syringe pump in withdraw mode creates a flow Q in the channel, the flow direction in the system is indicated by the black arrow. Reservoirs, channel and syringe are connected using Tygon tubes.

3.2.3 Flow cell

In order to reproduce the conditions for which a tracer is diffusing along one dimension and compare its concentration profile to the solution of Eq. (3.3), we build a microfluidics device where we continuously inject, side by side, the mentioned tracer solution/suspension together with its solvent (in the following called blank solution). Thus, we design a channel mold with rectangular cross-section and a parallel injection entrance for the two solutions (Fig. 3.1). In this flow cell, the solutions flow happens along the channel main direction only: thus, the only mass transfer mechanisms in the transverse direction is molecular diffusion. The cell geometry is printed onto transparent glass at high resolution in chrome (JD Photodata, UK). Micro-channels are fabricated using standard techniques of soft lithography and PDMS molding, they are then plasma-bonded it to a 1mm thick soda-lime glass slide. The resulting channel has width $w = 1$ mm, thickness $h = 0.08$ mm, thus a cross section A = 0.08 mm^2, and a length $L = 40$ mm (see Fig. 3.1).

Each inlet is connected with Tygon tubing (internal diameter of 0.5 mm) to a reservoir (15 ml Falcon tubes), one containing 4 ml of the blank solution, the other 4 ml of tracer solution. The outlet is connected to a waste reservoir containing 4 ml of water. Tubing connecting the microfluidic chip to the reservoirs can be open/closed at will by means of 2-ways microfluidic valves (MaxWire from Elveflow), all three reservoirs are pressurized using a pressure controller (OB1 MK3+ from Elveflow) so that the flow is established by a pressure drop between inlet and outlet of $\Delta p = 50$ mbar. Once the flow is interrupted (by closing simultaneously all valves and stopping the pressure drop) the tracer diffuses transversely towards the blank solution (and viceversa the black solution diffuses towards the tracer): in this configuration the one-dimensional tracer concentration profile along the channel transverse direction is solution of eq. (3.3). The tracer diffusion coefficient D is, then, obtained, by fitting the solution of eq. (3.3) to the measured concentration profile, using D as the only fitting parameter.

3.2.4 Optical system and image processing

The microfluidic device is placed under a microscope (an inverted Nikon Eclipse Ti-E2) equipped with a low numerical aperture (NA = 0.3) objective in order to observe in focus the whole depth of the channel. Gray-scale images are captured and stored using a Nikon DS-Qi2 camera. Each image is composed by 4908×3264 pixels whose physical size in the camera sensor is $7.3\,\mu$m: thus, considering the objective magnification used (objective 10X plus the internal microscope 1.5X extra magnification, for a total of 15X), an overall size of 2.3×1.6 mm. The images acquired are matrices
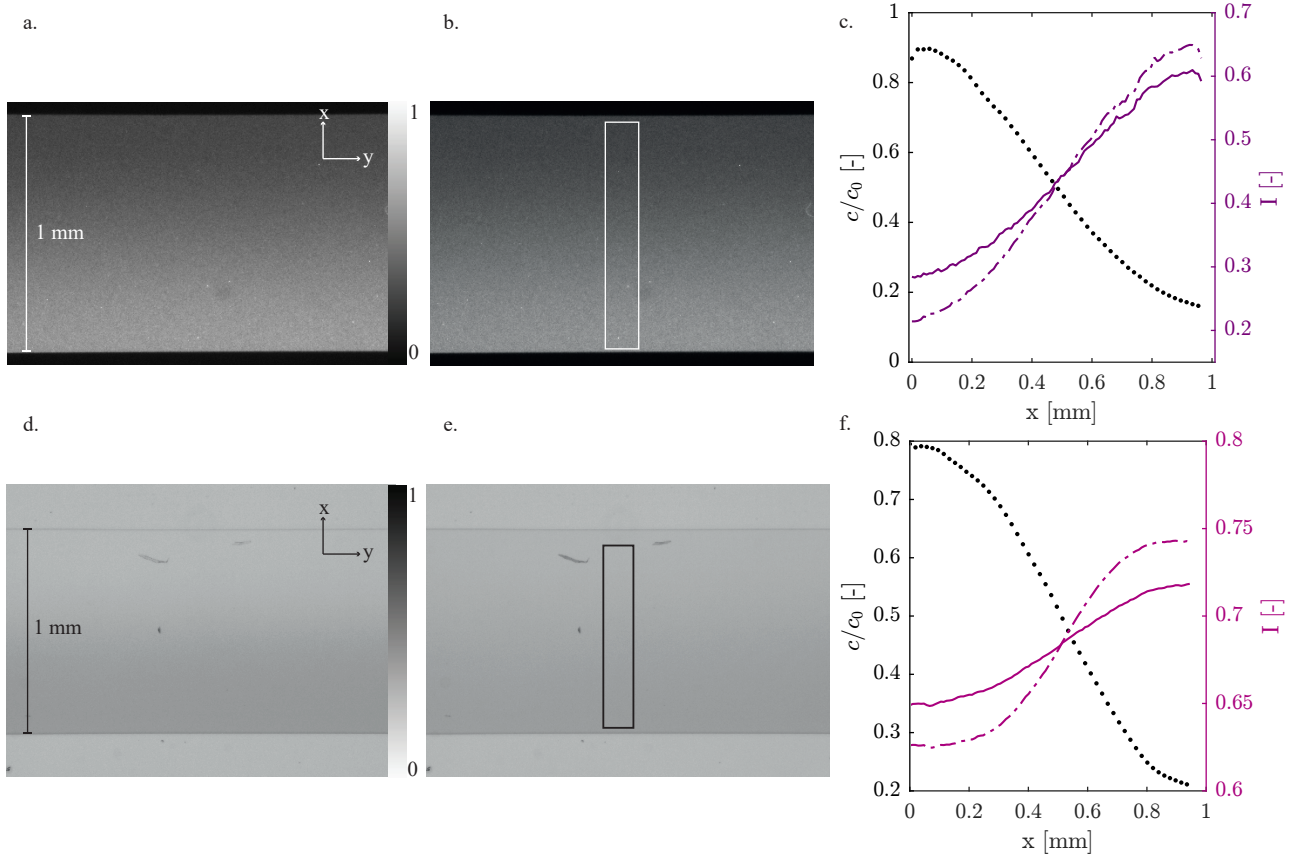
Figure 3.2: Microscopy images of the channel with 15x magnification optic, images are rescaled by pixel depth. Fluids are flowing in the *y*-direction and tracer diffuses in *x*-direction. For fluorescent particle tracer: *a*. Initial image, im0(c =0) and im1(c = 1) are light intensity values in the red rectangles, *b*. Experiment image im, the profiles are obtained by summing pixel values of the red rectangle in the y-direction, *c*. Light intensity profile of initial image (dashed line), im (solid line), resulting concentration profile according to Beer-Lambert law (dots) c = (im - im0) / (im1 - im0). Equivalent information for the methyl blue dye is given in *d*., *e*. and *f*., the resulting concentration profile is given by c = (im0 - im)/(im0 - im1).

of pixels whose value ranges from 0 to $2^{12} - 1$. Then, we crop each image to a desired region of interest (red rectangle in Fig. 3.2 *a* and *b*) which goes from wall to wall of the microfluidic and spans 300 pixels longitudinally (along the flow direction, *y*). Profiles (Fig. 3.2 *c*) are then obtained by averaging values along *y*-direction, within the region of interest.

3.2.5   Theoretical estimate of D

The polystyrene particles diffusion coefficient D can be theoretically estimated with the Stokes-Einstein relation [53] which applies to spherical objects Eq. (3.4). Working at $T = 293$ K with a suspension of viscosity $\mu = 1.06\,10^{-3}$ Pa s and particles of size $r = 7.5\,10^{-8}$ m, the diffusion coefficient is estimated as $D_b = 2.7\,10^{-6}$ mm^2/s. Even though methyl blue molecules present a non-spherical structure, closer to a sheet (much thinner than wide), we can define an effective radius $\bar{r} =$

$6.5\,10^{-10}$ m [99, 100, 101], the dynamic viscosity of the water-glycerol mixture is $\mu_m = 1.98$ Pa s and, thus, we estimate $D_m = 1.7\,10^{-4}$ mm^2/s. For each tracer, the characteristic time of diffusion $\tau_D = L^2/D$ over the channel width $L = 1$ mm represents the upper limit for the concentration gradient smoothing and its decay of mass flux, homogenizing its profile. Thus, the measurement must be performed over a much shorter time scale. For the beads $\tau_D = 1/2.7\,10^{-6}\,3.7\,10^5$ s ~ 100 hours; for the methyl blue $\tau_D = 1/1.7\,10^{-4} \sim 5900$ s ~ 1.6 hours. For a confined condition it has been shown and discussed in chapter two that the characteristic time for the exponential gradient decay is τ_D/π^2, thus about 10 hours for the beads and about 10 minutes for the methyl blue tracer.

3.2.6 Solution of diffusion equation

Since the fluid flow is stopped by closing the valves, the tracer is diffusing within the space of length L between the microfluidics solid and impermeable boundaries, i.e the PDMS walls: thus, the concentration profile that we measure is solution of the diffusion equation (Eq. (3.3)), with no-flux boundary conditions, as derived in [102]:

$$c(x,t) = \sum_{m=1}^{\infty} B_m \cos(\pi\,m\,x/L)\,e^{-\pi^2\,m^2\,D\,t/L^2} + cf,\qquad(3.8)$$

where $c_f = 1/(2L)$ is the homogeneous concentration reached at times larger than the characteristic diffusive time scale over the channel width $\tau_D = L^2/D$ and B_m a coefficient that depends on the initial concentration distribution $f_0(x)$:

$$B_m = 2\int_0^1 f_0(x)\,\cos(\pi\,m\,x)\,dx.\qquad(3.9)$$

Note that the initial condition $f_0(x)$ corresponds to any concentration profile collected at given time t_0 for which it will be imposed that $t_0 = 0$. Thus, the initial profile can be chosen at convenience. Exploiting the matlab function *lsqcurvefit*, we fit for each time step t_j the analytical solution $c(x_i, t_j)$, Eq. (3.8), to the measured concentration profile that we label $c_M(x_i, t_j)$ by varying the only parameter D until it is reached the minimum of the mean-squared error

$$\text{MSE} = \frac{1}{N}\sum_{i=1}^{i=N}\left(c(x_i, t_j) - c_m(x_i, t_j)\right)^2,\qquad(3.10)$$

where N is the number of points over which the concentration profile is detected (number of pixels along the transverse direction within the region of interest). We estimate the measurement uncertainty on the value of D as the ratio between the standard deviation σ and the mean $\overline{D}$ defined

as:

$$\overline{D} = \frac{1}{n} \sum_{j=0}^{j=n} D_j; \quad \sigma = \sqrt{\frac{1}{n} \sum_{j=1}^{j=n} \left(D_j - \overline{D}\right)^2}, \tag{3.11}$$

where n is the number of time steps (or samples collected), D_j the fitted value of D at time $t = t_j$.

3.2.7 Dilution index

Once the value of diffusion coefficient D has been correctly estimated one can predict the concentration profile $c(x,t)$ at any time and for any initial condition f_0 using Eq. 3.8. The degree of mixing reached by the diffusive system can be described in term of system entropy or dilution index [64]:

$$E(t) = \exp\left(\int c(x,t) \log(c(x,t)) \, dx\right). \tag{3.12}$$

The index increases as the system homogenizes.

3.3 Results

3.3.1 Polystyrene fluorescent particles

We record images of a diffusive front of polystyrene particles over seven hours at a rate of one image per hour, the measured concentration profiles are shows as dots in Fig. 3.3.a, as time increases, the profiles go from light to dark color. The fit of these profiles is superposed as solid lines while the initial condition $f_0(x)$ is shown as black dashed line. For this data set the MSE between fitted and measured profiles is on average, over all times, $2.3 \, 10^{-4}$.

We compute the temporal evolution of the Dilution Index, a diagnostic quantity for the system mixing degree, as defined in Eq. (3.12). In Fig. 3.3.c. is shown the temporal evolution of $E(t)$ for the measured (diamonds) and fitted (solid line) profile. Note that the system entropy increases as the particles diffuses, and it will eventually reach a plateau when the system is completely homogeneous. In Fig. 3.3.b (diamonds) are shown the fitted values of D for each profile and the average value is $\overline{D} = 2.6 \, 10^{-6} \mathrm{mm}^2/\mathrm{s}$ (Fig. 3.3.b black dotted line). The standard deviation among fitted values, given by Eq. (3.11), is $\sigma = 8.52 \, 10^{-8} \mathrm{mm}^2/\mathrm{s}$ which indicate a deviation around the mean of 3.3 %. The average value of the measured molecular diffusion coefficient is consistent, within 3 % with the theoretical estimation by the Stokes-Einstein relation, showing that the novel method proposed is accurate.
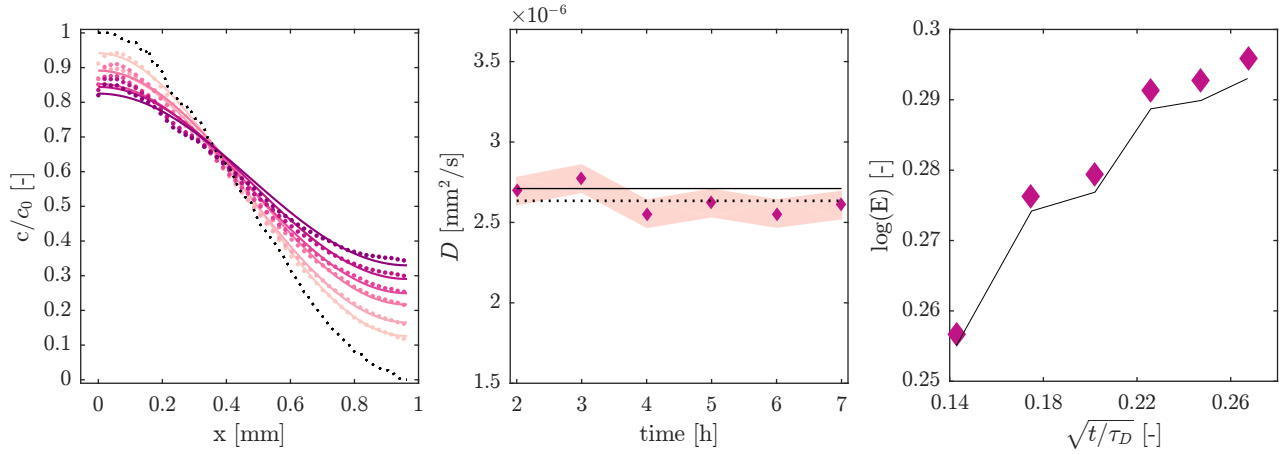
Figure 3.3: *a*. Laboratory measurement of the diffusive concentration profile of polystyrene particles suspension (dots) for six time steps (t = $7.5 \, 10^{-2}$ to $2.6 \, 10^{-1} \, \tau_D$), fitted solution of Eq. (3.8) (solid lines) with initial profile $f_0(x)$ (black dotted line); *b*. Value of fitted diffusion coefficient for each time step (diamonds), mean value $\overline{D}$ (dotted line), theoretical prediction by the Einstein-Stokes relation, Eq. (3.4) (solid black line), standard deviation σ (pink shade area); *c*. Dilution index value E

3.3.2 Methylene blue dye

Images of a methyl blue diffusive front are recorded over 11 minutes at a rate of one image every 50 s, the resulting concentration profiles are given in Fig. 3.4.a, as time increases the profiles are shown from light to dark color. We use the first profile (black dots in Fig. 3.3.a) as initial condition $f_0(x)$ for the fit of Eq. (3.8). The MSE is minimized by the fit to $8.7 \, 10^{-5}$ and we obtain ten values of fitted diffusion coefficient, one per profile, as shown in Fig. 3.4.b (diamonds). The average value (dotted line) is $\overline{D} = 2.4 \, 10^{-4} \mathrm{mm}^2/\mathrm{s}$ and the standard deviation among these fitted values, as defined in Eq. (3.11), is $\sigma = 4.89 \, 10^{-6} \mathrm{mm}^2/\mathrm{s}$ which indicates a deviation around the mean of 2 %. The measured value of the diffusion coefficient is 70% higher than the prediction of the Stokes-Einstein relation using the effective radius $\bar{r}$.

3.4 Discussion

The novel method presented here allows to measure the diffusion coefficient D of a tracer (dissolved or suspended) through a direct visualization of its concentration profile dynamics. The measured profiles are fitted with the solution of diffusion equation, with the single fitting parameter D. We calibrated the method measuring the diffusion coefficient of a suspension of identical spherical particles for which the Stokes-Einstein relation provides a theoretical estimate. Our results show that the method is accurate: for our test tracer the discrepancy between the measured and the theoreti-
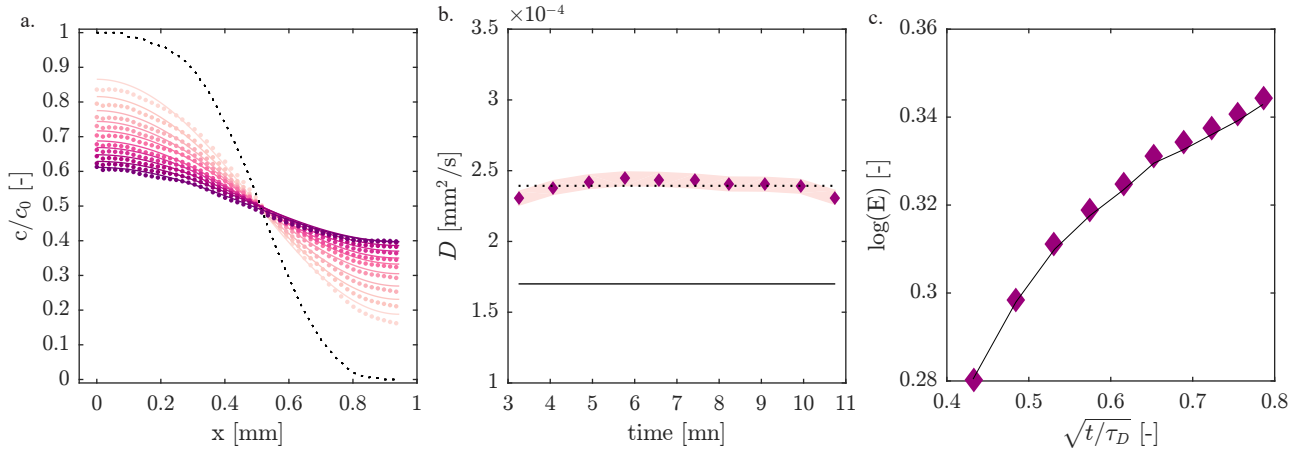
Figure 3.4: *a*. Laboratory measurement of the diffusive concentration profile of methylene blue (dots) for eleven time steps (t = 0.14 to 0.58 τ_D), fitted solution of Eq. (3.8) (solid lines) with initial profile $f_0(x)$ (black dotted line), *b*. Value of fitted diffusion coefficient for each time step (diamonds), mean value $\overline{D}$ (dotted line), standard deviation σ (pink shade area), estimation of D based on effective radius $\bar{r}$ using the Einstein-Stokes relation Eq.3.4; *c*. Dilution index value E

cal value of the diffusion coefficient is smaller than the method uncertainty of 3%. While we show that for non-spherical molecules or colloids using an effective radius to theoretically estimate the diffusion coefficient can lead to a substantial error, we demonstrated that in the case of methylene blue the value of D is underestimated by 70 %.

Moreover, the low standard deviation σ between the measurement over several profiles (collected at different times) implies that also with two concentration profiles (one for the initial condition and one for the fit) could be enough to determine a measurement of D. Due to the non linear shape of the concentration profile, we anticipate that it is better to collect profile data when the front is not too sharp and not too diffused. In fact, the fit MSE becomes larger as the profile flattens or is too steep, since there are less points over which the fit can be done: in other words, there are more concentration values that are equal (or very similar, i.e plateau on the profile edges).

Chapter 4

Impact of confinement on mixing within porous media front: laboratory experiment

4.1 Introduction

As discussed in Ch.1 one, to investigate and quantify pore scale mixing processes is crucial to properly describe systems in which biological or chemical reactions are involved, in particular to predict reaction rates and estimate their product mass. Recent technological development allowed to improve visualization of pore scale processes, using real three dimensional rock structure [12] or synthetic replicate of porous media [79, 35, 103] numerous studies tackle the question of solute transport, reactive transport and mixing considering the micro-scale heterogeneity of the flow field. However, to the best of our knowledge, no study have yet been carried to measure and describe the effect of grains and the no-flux boundary condition they impose locally on mass transport, on the overall mixing dynamic.

Experimentally two main challenges arise: i) to visualize the concentration field over a sufficiently large number of pores so that it experiences both stretching and coalescence regime [22] and ii) to work at relatively low Pe number, where diffusion impact mixing substantially, which is representative of natural systems where pore flow velocity can be very low. Both points rise technical challenges: i) the time to acquire an image covering a large domain (still ensuring high resolution of the inner-pore space) should not exceed the time for the front to travel over more than one pore size, strictly speaking the concentration front should not move "too much" during image acquisition and

ii) if diffusion is important with respect to advection, then mixing happens very fast within pores and it is not possible to capture the concentration field in a non well-mixed state at the pore scale, therefore diffusion coefficient value, pore geometry and flow rate must be carefully tuned in order to observe the temporal evolution of a concentration field where diffusion compete with advection to limit mixing.

We developed a novel experimental set-up to measure at high spatial resolution a concentration field being displaced within synthetic heterogeneous porous medium. In particular, it allows to observe the heterogeneous distribution of concentration within pores, with 100 pixels covering the length of an average pore throat size, and thus, to witness the effect of the impermeable grains on these concentration distributions and the development of the front on a longitudinal distance of tens of characteristic pore throat sizes. We show that pore scale mixing processes cannot be described by the cutting edge models developed for Darcy scale flow field [72, 22] since they do not consider the presence of impermeable and solid boundaries, the grains.

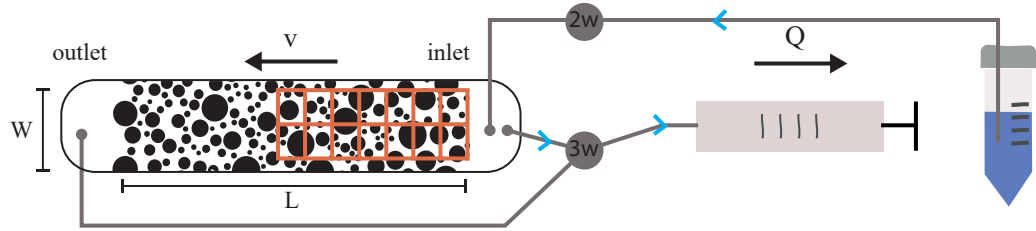## 4.2 Pore scale measurements of concentration field

4.2.1 Flow cell

To investigate the fate of an invading front of a conservative (i.e. non-reactive) solute subjected to diffusion and flow heterogeneity, we use microfluidic techniques to design a synthetic replicate of a porous medium. The two-dimensional pore geometry is built by randomly positioning disks (representing solid grains) of various diameter such that the pore throat size (the smallest distance between two neighbor disks) is statistically distributed like a decreasing power-law; within a range of values between $10 - 500 \, \mu$m with an average of $\lambda = 124 \, \mu$m. The microfluidic chamber is fabricated using standard techniques of soft lithography and PDMS molding [104], then plasma-bonded to a 1 mm thick soda-lime glass slide. Finally, the chamber has width $W = 7$ mm, length $L = 50$ mm, thickness $h = 0.05$ mm, cross-section area $A = 0.35$ mm^2 and porosity $\phi = 0.47$.

To initiate the flow a 500 μL glass syringe (Hamilton gas tight), driven by a syringe pump (Harvard Apparatus, PHD 2000), is connected to a series of valves allowing formation of a sharp front injection of the tracer solution into the chamber (see Fig. 4.1), previously saturated with a blank solution. The syringe, valves and chamber are connected with Tygon tubes (internal diameter 0.5 mm). Two reservoirs (one is the glass syringe itself, containing the blank solution, the other is a falcon tube

containing the tracer) are connected to the inlet of the chamber, a second inlet is used to clean the injection area by recirculating the tracer before it enters the porous medium, and the overall flow is established by withdrawing fluid from a single outlet. The pump is set to withdraw at a constant flow rate of $Q = 5\,10^{-3}$ μL/s, which corresponds to a pore scale, average velocity, of $v = Q/(A\,\phi) = 0.02$ mm/s.
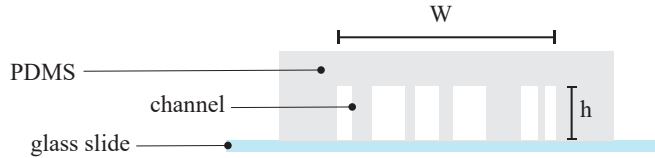

Figure 4.1: Experimental set-up to visualize the displacement of a concentration field in a synthetic porous medium and measure pore scale concentration values. *a.* Porous medium replicate geometry of length L = 50 mm: black disc stands for the grains, orange grid indicates image acquisition pattern; blue falcon tube is the tracer reservoir which is open/closed by a 2-way valve, the syringe is filled with blank solution and placed on a pump to trigger the flow, inlet and outlet of the chip are connected to a 3-ways valve which allows cleaning of the injection area, blue arrows indicate the cleaning circuit, v = 0.02 mm/s indicates the average flow velocity within the porous media, $Q = 5\,10^{-3}$ μL/s the pump withdraw rate; *b.* Cross-section of the porous medium: a PDMS channel (gray area) of dimensions W = 7 mm and h = 0.05 mm, with pillars for the grains, is plasma bonded to a microscopy glass slide, white areas between the gray pillars indicate the pore space.

4.2.2 Tracer

In order to optically measure the concentration field of a displacing scalar, we choose methylene blue (Sigma Aldrich). The measurement principle is the following: once a light source is homogeneously irradiating the sample, only portion of it will pass through reaching the camera: the more concentrated is the tracer, the more light will be absorbed and the less of it will be transmitted. The light transmittance (the ratio between the incoming and the transmitted light) is a non-linear function of the tracer concentration and it is typically described by the Beer-Lambert law [98]:

$$I = I_0\, e^{-s\,c} + I_b, \tag{4.1}$$

where I_0 and I are respectively the irradiated and transmitted (thus detected) light, c is the tracer concentration, I_b is the background light signal (the light detected when the tracer is highly concentrated thus, blocking most of the irradiating light) and s a parameter that depends on the physico-chemical properties of the solution. For a diluted solution, where $c < 1/s$, the relation simplified and becomes linear, it can be reduced to:

$$I = I_0(1 - s\,c) + I_b \quad \text{thus,} \quad c = \frac{1}{s}\left(\frac{I_0 + I_b - I}{I_0}\right). \tag{4.2}$$

To avoid a cumbersome calibration procedure, required to determine s, and get rid of the unknown
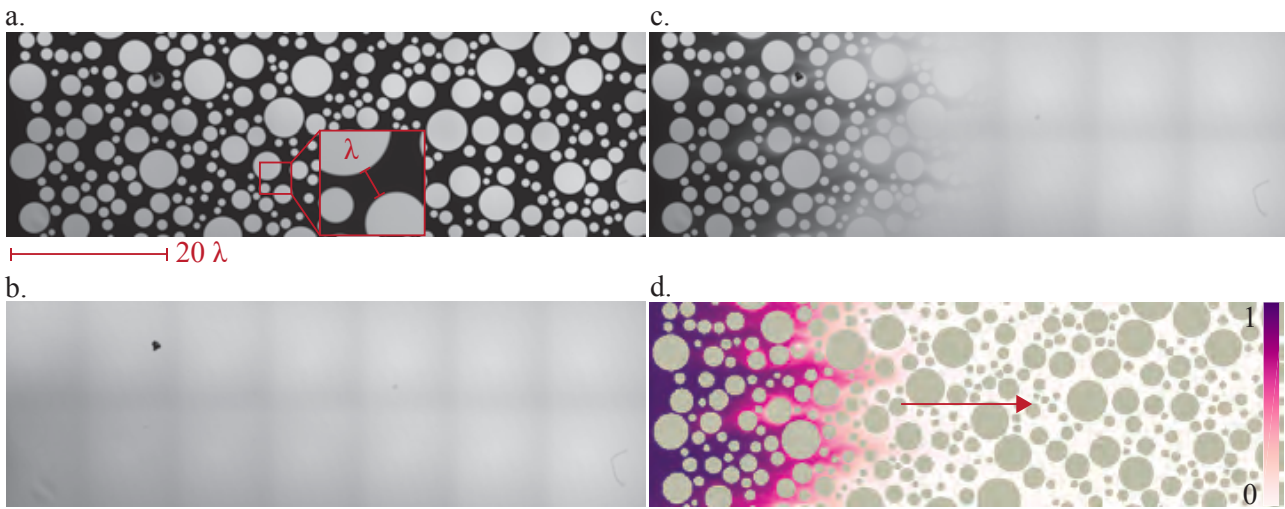
Figure 4.2: Light intensity and concentration fields of an invading tracer in a porous medium geometry, the gray disks represent the grains and the space between then the pores. *a.* Light intensity field when the medium is saturated with tracer, in the zoom-in view λ indicates a characteristic pore throat size; *b.* Light intensity field at initial time, there is no tracer and the chamber is filled with blank solution; *c.* Light intensity field of the invading tracer at t = 32 τ_a; *d.* Concentration field at t = 32 τ_a, the arrow indicates flow direction.

values I_0 and I_b, we express c with respect to the initial concentration c_0. Defining $im0$ as the light intensity measured when $c = 0$ (Fig. 4.2.b.) and $im1$ the one when $c = c_0$ (Fig. 4.2.a.), Eq. (4.2) gives $im0 = I_0 + I_b$, we have:

$$c = \frac{1}{s}\left(\frac{im0 - I}{I_0}\right) \quad \text{and} \quad c_0 = \frac{1}{s}\left(\frac{im0 - im1}{I_0}\right), \tag{4.3}$$

and finally we get the concentration value (Fig. 4.2.c.) as:

$$\frac{c}{c_0} = \frac{im0 - I}{im0 - im1}. \tag{4.4}$$

To define the relative importance of flow disorder and molecular diffusion, we consider the Péclet number, defined as the ratio between the characteristic diffusion time over the average pore throat size λ and the characteristic time for the average fluid velocity v to displace fluid over λ: $Pe = \lambda\, v/D$, where D is the diffusion coefficient of the tracer. Considering the average pore size in the medium ($\lambda \sim 124\,\mu$m), the diffusion coefficient D is tuned in order to observe a competition between diffusion and stretching for transport over several pores: $Pe > 10$. To do so, the tracer solvent is a mixture of milliQ water (30%) and glycerol (70%), that is about 40 times more viscous than water, so that the diffusion coefficient is lowered by 40 times with respect to its value in water: given $D_{wat} = 4.8\,10^{-4}$ mm^2/s, extrapolated from the value measured in Ch. 3 for a water-glycerol mixture of ratio 80%-20%: $D = 1.2\,10^{-5}$ mm^2/s. The tracer concentration dissolved into the water-glycerol mixture is $4.3\,10^{-3}$ g/mL.

4.2.3 Optical system and image processing

The microfluidic chip is placed under an inverted microscope (Nikon Eclipse Ti-E2) equipped with a 4x magnification objective with low numerical aperture (NA = 0.3) in order to observe in focus the whole depth of the chamber $h = 0.05$ mm. Gray scale images are captured at 16-bits color depth with a Photometrics Prime95B camera. The pixel size is 11μm. To cover a significant number of pores we acquire a large image composed of 7x2 individual images stitched together. The resulting image, considering the magnification used, has a size of l x w = 10.6 x 3.2 mm, this correspond to $81\,\lambda$ along the flow direction and $24\,\lambda$ along the transverse one. Each image is a matrix of pixels whose value ranges from 0 to $2^{16} - 1$. We add to the light path a band-pass filter centered on the peak transmission wavelength of the tracer (Semrock single-band band pass filter 662 ± 11 nm) to get a better contrast.

For the designed experimental conditions, the relation between detected light I and concentration c is linear, thus, the uncertainty propagation of I, whose information is stored into the matrix im, on the concentration value can be estimated following standard error analysis [105]: the normalized concentration c/c_0 relative uncertainty is equal to the one on I. We assess the light intensity relative uncertainty σ_I/I as the standard deviation of the matrix $im1$ divided by its own average $\sigma_{im1}/\overline{im_1}$ which is 0.3%. Thus, we convert the light intensity into a concentration field through eq. (4.4) and we set to zero all concentration values below $c_m = 3\,10^{-3}\,c_0$ and we set to one all values above $1 - c_m$.

4.2.4 Procedure

Before being used for an experiment, each microfluidics chip is placed in a vacuum chamber for 10 minutes, to deplete the air from the PDMS (which is porous and permeable to gas) allowing its saturation after the first liquid injection. The chip is first saturated with a blank solution, the water-glycerol mixture containing no tracer, then, the injection area is cleaned through a re-circulation procedure following the one descried by [15]: for 20 s the tracer flows, at flow rate $0.05\,\mu$l/s, from the reservoir to the syringe without entering the porous medium ensuring pure concentration within the tube and maximizing it within the injection chamber (see blue arrows in Fig. 4.1). The syringe is reset to experimental flow rate Q, the 3-ways valve is switched to allow the flow toward the porous medium outlet and the tracer solution is continuously injected, producing an initially sharp front with the defending fluid, while image acquisition starts. The acquisition of one large image, made of 7×2 single images stitched together, takes 5 s, after which a new image acquisition starts immediately. Exposure time is set to 1 ms.

4.3 Results

For the designed conditions, the system Péclet number would classically defined as $Pe = \lambda v / D = 206$. However, the characteristic time of diffusion in such a confined space is $\tau_D = \lambda^2 / (2\,D\,\pi^2) \sim 65$ s as we show in Ch. 2, thus, since the characteristic time of advection over a pore throat $\tau_a = \lambda / v = 6.2$ s, we estimate the Péclet number as $Pe = \lambda\,v / (D\pi^2) = 21$. Looking at the macroscopic scale of the whole porous system, the characteristic time of advection over one pore volume $\tau_{pv} = l / v = 530$ s (about $85\,\tau_a$). The acquisition of one large image lasts for about 5 s which is close to τ_a, ensuring that the front will not travel much more than one pore throat length during capturing and stitching process. We analyze the concentration field from $t = 0$, when the entire front enters the field of view, to $t = 56\,\tau_a$, time at which the foremost front tip begins to leave the field of view: 49 time steps in total.

Figure 4.3 shows four snapshots of the normalized concentration c/c_0 at times $t = 8$, 15, 28 and $41\tau_a$. We designed this experiment to get the invading front as sharp as possible: however, the solute experiences some dilution within the microfluidics, just prior entering the porous system on the left-hand-side of the field of view during the cleaning and re-circulation phase. Thus, the front enters the porous system with some initial longitudinal dispersion, a process that occurs anyway while passing through the porous medium.

The no-slip boundary condition taking place at the impermeable grains walls induces a flow hetero-geneity within the microfluidic chamber: the middle point of each pore throat has a higher velocity than the rest of it with a profile, from grain wall to grain wall, that is approximately parabolic [28]. This happens because we designed the flow cell so that the thickness of the cell is not governing flow and mass transfer, the ratio between a pore throat and the chamber vertical gap is on average close to one, so that we find the parabolic profile in both directions. The experiment last for about 6 mn which is much shorter than the diffusive time over the channel thickness $h^2/D = 20$ mn ensuring that Taylor dispersion do not occur. Due to the flow heterogeneity, the invading front experiences stretching and it gets deformed to pass through the tight and confined space of the pores. There, the competition between fluid stretching and molecular diffusion controls the local concentration transport and the consequent mixing dynamics.

To quantify the macroscopic (landscape size) transport properties, we consider the longitudinal con-centration profile, which is the transverse average $P(x)$ of c/c_0. For each time step we compute $P(x)$, as shown as a black line on Fig. 4.3 superposed to the concentration fields): as a first approximation this quantity can be modeled using the classical advection-dispersion equation:

$$\frac{\partial P}{\partial t} = -v\,\frac{\partial P}{\partial x} + D^\star\,\frac{\partial^2 P}{\partial x^2},\tag{4.5}$$

with $D^\star$ an unknown dispersion coefficient, a macroscopic measure of solute spreading which scales

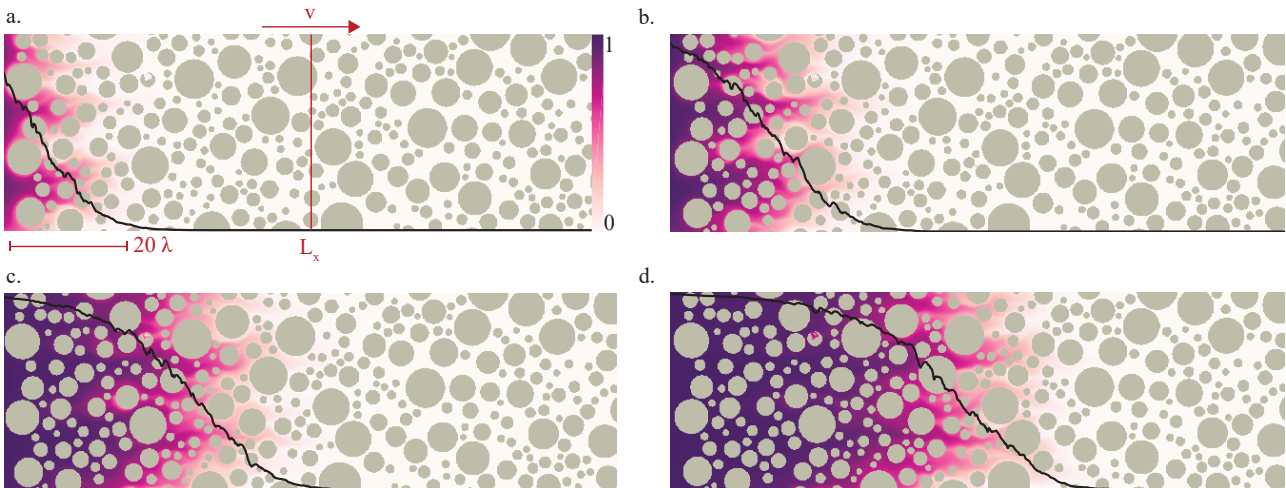Figure 4.3: Normalized concentration field c/c_0 of invading front in a porous medium structure; gray discs stand for solid and impermeable grains, area between them for the pore space, red arrow indicates flow direction, vertical red line position L_x where the break-through curve (BTC) is computed; $Pe = \lambda v/D = 219$. $a - d$ are snapshots at time: $t = 8, 15, 28$ and $41\tau_a$, respectively.

as *Pe* [65]. The solution to the previous eq. 4.5 is, for a sharp injection, given by [2]:

$$P(x,t) = \frac{1}{2} \left[1 - \text{erf} \left(\frac{x - x_0}{\sqrt{4 \, D^\star \, t}} \right) \right].$$ (4.6)

where $x_0 = vt$ is the averaged front position, the longitudinal position where $P = 1/2$. We fit Eq. 4.6 to the measured concentration profile, where $D^\star$ is the only fitting parameter. The measured and fitted profiles are presented in Fig. 4.4.b. By fitting these profiles over the 49 time steps, we obtain an average value for $D^\star = 8.9 \, 10^{-3}$ mm$^2/s$.
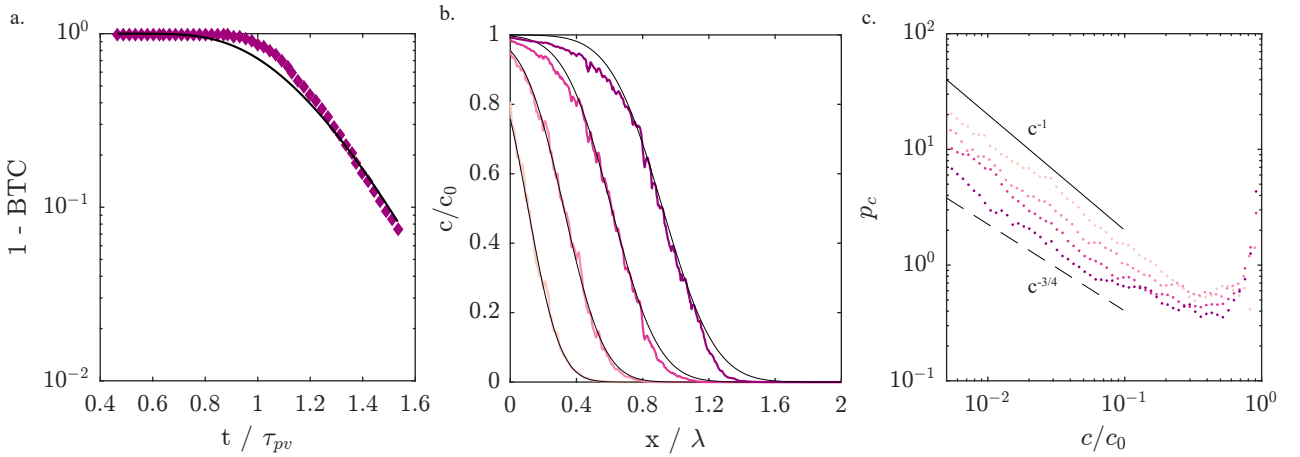

Figure 4.4: Transport measures of a concentration field invading a porous medium structure (Fig. 4.3). *a*. Complementary BTC recorded in the middle of the domain at location L_x, time is normalized by the advective time over a pore volume; *b*. Longitudinal projection of concentration field (Figs. 4.3.a.-d.), for time t = 17, 24, 33 and 41 τ_a, time increase from light to dark colours, black solid lines are given by Eq. 4.6 with $D^\star$ as fitting parameter, the averaged value obtained over all time steps is $D^\star = 8.9 \, 10^{-3}$ mm$^2/s$; *c*. PDF of concentration field shown in *a.*, *b.*, *c.* and *d.* with time increasing from light to dark colours, black solid line indicate a c^{-1} scaling for early time and black dashed a $c^{-3/4}$ scaling for later ones.

Another classical diagnostic quantity used to quantify transport in porous systems [65] is the breakthrough curve (Fig. 4.4.a.) which is the time series of the normalized and averaged concentration (along the transverse direction) at a defined downstream location L_x (see Fig.4.3a), in our case the middle of field of view. The BTC can be modeled using the advection-dispersion equation 4.6 $c(x = L_x, t)/c_0$ using the value of $D^\star$ previously fitted on the longitudinal projection of the concentration field. The model prediction is given as a black solid line in Fig. 4.4a and characterizes well the observed solute BTC.

The concentration field can also be described in term of its concentration distribution, i.e the normalized frequency of occurrence of concentration values in given ranges, also called probability

density function (PDF). For a continuous system (as with a Darcy scale description), at all times the transport concentration PDF is expected to be the same, scaling as $1/c$ for low concentration values, reaching a minimum around $c = 1/2$ and increasing again for larger concentrations. This can be shown by following the lamellar description of mixing proposed by [82, 72, 22]: the concentration PDF can be seen as the superposition of individual lamellas PDF. Considering an invading front (and not a pulse as in [82, 72, 22]), the stretching mechanisms as the effect of modifying the space over which the normalized concentration c/c_0 varies between 0 and 1, but it does not affect the minimum or maximum values in each lamella. Therefore, the superposition of non-overlapping lamellae that experience different stretching results in the same PDF as the one of an individual lamellas whose concentration ranges between 0 and 1 following an error-function like shape (solution of diffusion equation for a front in unconfined conditions, as discussed in Ch.2).

However, as the front travels downstream through the impermeable grains the slope of the distribution changes, it goes from c^{-1} to $\sim c^{-3/4}$. This is shown in Fig. 4.4 c for the same four time steps presented in Fig. 4.3, with time increasing form light to dark color. This is probably the consequence that within pores the lamellas do not follow an error-function like distribution, but, as discussed in Ch.2, the diffusion mechanism within a single pore is affected by the no-flux boundary conditions at the grains wall. Moreover, probably also the fluid stretching, the other key mechanism controlling the mixing dynamics (and, thus, the concentration PDF), is affected by the presence of solid impermeable grains.

4.4   Conclusion

As already demonstrated by [25] at Darcy scale, where the individual pores are not resolved, we observe that macroscopic measurements of displacement and spreading such as longitudinal projection of concentration field and early times BTC are well predicted by the classical advection dispersion models. Observations of transport dynamics for longer times, i.e. the BTC for times much larger than the pore volume time scale, would probably deviate from the advection-dispersion prediction since small concentrations fluctuations, associated to flow heterogeneity, would become important.

Considering as diagnostic quantity for mixing dynamics the concentration PDF, following [66, 72, 22], our measurements show that at pore scale, the presence of solid and impermeable boundaries,

the grains, triggers a different mixing dynamics that affect the concentration distribution statistics which deviates from what it would be expected for an invading sharp front within a continuous non-confined domain. We hypothesize that the key processes of diffusion, stretching and merging of lamellas are affected by the confinement conditions induced by the presence of the grains, impacting the overall mixing dynamics. In order to understand better this complex problem, in the next chapter we explore the powerful tools of numerical simulation to investigate the effect of local stretching in confined media.

As discussed in Ch.2, diffusion is affected by the no-flux boundary conditions at the solid interface. Similarly, stretching is likely to be limited by the presence of impermeable grains. Our results indicate that the confined nature of porous media, in particular the specific boundary conditions constraining flow and transport around the solid obstacles, must be taken into account to correctly predict pore scale concentration field distributions. We suggest that such a model could be derived by extending the lamellar formalism [66, 72, 22] to adapt diffusion and stretching mechanisms to the dynamics of a confined environment.

Chapter 5

Impact of confinement on mixing within porous media: numerical simulations

5.1 Introduction

We consider the fluid flow through two heterogeneous porous media, focusing on different spatial scales, one resolving the detailed structure of the pore space (see Fig. 5.1 *a*. where the gray disks represent solid impermeable grains), but describing only a few tens of them, and the other spanning over tens of thousands of pores, without resolving their structure (see Fig. 5.1 *b*. where the color represent the value of the permeability field *k*).

For the first case, as described in this thesis introduction, chapter 1, the incompressible fluid motion is described in terms of momentum conservation that for the low Reynolds number $Re = \bar{v}\lambda/v$ ($\bar{u}$ is the average fluid velocity across the characteristic length scale λ and v represents the fluid kinematic viscosity) corresponds to the solution of the Stokes equations. For the second case, the larger scale fluid flow $\vec{q}$ description is provided in terms of the Darcy equation (5.2) and a continuous permeability field k, representing the local average pore space.

In both scenarios, once the flow solution $\vec{u}$ or $\vec{q}$ is known, the transport of a dissolved tracer is controlled by the advective displacement and diffusive flux: thus the spatio-temporal evolution of the tracer concentration field c is governed by mass concentration described by the advection diffusion equation (5.7). Neglecting diffusion, the fate of a fluid element transported by the flow field is provided by integrating the motion equations

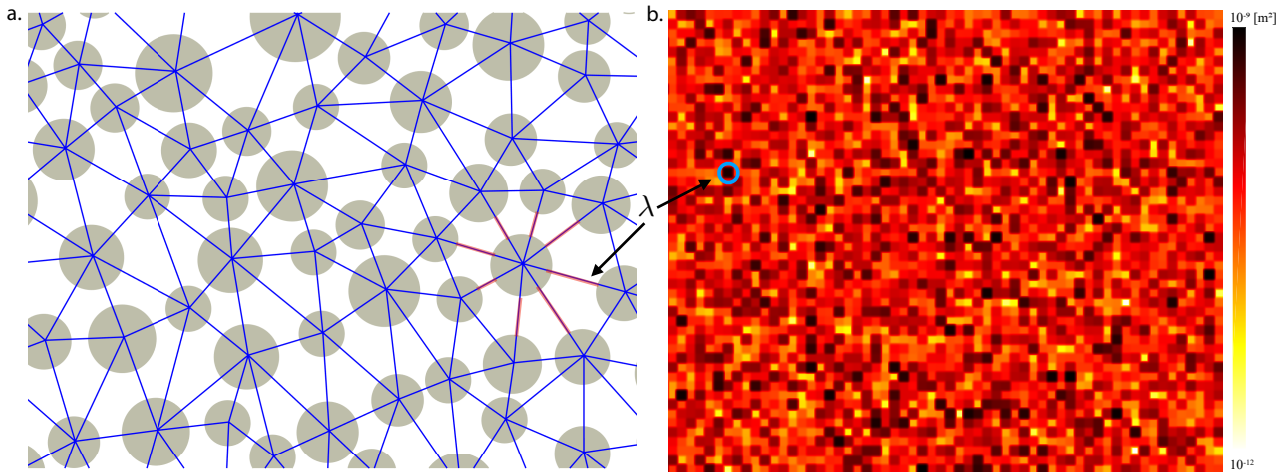$$\frac{d\boldsymbol{x}}{dt} = v[\boldsymbol{x}(t)].$$ (5.1)

Figure 5.1: Porous medium properties. *a*. Small scale: the detailed structure of the grains arrangements (gray disks) is characterized by a Delaunay triangulation (blue segments) connecting neighboring grains. The size λ of each pore throat is defined as the distance between the boundaries of close grains (a few examples around a single grain as red segments). *b*. Larger scale: the porous structure is replaced by a continuous permeability field k, shown with darker colors for higher values. The random value of k at each location is log-normally distributed with a spatial correlation length λ over which the value of the permeability field is almost constant.

5.2 Method

Here, we consider the numerical solution of flow and transport presented in the following were obtained using commercial software COMSOL 5.5. The design of the simulations was done in collaboration with Prof. Luis Cueto-Felgueroso from UPM Madrid. Particle tracking simulations were performed using an in-house code developed by Filippo Miele [106].

5.2.1 Numerical solution for fluid flow and advective transport

Flow solution of the Darcy's law for larger scale

In its natural state water moves in the subsurface and this movement is driven by a pressure gradient. The basic equation governing groundwater flow, for a saturated medium, was formulated by hydraulic engineer Henry Darcy in 1856: the law carrying its name stipulates that the flow rate Q through a porous medium of length L and cross-sectional area A is proportional to the hydraulic gradient across the medium itself (head-loss divided by the flow path length L) as:

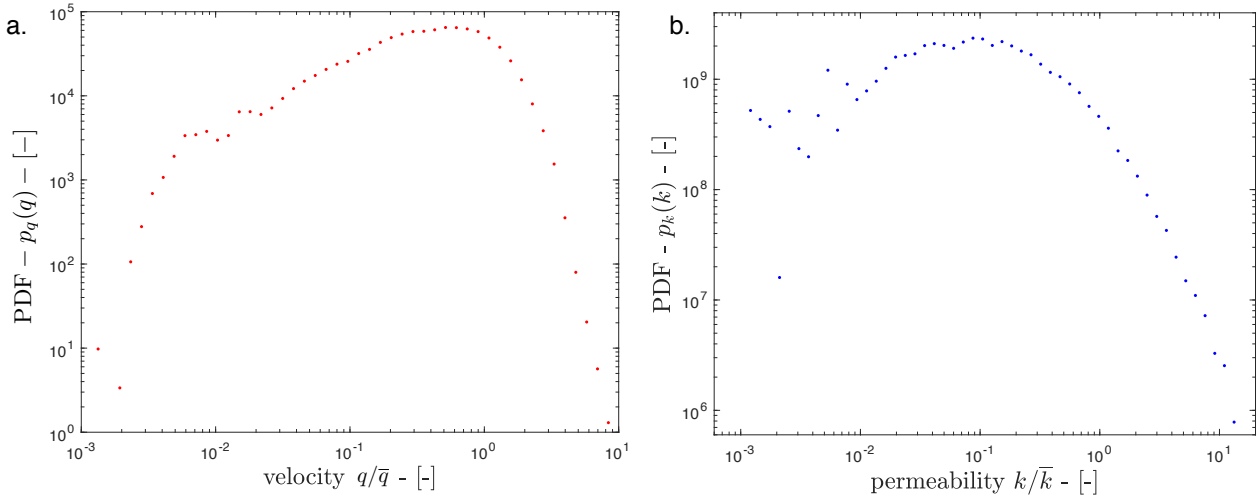$$\frac{Q}{A} = -K \frac{dh}{L} = -\frac{k}{\mu} \nabla p, \tag{5.2}$$

Figure 5.2: Darcy scale field. *a*. Probability Density Function of the velocity magnitude; *b*. Probability Density Function of the permeability field *k*.

where the proportionality constant K [m/s] is the medium hydraulic conductivity, μ [Pa s] the fluid dynamic viscosity, k $[m^2]$ the medium permeability field, p [Pa] the local pressure and Q/A the average (or Darcy) fluid velocity. It describes the ease of a fluid to move through the solid matrix and it is a function of both fluid and medium properties. This important law can be extended to more dimensions, considering the local velocity $\vec{q}$, pressure p and permeability k fields as:

$$\vec{q} = -\frac{k}{\mu}\nabla p. \tag{5.3}$$

We consider the permeability field shown in Fig. 5.1 *b* whose statistical distribution (PDF) is shown in Fig. 5.2 *b* and we impose an average velocity at the medium inlet $Q/A = \bar{q} = 10^{-5}$ m/s (which corresponds to the same average fluid velocity imposed in the experiment described in Ch.4). Moreover, no-slip conditions (zero fluid velocity) are imposed at the top and bottom domain boundaries. The fluid non-compressibility results in a divergence-free velocity field, shown in Fig. 5.3 *a*, for which

$$\nabla \cdot (k\nabla p) = 0. \tag{5.4}$$

We solve Eqs.(5.2) and (5.4) for $\vec{q}$ and p using a finite element scheme; the fluid velocity values are obtained over an irregular mesh nodes and then interpolated on a Cartesian grid of elements of size $1.5\,10^{-4}$ m. The domain is a rectangle of size $L \times W = 1.7 \times 1$ m, which is discretized using a mesh with element size ranging between 10^{-4}m and 10^{-3}m, fluid density $\rho = 1000$ kg/m^3 and viscosity $\mu = 0.001$ Pa s, the resulting Reynolds number is $Re = 0.4$. We generate a log-normal distributed permeability field with permeability values between 10^{-12} m^2 and 10^{-9} m^2 (representing a coarse
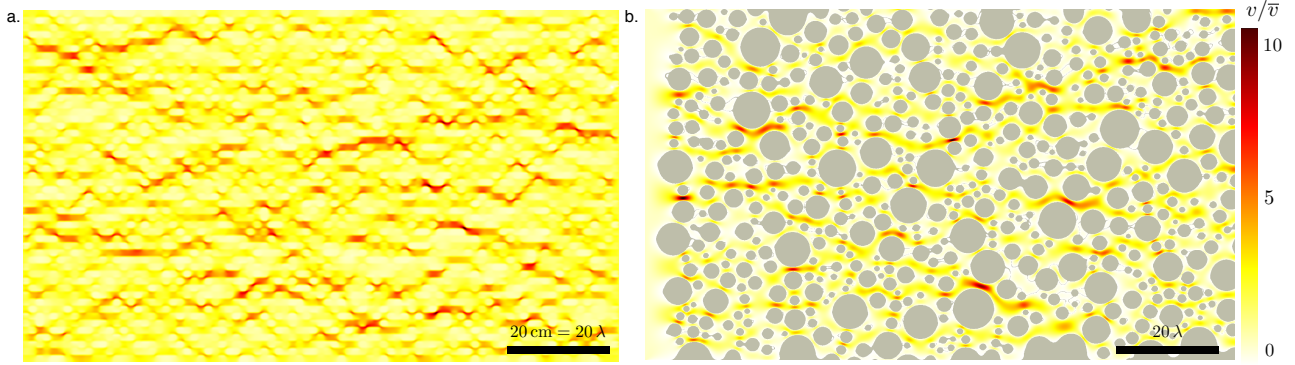
Figure 5.3: Normalized magnitude of the computed velocity fields: *a*. Darcy's flow and *b*. Stokes flow.

sand) [3] and isotropic correlation length $\lambda = 0.02$ m (represented in Fig. 5.1 *b* by the diameter of the blue circle). Using the commercial software COMSOL, we compute the pressure field, the longitudinal and transverse fluid velocity, q_x and q_y respectively. The resulting velocity magnitude as $q = \sqrt{q_x^2 + q_y^2}$ has a statistical distribution (PDF) shown in Fig. 5.2 *a* and it spans a wide range of velocities, similarly to the distribution of permeability field values shown in Fig. 5.2 *a*.

Pore scale medium properties

We consider the porous system as in Fig. 5.1 *a* resolving the solid and impermeable grains, around which no-slip (fluid velocity is zero) boundary condition apply. The pores geometry is similar to the one in [21], whose solid and impermeable structure consists of non overlapping circular disks of random position and radius. This disordered arrangement of disks can be characterized geometrically by constructing a Delaunay triangulation of the disk centers [e.g., 107]: each triangle defines a *pore body* and each edge defines a *pore throat* (a few examples as red segments in Fig. 5.1 *a*). The two-dimensional domain is a rectangle of size $L \times W = 7 \times 10$ mm, which is the same geometry used in Ch. 4 for microfluidics experiments, of characteristic pore throat size $\overline{\lambda} = 130$ μm, given by the average pore throat size, porosity $\phi = 0.47$.

We characterize the statistical properties of the medium through the distribution of pore throat size, $\lambda = d - R_1 - R_2$, where d is the distance between the center of two neighboring disk that are connected by an edge of the Delaunay triangulation, and R_1, R_2 are their respective radii. The random position and size of the disks is characterized by a power law distribution, probability density function (PDF), of their radii $p_R(R) \sim R^{1-2\beta}$, with $\beta = 1.8$, which have been generated to be spatially organized such that the PDF of pore throat size is a power law $p_\lambda(\lambda) \sim \lambda^{-\gamma}$, with $\gamma = 2/3$ with an exponential cut-off for large pores. The considered medium structure is characterized by
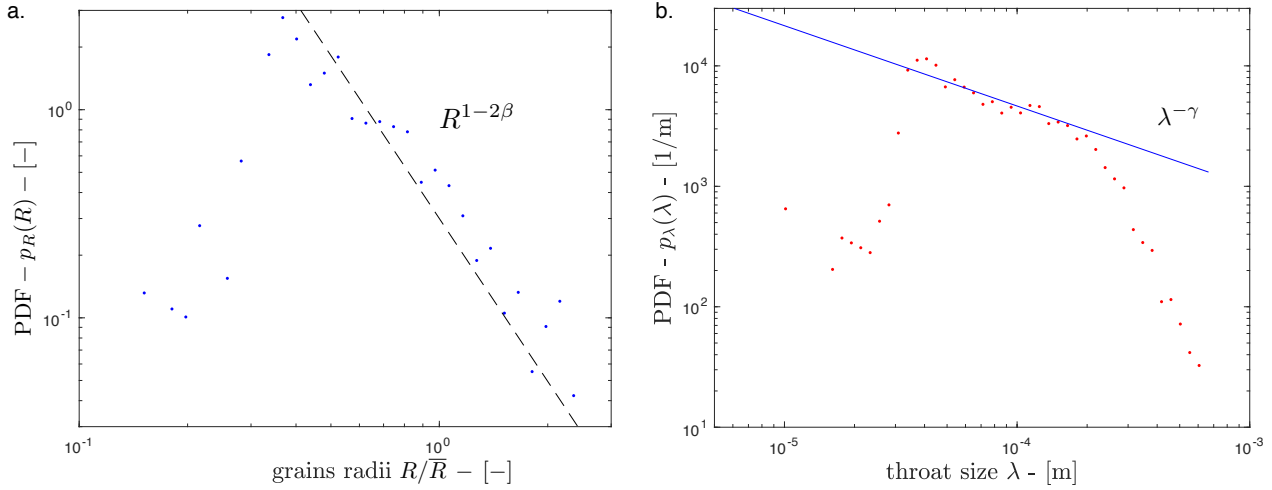
Figure 5.4: Small scale medium properties. *a*. the PDF of the grain radii R, *b*. the PDF of the pore throat size λ defined as the distance between neighboring grains wall.

the grain radii R distribution that, combined with their location, determine the pore throat size λ (represented by red segments in Fig. 5.1 *a*) distribution through which the viscous fluid is forced to pass.

Flow solution of Stokes equations

We consider the same fluid as in our experiments discussed previously in chapter four: a mixture of water and glycerol of density $\rho = 1194 \text{ kg/m}^3$ and viscosity $\mu = 3\,10^{-2} \text{ Pa s}$. Flow equations at this scale are derived considering momentum conservation, for Newtonian fluids they are expressed as a set of partial differential equations: the Navier-Stokes equations. For flow characterized by low Reynolds number (describing the ratio between inertial and viscous effect), typical of confined media, inertia can be neglected (flow is dominated by viscous forces) and the flow problem is reduced to the so-called Stokes equations. Considering an horizontal plane, thus neglecting gravity, we obtain:

$$\nabla p = \mu \nabla^2 \vec{u}, \tag{5.5}$$

We consider the case of an incompressible fluid for which the resulting velocity field is divergence free, or $\nabla \cdot \vec{u} = 0$.

We use the commercial software COMSOL multiphysics to numerically compute the longitudinal and transverse fluid velocity u_x and u_y solving Stokes incompressible flow and we designate the velocity magnitude as $u = \sqrt{u_x^2 + u_y^2}$. The Eq. (5.5) are solved for u_x and u_y over an irregular mesh

with element size ranging between $1.25\,10^{-6}$ m and $1.25\,10^{-5}$ m; then, the fluid velocity values are interpolated over a Cartesian grid with element of $7\,10^{-7}$ m. We impose no-slip conditions (fluid velocity is zero) at the top and bottom domain boundary as well as around the solid grains, a fluid velocity $u = 10^{-5}$ m/s is imposed at the inlet at a distance $\sim 3\,\lambda$ from the first row of grains, resulting in a Raynolds number $Re < 10^{-2}$, verifying a posteriori that the flow is laminar. The magnitude of the computed velocity field is shown in Fig. 5.3 *b*.

The link between the pore throat size λ PDF, capturing the host-medium heterogeneity and the low velocity PDF can be understood modeling the flow, in analogy with pore-network models [e.g., 108, 109], as equivalent to the one within a collection of parallel pipes with different size as in [21, 110]. The fluid velocity through each pore, also called the *porelets*, would be, then, approximated with the one of a pipe: Hagen-Poiseuille flow. While pore-network models focus on the pores contribution to the medium permeability, its overall ability to transmit fluid, the link between medium structure and the low velocity distribution can be established focusing only velocities in the range 10 to 10^4 times smaller than the mean Eulerian velocity, $u/\overline{u} \ll 1$ (with $\overline{u}$ the average pore velocity over the domain): the pores that do not really contribute much to the average velocity value and, thus, on the medium permeability.

In this context, the velocity magnitude through the porous landscape is locally controlled by the smallest openings of size λ: the pores conceptualized as pipes of width λ and length λ, driven by a single effective pressure gradient $\langle \nabla p \rangle$ across the pipe itself. This conceptual framework does not take into account the pores connectivity and it is consistent with the medium isotropy, directionality independence, typical of many porous media [2]. The fluid velocity through a pipe has only longitudinal component [111], and its magnitude has a parabolic profile:

$$u(y) = A \left[\left(\frac{\lambda}{2} \right)^2 - y^2 \right],$$

where $A = \frac{-\langle \nabla p \rangle}{2\mu}$, the maximum velocity, in the middle of the pipe ($y = 0$), is $u_M = A\lambda^2/4$ and the smallest velocity, at the no-slip pipe walls ($y = \pm\lambda/2$), is $u_m = 0$. For a collection of pipes with a given width distribution $\mathrm{PDF}(u|\lambda)$, represents the conditional probability of the local velocity u within a pipe of given width λ. Following [21] the following scaling for the low velocity distribution, controlled by an ensemble of distributed porelets, is

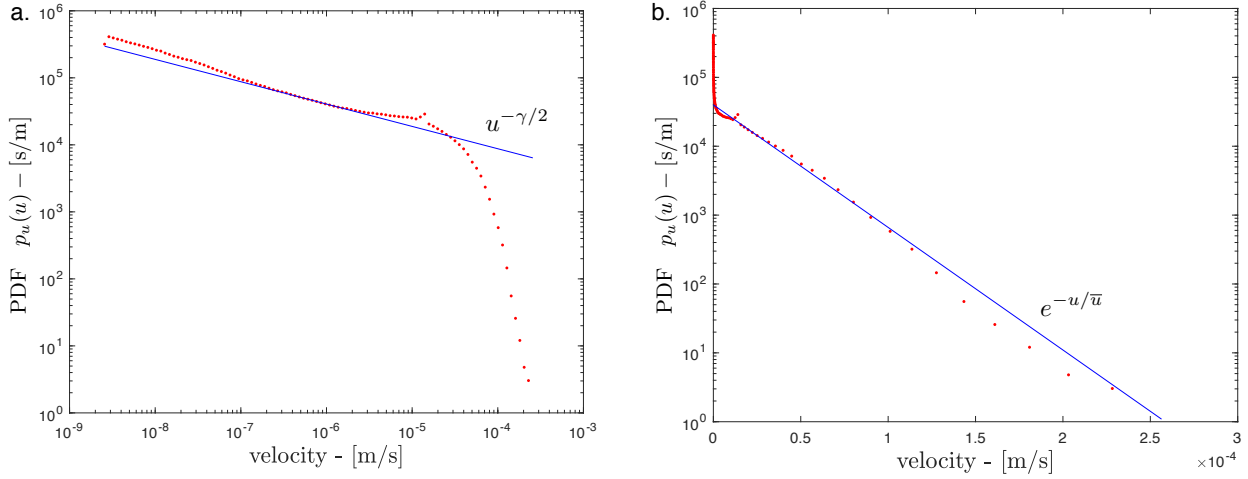$$\mathrm{PDF}_u(u) \sim u^{-\gamma/2}. \tag{5.6}$$

Figure 5.5: PDF of velocities in Stokes flow field. *a*. Logarithmic plot shows the power-law scaling of low velocities values where the exponent is controlled by γ given by the distribution of pore throat size (see Fig. 5.4 *b*.); *b*. Semi-logarithmic plot emphasises the exponential cut-off followed by high velocities values.

where γ is the characteristic exponent of the pore throat size distribution. A detailed analysis of our numerical computation shows that the low velocity PDF is well described by the previous expression, as highlighted by the double logarithmic plot shown in Fig. 5.2.1 *a* with an exponential cut-off, highlighted by the semi-logarithmic plot of Fig. 5.2.1 *b*.

5.2.2 Numerical simulation of transport

Solute transport is simulated using the advection-dispersion equation where the conservation of mass controls the spatio-temporal evolution of a solute concentration $c(x,t)$ in a flow field $\vec{v}$ (which is the Darcy solution $\vec{q}$ or the Stokes one $\vec{u}$, depending on the considered case):

$$\frac{\partial c}{\partial x} = -\nabla \cdot \vec{J} = -\vec{v} \cdot \nabla c + D \nabla^2 c, \tag{5.7}$$

where $\vec{J}$ represents the local mass flux composed by the advective term $\vec{v} c$ ($\vec{v}$ representing the local velocity solution of Darcy or Stokes equations depending on the considered scenario) and the Fickian term $D\nabla c$ (D representing the solute effective dispersion or diffusion coefficient). The initial condition is a sharp front with $c_0 = 1$ initial condition, no-flux B.C at the top and bottom of the domain and around the grains for the pore scale simulation. The solver uses a backward Euler scheme and time stepping is optimized by the solver. In the Darcy field the time for the flow to fill one pore volume is defined as $\tau_{pv} = L/\bar{q} = 1.5\,10^5$ s and the simulation runs for $110\,\tau_{pv}$. Similarly for the pore scale simulation (Stokes flow) $\tau_{pv} = l/\bar{u} = 435$ s and the simulation runs for $60\,\tau_{pv}$. Dispersion/diffusion coefficients are set to be $D^* = 3\,10^{-4}$ mm^2/s for the larger scale and
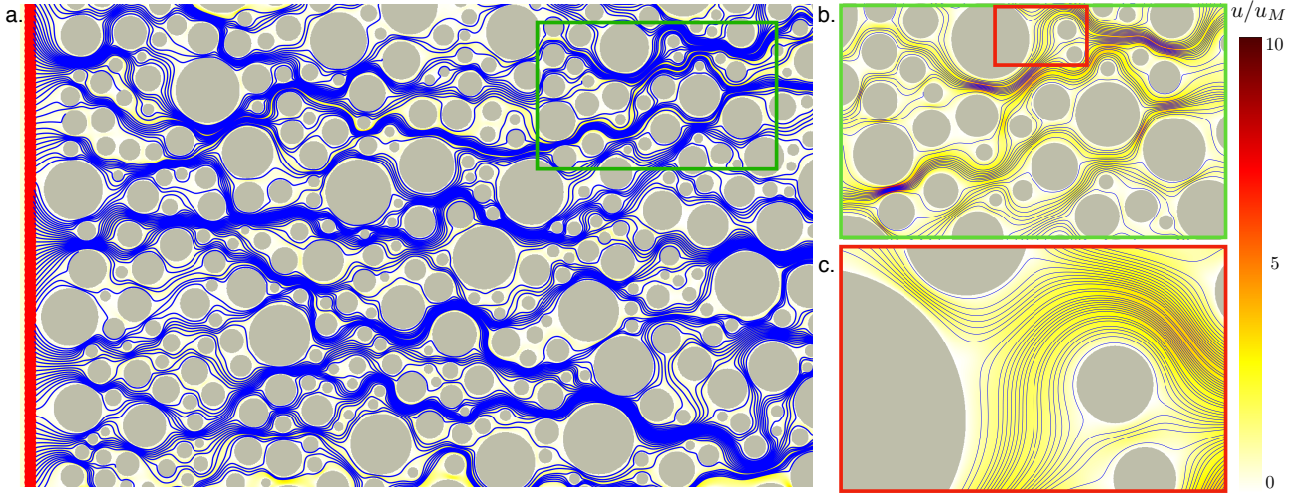
Figure 5.6: Particle tracking simulation results. *a*. Large view of the two-dimensional Stokes solution velocity field magnitude, colormap from light to dark for increasing values, through the considered porous system superposed to 100 trajectories (blue solid lines), whose initial position is represented by a red dot placed on the left hand side of the system. *b*. and *c*. closer views of the same set of trajectories.

$D = 1.2\,10^{-5}$ mm^2/s (matching the value of the tracer used in the experiment discussed in Ch.4) for the pore scale simulation.

5.2.3 Particle tracking

We study transport by the computed velocity fields by tracking the displacement of fluid particles along streamlines (no diffusion, just advection). The fluid trajectories are computed using a fourth-order Runge-Kutta time stepping scheme. Within this framework, the velocity of each transported particle $\boldsymbol{u}(\boldsymbol{x})$ located at $\boldsymbol{x}$ is evaluated by locally interpolating the Eulerian velocity field over a local grid of 10×10 pixels centered around the particle location with a bicubic polynomial. The fourth-order Runge-Kutta time stepping scheme is implemented using the *Matlab* function ode45, which is a powerful tool to solve non-stiff ordinary differential equations (ODE). We use ode45 to integrate the particle p trajectory (x_p, y_p, t_p) which is solution of two ODE at the same time:

$$dx_p(\boldsymbol{x}) = \int_0^{dt} v_x(\boldsymbol{x})\, dt, \quad dy_p(\boldsymbol{x}) = \int_0^{dt} v_y(\boldsymbol{x})\, dt, \tag{5.8}$$

where the $x-$ and $y-$ velocity components and its modulus $v = \sqrt{v_x^2 + v_y^2}$ (v is the Darcy flow field or the Stokes flow field, depending on the case under consideration) are evaluated at the position $\boldsymbol{x} = (x, y)$ of the particle p, as discussed above. In order to get a number N_p of trajectories of equal longitudinal length, in other words every particle moves from the medium inlet to the medium outlet, this calculation will result in trajectories of different size (different number of points), since
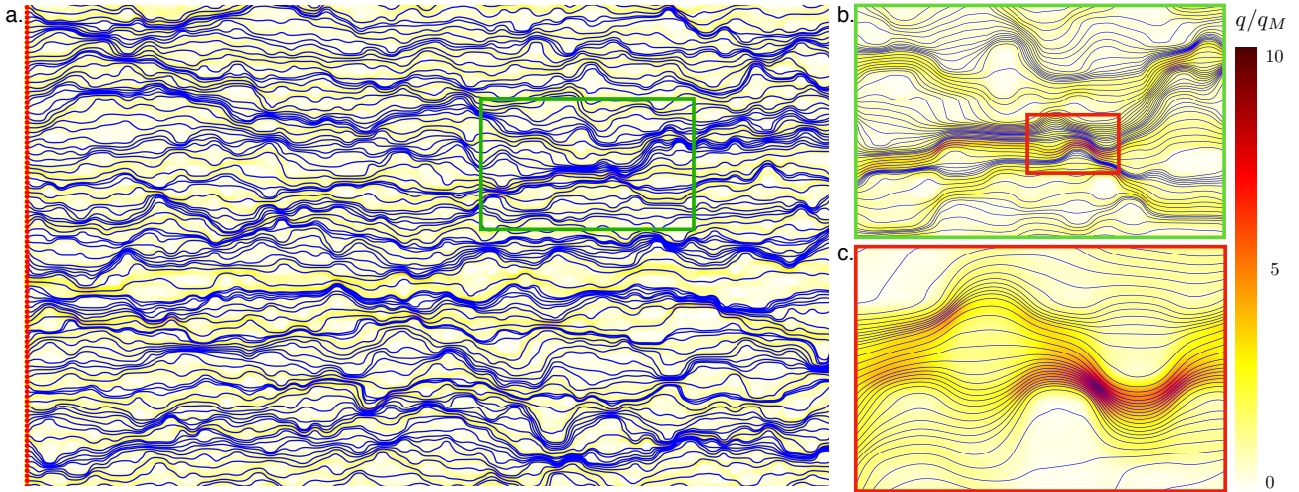
Figure 5.7: Particle tracking simulation results. *a*. Large view of the Darcy's solution two-dimensional velocity field magnitude, colormap from light to dark for increasing values, through the considered porous system superposed to 100 trajectories (blue solid lines), whose initial position is represented by a red dot placed on the left hand side of the system. *b*. and *c*. closer views of the same set of trajectories.

in every location where the flow is stagnant (among tight grains or within a low permeability zone) the time needed to move along is much longer than in faster zones. To avoid this problem and to obtain a similar number of points per trajectory, while a trajectory get integrated by the Matlab function *ode45* we sample the solution over constant spatial steps of size *ds* along the trajectory itself (along the curvilinear coordinate), instead of at constant temporal increments *dt*. Therefore, instead of integrating each step between t and $t + dt$, we integrate the motion of each fluid element p over variable time increments, between t and $t + dt_p(\boldsymbol{x})$, where $dt_p(\boldsymbol{x}) = \frac{ds}{v(\boldsymbol{x})}$ and

$$dx_p(\boldsymbol{x}) = \int_0^{dt_p(\boldsymbol{x})} v_x(\boldsymbol{x})\, dt, \quad dy_p(\boldsymbol{x}) = \int_0^{dt_p(\boldsymbol{x})} v_y(\boldsymbol{x})\, dt. \tag{5.9}$$

In Fig. 5.6 are shown 100 trajectories integrated over the velocity field Stokes solution within the resolved pores and in Fig. 5.7 are shown 100 trajectories integrated over the Darcy's flow solution.

5.3 Results and discussion

5.3.1 Darcy scale

Concentration and concentration gradient fields

We analyze the temporal evolution of a concentration field as it is transported by the computed Darcy velocity field. For the analysis of our transport simulations, we define two time scales that

we will use to normalize time. The first is the characteristic time to travel over one correlation length $\lambda = 0.02$ m of the permeability field $\tau_a = \lambda/\bar{q}$, and the second one is the time required by the invading solute front to move across the porous system up to the position L_x where the BTC will be measured, $\tau_{pv} = L_x/\bar{q}$.
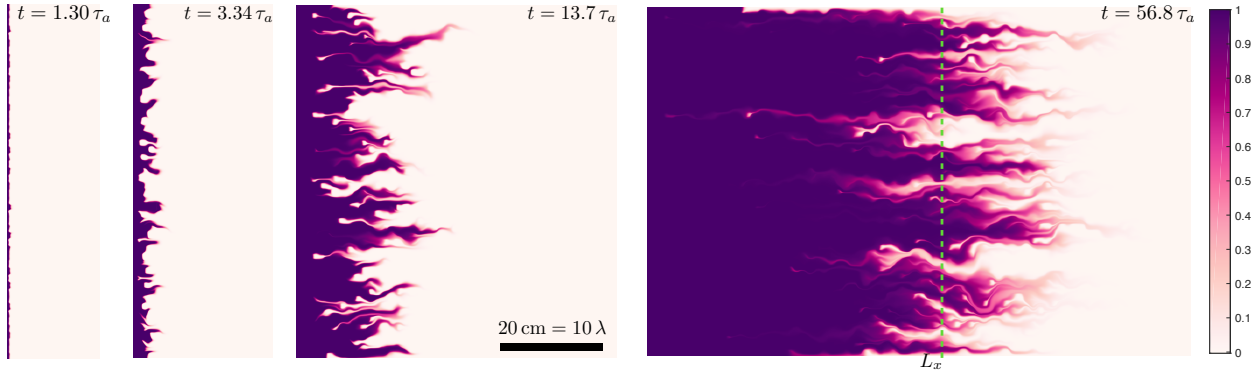

Figure 5.8: Normalized concentration field c/c_0 of invading front in Darcy flow field with average velocity $\bar{q} = 10^{-5}$ m/s and heterogeneous permeability field of correlation length $\lambda = 10^{-2}$ m, Pe = 370. Snapshots at time: $t = 1.30, 3.34, 13.7$ and $56.8\,\tau_a$; the vertical dashed line denotes the position L_x where BTC has been computed.

Snapshots of the computed tracer concentration field are shown in Fig. 5.8 $a - d$ at four time steps $t = 1.30, 3.34, 13.7$ and $56.8\,\tau_a$. As the concentration field travels downstream it experiences heterogeneity of the flow field and we observe the originally transverse front to undergo deformation into an elongated structure, see Fig. 5.8, due to the spatial contrast of local fluid velocities. In this scenario, such fronts can be described as an ensemble of strips aligned along the flow direction, each strip being subject to competitive mechanisms of diffusion (along the strip transverse direction) and local stretching (along the local flow direction). In such context, these strips are typically called lamella and the front undergoes the so-called lamella-like topology described by [82, 72, 22].

Figure 5.9 shows the magnitude of the gradient of the concentration field at times $t = 1.30, 3.34, 13.7$ and $56.8\,\tau_a$:

$$|\nabla c/c_0| = \sqrt{\left(\frac{\partial c}{\partial x}\right)^2 + \left(\frac{\partial c}{\partial y}\right)^2}. \tag{5.10}$$

Initially, the gradient magnitude looks-like a vertical strip: as time advances, it gets displaced with the average fluid velocity and it elongates about it in the discussed lamellar structure. The zoomed-in view shown in Fig. 5.9 for time $13.7\,\tau_a$ highlight the role played by low permeability zones: there the front substantially slows down compared to the surrounding faster flow zones. This velocity

contrast stretches the front keeping the gradient magnitude steep (darker color) against the action of dispersion that tend to smooth-down the concentration values and, thus, the gradient.
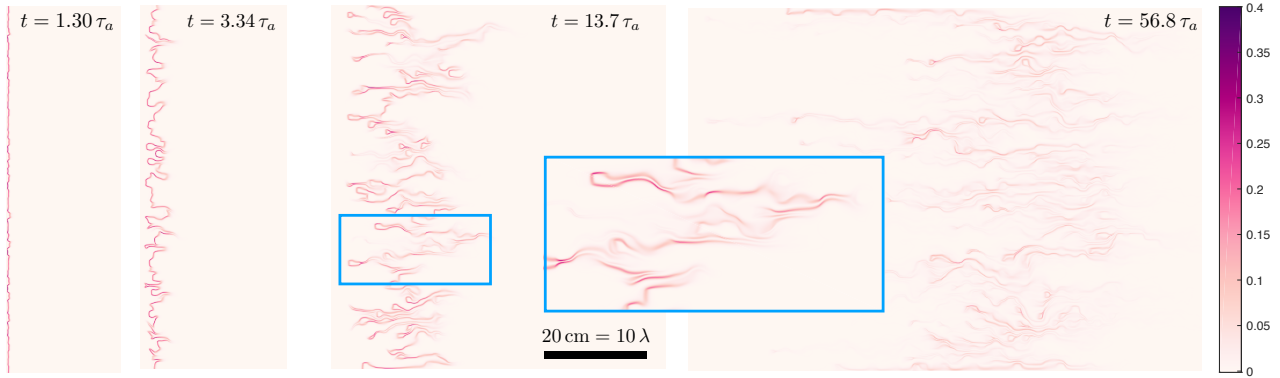

Figure 5.9: Concentration gradient field $\nabla c/c_0$ of invading front in Darcy flow field with average velocity $\bar{q} = 10^{-5}$ m/s and heterogeneous permeability field of correlation length $\lambda = 10^{-2}$ m, Pe = 370. Snapshots at time: $t = 1.30, 3.34, 13.7$ and $56.8\,\tau_a$.

To understand the role played by fluid stretching we follow the recent study of Le Borgne et al. [63] and we quantify the front deformation in terms of the statistics of Lagrangian particles simply advected by the computed velocity field.

Local stretching and elongation

Local stretching will be quantified in terms of the elongation experienced by fluid elements located along a strip initially oriented in the main flow transverse direction (the blue line in Fig. 5.10). As time passes, each fluid element composing that strip is moving with the flow, we neglect diffusion here, following the particle tracking scheme discussed above. While moving with different velocities, the heterogeneous flow field deforms that strip, as shown in Fig. 5.10 for three times $t = 3, 23, 43\,\tau_a$ from dark to light color, superposed to the velocity field magnitude.

Zones of low velocity slow down significantly the front while increasing its length. Due to flow heterogeneity the front does not deform homogeneously: at different position, along the front, fluid elements get separated by different amount of space. Moving along the front, we model it as composed by a sequence of fluid elements labeled $k = 1 \ldots, N_p$, from bottom to top in Fig. 5.10. Initially these fluid elements are equally spaced with distance ds_0 among each neighboring couple k and $k - 1$. After a time t, the distance among particles becomes:

$$ds_k = \sqrt{(x_k - x_{k-1})^2 + (y_k - y_{k-1})^2}, \tag{5.11}$$
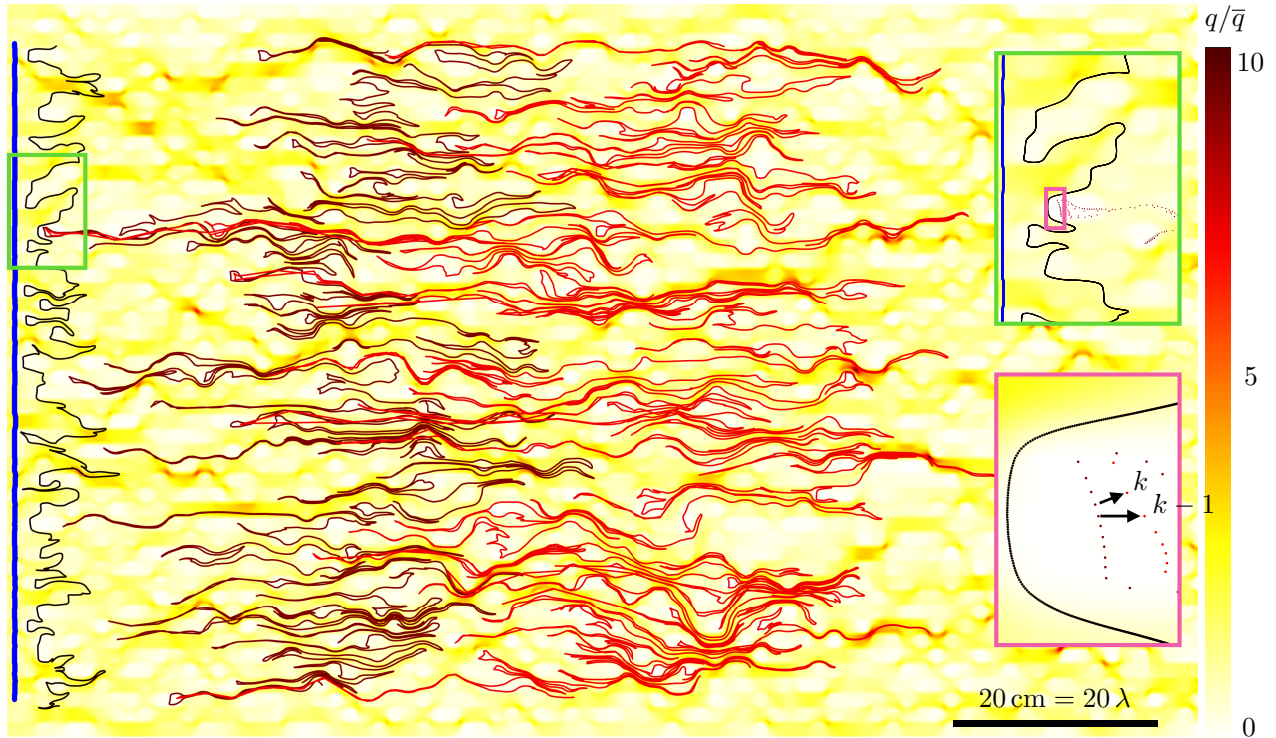
Figure 5.10: Deformation of a strip, initially oriented transverse to the flow direction (vertical blue line), superimposed on the heterogeneous Darcy velocity field magnitude $q/\bar{q}$. The deformed strip is shown at three times $t = 3, 23, 43\,\tau_a$ from dark to light color. While the strip is stretched and elongated by the contrast of velocities it remains a continuous line. Green and red rectangles shows zoom-in views of a portion of the strip up to the individual fluid elements labeled k.

and the overall front length would be:

$$\Sigma(t) = \sum_{k=1}^{N_p} ds_k.$$

(5.12)

As shown in the two zoomed-in view of the deforming front location, inset of Fig. 5.10, the fluid particles are moving through the continuous Darcy velocity field accelerating and slowing down based on the local velocity magnitude, but never encountering impermeable boundaries (the permeability field is defined positive in this context). This acceleration/deceleration is reflected in the local fluid particles separation and approach controlling the stretching/compression of the front. In particular, the pink-framed inset of Fig. 5.10 shown the separation between two neighboring particles, k and $k-1$ at two successive time steps of the particle tracking simulation (from the dark to light color as time increases).

Figure 5.11: Concentration field c/c_0 of the invading front, gray discs stand for solid and impermeable grains, Péclet number $Pe = 250$. Snapshots at time: $t = 2.38, 7.13, 16.6$ and $49.9\,\tau_a$. The vertical dashed line denotes the position L_x where BTC is computed.
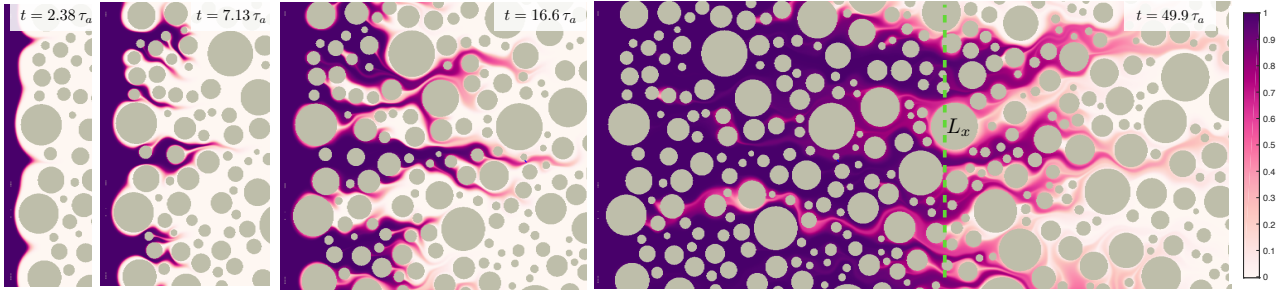
5.3.2 Pore scale

Concentration and concentration gradient fields

We analyze the concentration field of a tracer displaced within the considered fully resolved porous medium geometry: an example of the measured fields at time $t = 2.38, 7.13, 16.6$ and $49.9\,\tau_a$ is given in Fig. 5.11. The vertical dashed line represents the location where the BTC is measured. As the concentration front enters the porous medium, it get distorted into a lamellar topology similar to what is observed at Darcy scale: in each pore a lamella is subjected to the local pore velocity and it gets elongated by stretching along the local flow direction, while diffusion smooth-out the concentration value increasing the lamella extend in the transverse direction. While the lamella width increases the diffusing concentration eventually encounters the impermeable wall of a grain (representing physical confinement), where the mass flux is null. In other words, mass accumulates at the grains walls and concentration increases.
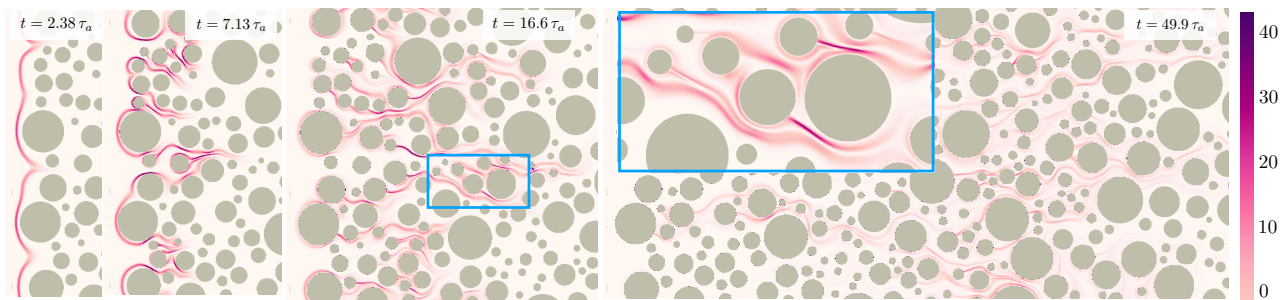
Figure 5.12: Concentration gradient $\nabla c/c_0$ of the invading front, Pe = 250. Snapshots at time: $t = 2.38, 7.13, 16.6$ and $49.9\,\tau_a$.

Figure 5.12 show four snapshot of the concentration gradient magnitude, as defined also for the Darcy scale scenario in Eq. (5.10), at times $t = 2.38, 7.13, 16.6$ and $49.9\,\tau_a$. At early time, the front is basically vertically aligned and the gradient is quite homogeneous along the vertical direction while

it varies due to diffusion) along the longitudinal direction. As time passes, the front deforms and undergoes stretching due to fluid velocity heterogeneity among the grains. The gradient magnitude value becomes variable along the front location since at different locations different stretching are exerted.

Local stretching and elongation

We investigate the fluid stretching induced by the flow heterogeneity within the porous structure shown in Fig. 5.13 following the same procedure and computing the same diagnostic quantities as for the Darcy's flow scenario considered above. Therefore, local stretching will be quantified in terms of the elongation experienced by fluid elements located along a strip initially oriented in the main flow transverse direction (the blue line in Fig. 5.13). As time passes, each fluid element composing that strip is moving with the flow (in order to study the only effect of front deformation due to fluid stretching we neglect diffusion here) following the particle tracking scheme discussed above. While moving with different velocities, the heterogeneous flow field deforms that initial strip, as shown in Fig. 5.10 for three times $t = 6, 22, 39\,\tau_a$ from dark to light color, superposed to the velocity field magnitude (from light to dark color for increasing velocity values).
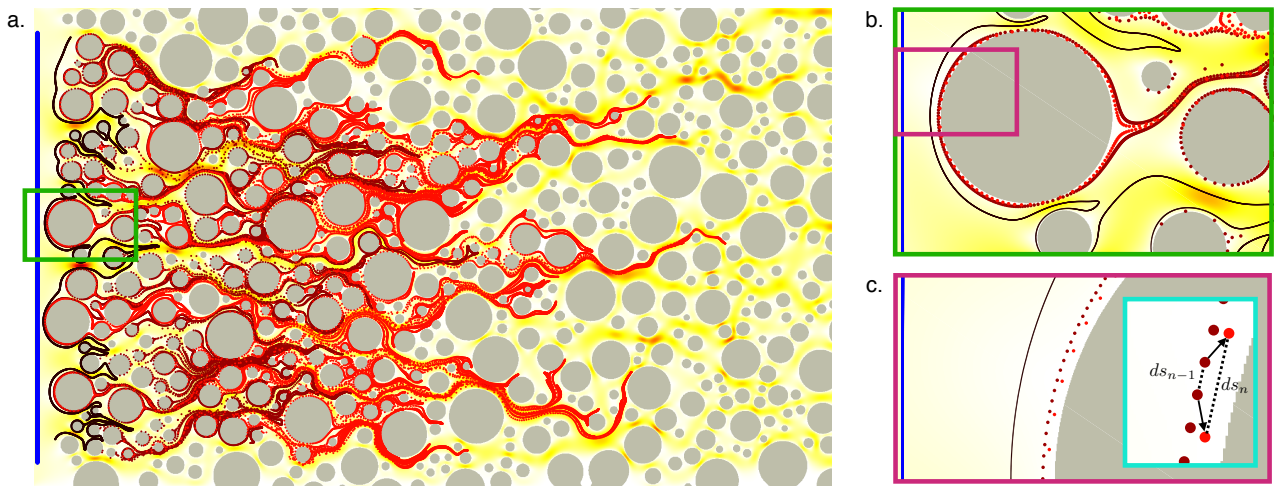
Figure 5.13: *a.* Deformation of a strip, initially oriented transverse to the flow direction (vertical blue line), superimposed on the heterogeneous Stokes velocity field magnitude. The deformed strip is shown at three times $t = 6, 22, 39\,\tau_a$ from dark to light color. As the strip is advected in the porous medium it get pin behind the grains; *b.* Zoom-in view of the strip as it encircle a grain, it forms an anchor point persistent throughout the strip elongation in the domain; *c.* Zoom-in view showing the individual fluid particles at two times ($n-1$ and n) as they are advected towards the grains.

As shown in the three zoomed-in view of the deforming front location, insets of Fig. 5.13, the fluid particles are moving through the continuous pore scale velocity field accelerating and slowing

down based on the local velocity magnitude, getting around the impermeable boundaries of the solid grains wall. This acceleration/deceleration is reflected in the local fluid particles separation and approach controlling the stretching/compression of the front. In particular, the cyan-framed inset of Fig. 5.13 shown the separation between two neighboring particles, at two successive time steps n and $n + 1$ when we sampled the particle tracking simulation (from the dark to light color as time increases). As the front passes by a grain the front surrounds it with a fluid envelop that get elongated homogeneously, as shown by the relatively constant separation of dots visible behind each grain (see inset of Fig. 5.13). We understand that acknowledging the fact that close and around the grains, fluid velocity is very small and approaches zero, due to no-slip boundary conditions, while further away the fluid elements can move faster. Thus, in first approximation, all fluid elements left behind a grain move homogeneously and, thus, get separated from each other at the same rate.

5.3.3 On the role of confinement on mixing

We considered two simplified case studies for mixing within heterogeneous porous systems that differ from the observation scale: one resolves the detailed structure of the pore space, the other captures the larger scale without resolving the solid grains arrangements. The first case heterogeneity is dictated and controlled by the pore throats size distribution, the length scale through which the fluid is locally forced to pass while governed by viscous forces. For the second case, the detailed medium structure is replaced with a continuous permeability field whose local value represents the ability of the medium to locally transmit fluid for a given pressure drop. Both case studies have a similar heterogeneity in terms of the resulting velocity field that ranges across four orders of magnitude. Moreover, to make the two cases comparable we considered a spatial correlation length λ such that the considered domains longitudinal size L is $L/\lambda \sim 100$.

In both scenarios, the longitudinal concentration profile P is well described by the solution of one dimensional advection-dispersion equation:

$$P(x,t) = \frac{1}{2} \left[1 - \text{erf}\left(\frac{x - x_0}{\sqrt{4\,D^\star\,t}} \right) \right]. \tag{5.13}$$

where $x_0 = \bar{q}\,t$ or $x_0 = \bar{u}\,y$ is the average front position for the Darcy and pore scale case, respectively and $D^\star$ begin the effective dispersion coefficient which is a measure of the solute spreading about its own front. Figures 5.14 a. and 5.15 a. show as colored solid lines the observed profiles superposed to the fitted model Eq. (5.13) (black solid lines), where $D^\star$ is the only fitting parameter that minimizes the sum of the square differences between the numerical solution and the model itself. The averaged

value of the fitted $D^\star$ over all times is 0.11 mm^2 /s for the Darcy scale and $D^\star = 4.2\,10^{-3}$ mm^2/s for the pore scale simulation. Note that the latter value is close to the one obtained in the transport laboratory experiment ($D^\star = 3\,10^{-3}$ mm^2/s in Ch.4) performed within the same geometry printed into a microfluidic device.

An important macroscopic measure of solute transport is the Break-Through Curve (BTC) which is a time-series of c/c_0, the transversely averaged concentration, normalized by the injected one c_0, measured at the downstream position L_x (see vertical red line in Fig. 5.8). Here we consider the complementary BTC, or $1 - c/c_0$ which is shown in Fig. 5.14 *b* for the Darcy scale and Fig. 5.15 *c* for the pore scale, respectively. In both cases, the complementary BTC is constant, and equal to unity, until time reaches τ_{pv}, which means that the average front breakthrough at L_x; then, it decays. This temporal behavior can be modeled with the previously introduced advection dispersion framework dimensional advection-dispersion equation, evaluated at $x = L_x$:

$$P(x = L_x, t)/c_0 = \frac{1}{2}\left[1 - \operatorname{erf}\left(\frac{L_x - \bar{q}\,t}{\sqrt{4\,D^\star\,t}}\right)\right], \tag{5.14}$$

where the dispersion coefficient $D^\star$ is the one fitted on the concentration field longitudinal projections. For normalized times $t/\tau_{pv} > 1$ it start to decay exponentially with characteristic time scale

Figure 5.14: Results for the Darcy scale. Transport and mixing measures of a concentration field displaced in a Darcy flow field. *a*. Longitudinal projection of concentration field (Fig5.8 *a.-d.*), for time t = 3, 13, 27 and 43 τ_a, time increases from light to dark colours, black solid lines are Eq. 4.6 with $D^\star$ as fitting parameter, value obtained over all time steps is $D^\star = 0.11$ mm^2/s; *b*. complementary BTC recorded in the middle of the domain, time is normalized by the advective time over a pore volume, black solid line is prediction of Eq. (5.14) with $D^\star$ fitted on the longitudinal projection of concentration field; *c*. Segregation intensity, time is normalized by advective time over the permeability field correlation length λ.

$D^*/\bar{q}^2$. We note that for later times, when the BTC is smaller than 10^{-2}, the BTC deviates from the exponential decay exhibiting the so-called tailing, a signature of the medium strong heterogeneity [65]. From the direct analysis of the computed concentration field it is possible to get information about the mixing process and its temporal dynamics.

We chose, as metric for mixing in confined conditions, the intensity of segregation as defined by [112]:

$$I(t) = \frac{\overline{c(x,t)^2} - \overline{c(x,t)}^2}{\overline{c(x,t)}\,(1 - \overline{c(x,t)})},\tag{5.15}$$

which quantifies the degree of segregation between two components A and B, here our tracer of concentration c and the background/displaced solution of concentration $1-c$, the average concentration of A is $\overline{c(x,t)}$ and of B is $(1 - \overline{c(x,t)})$. $I(t)$ varies from 1 when the segregation is total ($c(x,t)$ is either 1 or 0) to 0 when the system it is homogeneous. The temporal evolution of $I(t)$ is shown in Fig5.14 c for the Darcy scale case and in Fig. 5.15 b for the pore scale scenario. Here we observe a first substantial difference between the two case studies: while the segregation index for the Darcy scale decreases from its initial value down to about 0.87 after $60\,\tau_a$, for the pore scale scenario it decays more going from its initial value, down to 0.65. This implies that the level of segregation measured at the Darcy scale is more important that the one at the pore scale. In other words, the
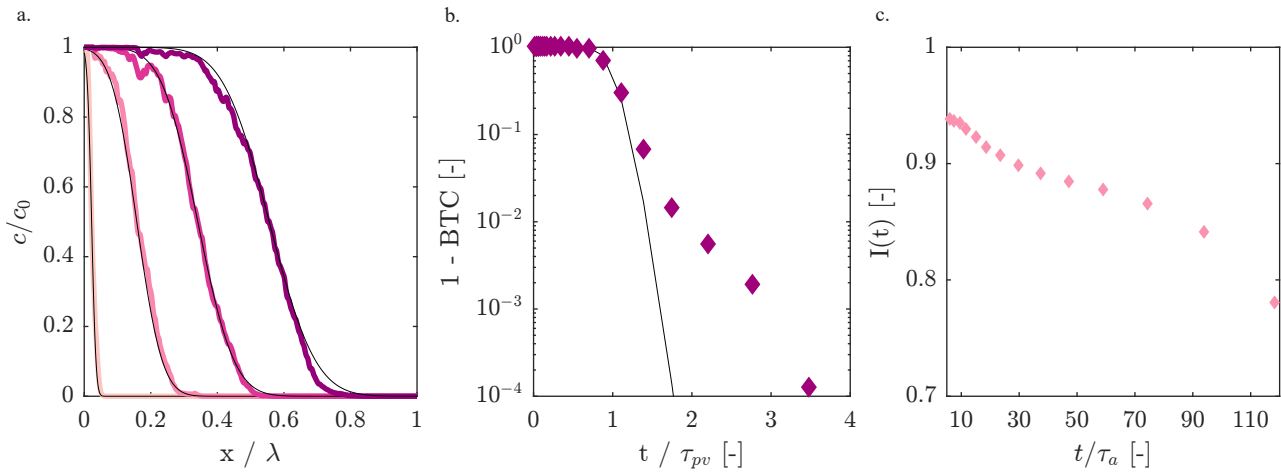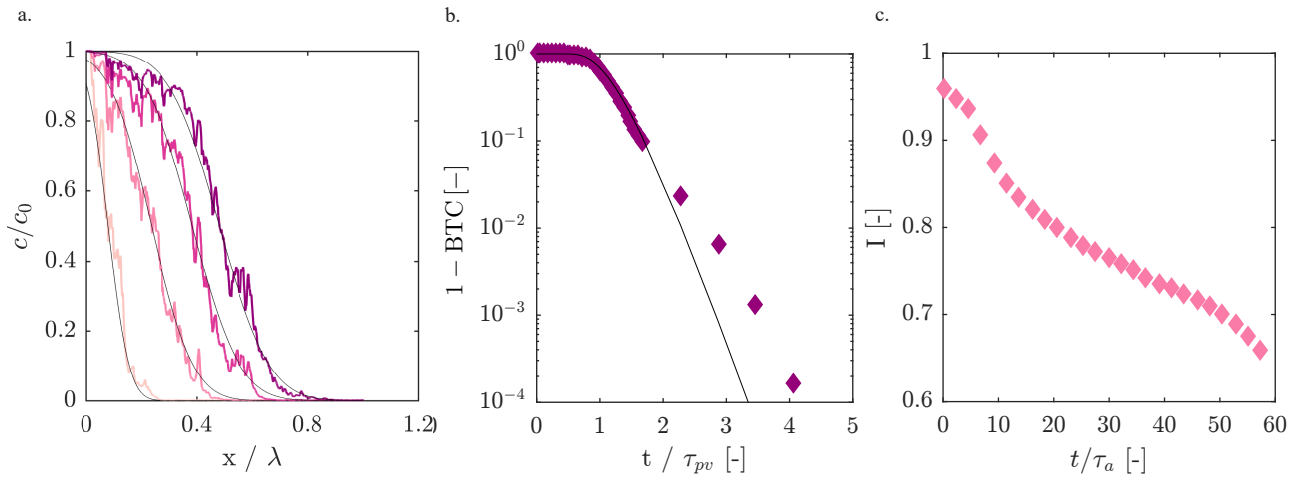

Figure 5.15: Results for the pore scale. Transport and mixing measures of a concentration field displaced in a porous medium structure. *a*. Longitudinal projection of concentration field (Fig5.8 *a.-d.*), for time t = 19, 21 32 and 41 τ_a, time increases from light to dark colours, black solid lines are prediction from advection-dispersion equation 5.7 with $D^\star$ as fitting parameter, value obtained over all time steps is $D^\star = 4.2\,10^{-3}$ mm^2/s; *b*. Segregation intensity, time is normalized by advective time over the average pore throat size λ; *c*. Complementary BTC recorded in the middle of the domain, time is normalized by the advective time over a pore volume, black solid line is prediction of Eq. (5.14) with $D^\star$ fitted on the longitudinal projection of concentration field.

pore scale get mixed and it segregation reduced faster that in the non-confined and continuous case. This is consistent with the observation, described in Ch.2, that diffusion within confined boundaries happens faster and mixes more efficiently than in an unconfined and continuous medium.

Figure 5.16: Darcy scale; *a*. PDF of the concentration field shown in Fig.5.9 with time increasing from light to dark colours, blue solid line indicates the c^{-1} scaling for low concentration values; *b*. PDF of the corresponding concentration gradient field shown in Fig. 5.8, blue solid line indicates the g_c^{-1} scaling for low values as predicted by [22]; In both *a*. and *b*. the distributions are spread out in the vertical direction for better readability.

To further analyze the mixing state of the displacing solutes, we consider their concentration PDF: a normalized histogram of the spatial occurrence of the concentration value. Unlike other metrics, such as longitudinal projection, spreading length, or BTC, the PDF gives credit to the entire range of concentrations values, similarly to the segregation index. We compute the PDF of invading scalar concentration that are shown in Fig. 5.16 *a* for the Darcy scale and in Fig. 5.17 *a* for the pore scale. The time at which the PDF have been computed are the same as the one where the corresponding fields have been shown above.

For the Darcy scale, at all times the concentration PDF seems to be the same, scaling as $1/c$ for low concentration value, reaching a minimum value at about $c = 1/2$ and increasing again for larger concentrations. Following the lamellar description of mixing proposed by [82, 72, 22], the PDF of the concentration field can be computed as the superposition of the PDF of all individual lamellae. Considering an invading front (and not a pulse as in [82, 72, 22]), the stretching mechanisms as the effect of modifying the space over which the normalized concentration c/c_0 varies between 0 to 1, but it does not affect the minimum or maximum values in each lamella. Therefore, the

superposition of several lamellae that experience different stretching results in the same PDF as the one of an individual lamella whose concentration ranges between 0 and 1 following an error-function like shape (solution of diffusion equation for a front in unconfined conditions, as discussed in chapter two).
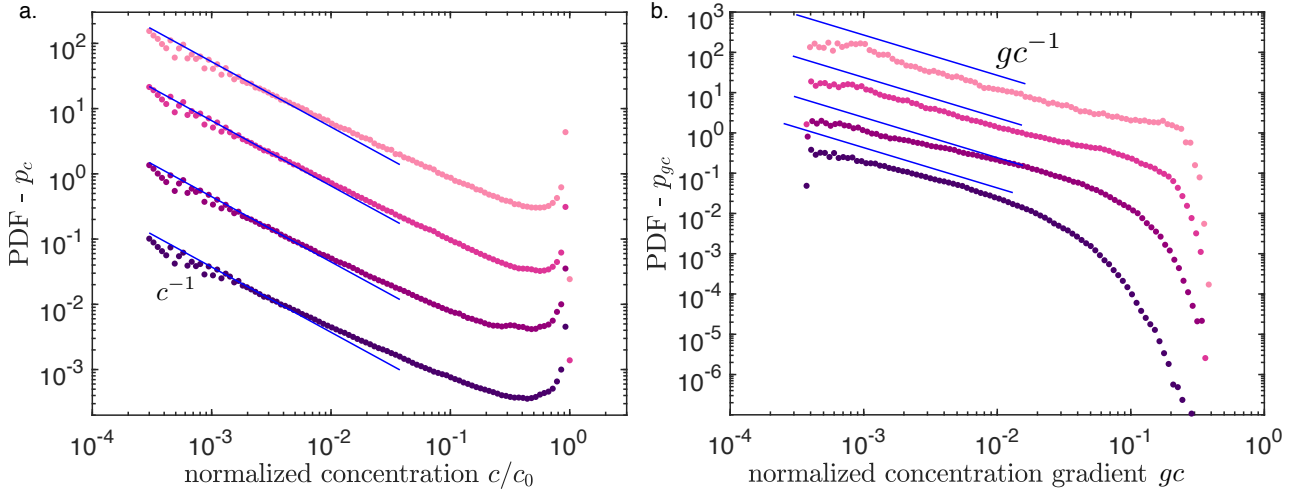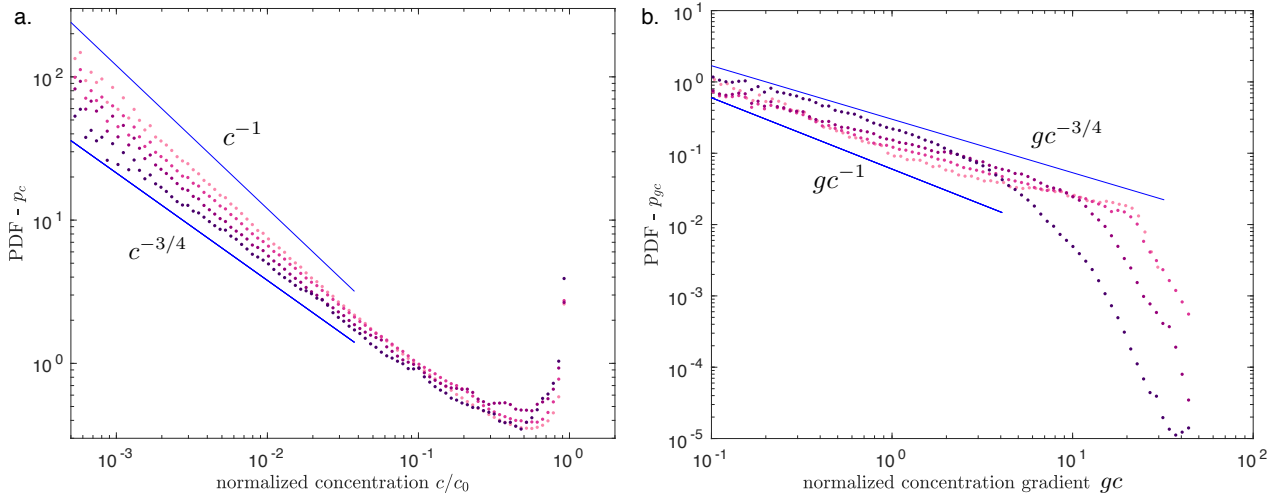

Figure 5.17: Pore scale; *a.* PDF of the concentration field shown in Fig.5.11 with time increasing from light to dark colours, we note the transition of low concentration values scaling from c^{-1} at early time to $c^{-3/4}$ at later time; *b.* PDF of the corresponding concentration gradient field shown in Fig. 5.12, transition of low concentration values scaling from g_c^{-1} at early time to $g_c^{-3/4}$ at later time which diverge from the pore scale observations.

For the pore scale, instead, we observe a clear dynamics. The early times, about $2\,\tau_a$, concentration PDF has the same behavior discussed for the Darcy scale: it scales as $1/c$ for low concentrations and it increases for values larger than $c = 1/2$. However, as time passes the scaling of the low concentration values decreases approaching the scaling $c^{-3/4}$ observed at later times, above $40\,\tau_a$. This means that there is less and less occurrence of low concentration values, and there is more and more occurrence of intermediate values, as reflected in the slight increase of the PDF for value about $c = 1/2$. We interpret that as another signature of the presence of no-flux boundary conditions at the grains wall that define the system confinement. Note that we discussed the same observation in the previous chapter, as observed with our microfluidics experiment.

We also quantified the concentration gradient magnitude, as shown in Figs. 5.8 and 5.12. We denote with g_c the concentration gradient magnitude value: its PDF is shown in Figs. 5.16 *b* and 5.17 *b* for the Darcy and pore scale scenarios, respectively. The Darcy scale g_c PDF scales for low values of g_c as g_c^{-1}, while at higher values we observe an exponential cut-off whose value decreases with time.

We interpret that as the effect of local fluid stretching on individual lamellae, as observed by [63] for a conservative pulse. The pore scale g_c PDF for low values of g_c scales as g_c^{-1} for early times and it slows down the scaling towards $g_c^{-3/4}$ for larger times. The higher values PDF displays an exponential cut-off whose value decreases with time, as for the Darcy's case.

The novel lamellar model presented by [63] assumes that an invading front can be described as the superposition of several lamellae that undergo i) stretching by the flow filed along the local flow direction and ii) diffusion along the transverse one. In this framework, the statistical combination of all lamellae evolves according to different regimes. At early times, all lamellae are independent since diffusion has not had enough time to get them into contact: thus, the overall concentration PDF is the simple average of the individual lamellae PDF that is assumed to be the one of a one-dimensional diffusive pulse (or front, depending on the case under consideration) in a unconfined domain. If a pulse is considered, or the gradient of a front is under investigation, the local fluid stretching is impacting the maximum value of the lamella concentration. This can be systematically taken into account through the Ranz transform, as introduced and discussed in chapter two, that normalizes the time of each lamella with respect to the characteristic diffusive time across the lamella width the undergoes stretching and compression. As observed and modeled by [63], this combined mechanisms have the effect to introduce a exponential cut-off to the concentration PDF of a pulse, or of a front gradient; the dynamics of the cut-off value begin controlled by the stretching statistics.

The fluid stretching for both the considered scenarios are, here, defined in terms of local front elongation, relative to the initial separation ds_0, as $\rho = ds/ds_0$. We compute, at every time, the PDF of the local elongation $p_\rho(\rho)$: in Fig. 5.18 a it is shown as dots $p_\rho(\rho)$ at times $t = 3, 23, 43\,\tau_a$ (the same times for which the displacing fluid elements line is shown in Fig. 5.10) with different colors for different times (time increases from dark to light colors). This PDF is well described by the power-law distribution, shown as solid lines:

$$p_\rho(\rho) = [\rho + \overline{\rho}(t)]^{1-2\beta}, \tag{5.16}$$

where $\beta = 1.8$ is the same parameter characterizing the grain radii (size) distribution shown in Fig. 5.4 and $\overline{\rho}$ is the average elongation. Note that the model superposed to the simulated data is not a fit. We understand this supposing that, as observed in Fig. 5.18, the fluid particles are moving with very similar and slow velocity when they approach a grain. Behind each grain the moving par-

ticles experience the strong and homogeneous elongation that characterizes the tail of the observed p_ρ. Since in the middle of a pore the fluid velocity is close to the average velocity $\overline{u}$ and close to a grain the velocity approaches zero, the stretching intensity behind a grain is set by the grain size R itself: along that distance the fluid particles get separated because on the one hand they are pinned, on the other hand they get pulled at average velocity $\overline{u}$. Thus, the grain size distribution controls the local fluid stretching as quantified by the local fluid elements relative elongation ρ.

In Fig. 5.18 b it is shown as dots $p_\rho(\rho)$ at times $t = 6, 22, 39\, \tau_a$ (the same times for which the displacing fluid elements line is shown in Fig. 5.13) with different colors for different times (time increases from dark to light colors). This PDF is well fitted by the log-normal distribution, shown as solid lines:

$$p_\rho(\rho) = \frac{1}{2\rho\,\sigma_\rho\,\sqrt{2\pi}}\, e^{-\frac{(\log[\rho]-\mu_\rho)^2}{2\sigma_\rho^2}}, \tag{5.17}$$

where the two parameters μ_ρ and σ_ρ are fitted to minimize the difference between model Eq. (5.17) and computed PDF $p_\rho(\rho)$.
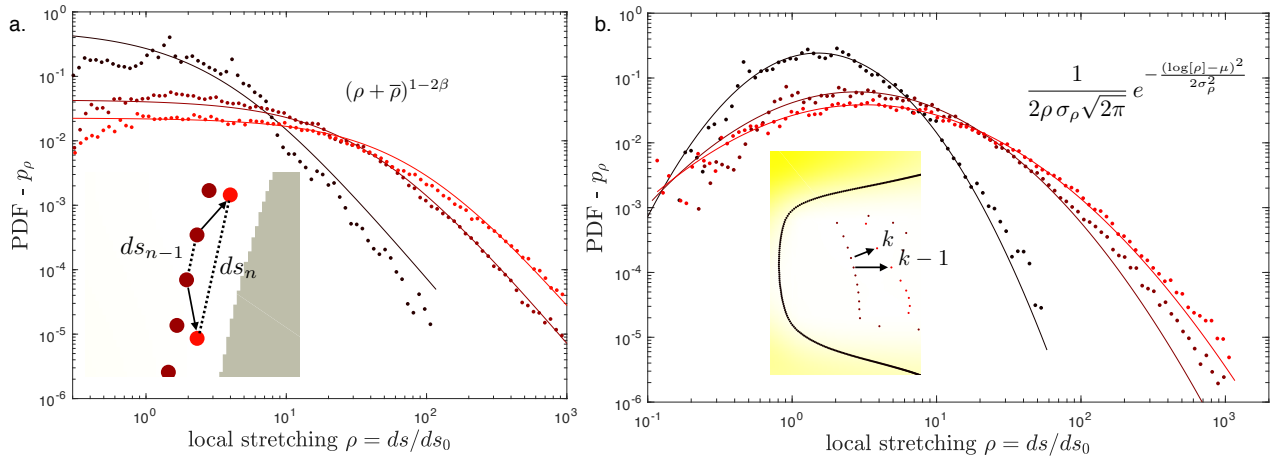
Figure 5.18: PDF of local stretching ρ; *a.* Distributions for pore scale velocity field, shown at times corresponding to Fig. 5.13, inset shows individual fluid particles at two time step $n-1$ and n as they approach a grain surface (gray area) and the local stretching ds, the distribution is described by Eq. 5.16; *b.* Distributions for Darcy scale velocity field, shown at time corresponding to Fig. 5.10, inset shows individual fluid particles as they are advected at two times $k-1$ and k, the distributions are well described by Eq. 5.17.

This observed distribution of the elongation reflects the broad heterogeneity of velocity field which is a consequence of the permeability field, as observed also by [63]. The global stretching is quantified by the average elongation $\overline{\rho}$ which is also identical to the normalized front length $\Sigma(t)/\Sigma(t=0)$:

this is shown in Fig. 5.19, inset a for pore scale and b for the Darcy's one. In both scenarios, the front elongation dynamics scales as the power law:

$$\bar{\rho} = 1 + [t/\tau_c]^\beta, \tag{5.18}$$

where we fit the exponent parameter $\beta = 1.8$ and $\beta = 1.2$ and the characteristic time $\tau_c = 3\,\tau_a$ and $\tau_c = 2.5\,\tau_a$ for the pore scale and Darcy's scale, respectively.
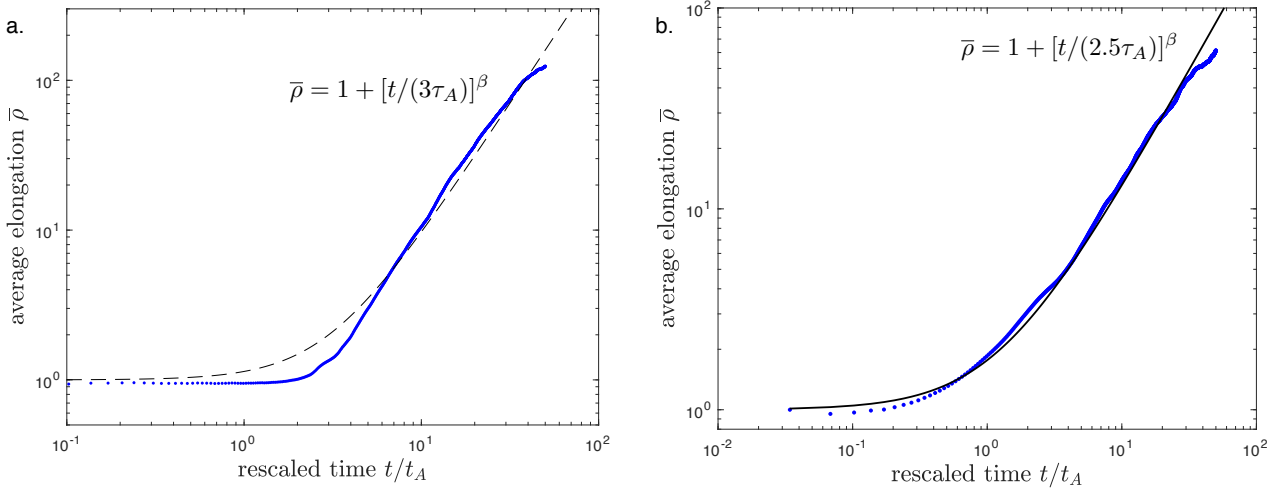
Figure 5.19: Temporal evolution of average elongation at pore a. and Darcy scale b.. Both dynamic are well described by the power law given in Eq. 5.18.

5.4 Conclusion

This chapter presents numerical simulations of flow, transport and particle tracking at both Darcy and pore scale. Darcy scale simulations were performed to be uses as a control for the pore scale analysis. Our large scale (Darcy) results are in agreement with previous studies [25, 72, 22] in term of transport, concentration distribution and fluid stretching, as quantified by solute, transport particle tracking simulation and Lagrangian analysis.

Solute transport by a Stokes flow field was designed to i) validate and support the observations collected with our novel laboratory experiments, as presented in Ch.4, and ii) study concentration gradient fields and their distribution, which is technically very challenging from small scale laboratory observations. Although the porous medium geometry as well as the fluid and solute properties, are matched in simulations and experiments, we acknowledge that two important elements make difficult a direct and exact comparison between data sets collected with experiments and with nu-

merical simulations.

First, the laboratory experiments were conducted in microfluidic channels, whose geometry is two-dimensional but the actual channel is three-dimensional: thus, our observations are 2D projections of the occurring flow and transport processes, while our simulations are strictly two dimensional. Second, in both cases the initial condition is a front, in the simulation it can be made sharp and from the first time step the concentration at the inlet is exactly the maximum concentration c_0, while in the micro-fluid chip inevitably some Taylor-dispersion effect occurs within the inlet area of the chip (even though we payed particular attention to use a re-circulation scheme to minimize this effect), thus, the invading front is not perfectly sharp. Beside these observations, the results obtained from the simulations and experiments clearly indicate that solute transport is affected by the confined condition prevailing inside the pores as quantified by i) a diffusion profile and ii) a stretching kinematics that are fundamentally different in the confined versus continuous description of porous systems.

Chapter 6

Conclusions

This thesis collects the efforts to move a step forward towards a more realistic description of mixing phenomena by confined and heterogeneous media and take into explicit consideration the discrete nature of a porous system composed by impermeable and solid grains. We consider that the displaced concentration field of a dissolved substance through a solid matrix experiences an ensemble of obstacles constraining flow and mass transport by imposing no-flow (i.e no slip) and no-flux boundary conditions. Therefore, we hypothesize that the solid boundary constrain alters both **stretching mechanism** and **diffusion dynamics** affecting the overall concentration field distribution. The thesis focuses on those two main axes: i) diffusion limited mixing and ii) stretching dynamics, under physically confined condition.

Diffusion-limited mixing under confinement

Diffusion is the key mixing mechanism in fluid systems, since it ultimately homogenizes concentrations, also in the presence of stretching and compression by velocity heterogeneity. We computed the analytical solution of the one-dimensional diffusion equation in a confined domain, characterized by the presence of no flux boundaries, separated by a distance λ (which could represent the size of a pore), that prevent the solute concentration from diffusing freely and explore wider areas of space. We show how diffusion is affected by the confined nature of the considered spatial domain and we quantify its impact on mixing.

The general solution of the diffusion equation in a confined domain, expresses the concentration profile of a diffusive tracer as the superposition modes m (functions that do not change shape as the system diffuses) that are periodic and fluctuating in space between the domain boundaries, and temporally decaying exponentially fast, scaling as $\exp(-m^2\pi^2 t)$. As far as the diffusing tracer does

not experience the presence of the impermeable boundaries (e.g. right after the injection of a pulse in the middle of the domain $t < 1/(m^2\pi^2)$) the exponential decay of the modes is not substantially changing their amplitude and a large number of modes must be taken into account to describe the tracer concentration profile, recovering the classical solution for an un-confined case. In such conditions space and time are coupled and the concentration profile can be expressed in terms of the classical dimensionless coordinate for diffusion, $\xi = x/\sqrt{2Dt}$, making the profile self-similar and scale independent, which is reflected in the slow, power law decay of several mixing measures. However, as soon as a single mode m dominates the sum, space and time are decoupled and the exponential decay of the solution defines a characteristic time scale ($1/(m^2\pi^2)$), as reflected by the exponential decay of the mixing measures considered.

Physically, in a confined space the no-flux boundary condition $\nabla c(0,t) = \nabla c(\lambda,t) = 0$ imposes a flat profile at the domain edges leading to an overall steeper gradient and higher mass flux compared to the unconfined case where mass can freely diffuse exploring wide areas of space, slowly dissipating the concentration gradients. Therefore local and global measures of mixing display significantly different dynamics. The resulting exponential time scaling of mixing measures in confined conditions leads to the definition of a new characteristic time scale for diffusion, which depends on the initial condition and it is fixed by the leading mode (e.g. $m = 1$ for a front and $m = 2$ for a pulse), $\lambda^2/(m^2 D \pi^2)$, which is much shorter (one order of magnitude shorter) than the characteristic λ^2/D defined to re-scale the diffusion equation. Our observations show that the homogenization dynamics (mixing) is significantly faster under confinement, i.e. no-flux boundary conditions.

Novel method to measure the diffusion coefficient

Knowing the value of the diffusion coefficient D is crucial to describe the fate of a diffusing substance and all the diffusion-related phenomena, like mixing or reactions. For spherical object of radius r the value of the diffusion coefficient can be theoretically derived from the well-known Stokes-Einstein relation [53] which couples the kinetic energy associated to the thermal agitation of particles and the viscous drag the particle experiences while moving within a viscous fluid. For objects of approximately spherical shape (e.g. many type of molecules, colloids or bacteria) for which the radius is known, several methods have been developed in the past decades to measure the value of D based either on the microscopic (individual motion) or macroscopic (concentration distribution) properties of the process.

However, these methods are either based on indirect measurements, such as dynamic light scattering (DLS), or requires prior knowledge on either the host fluid or the molecule of interest, such as Taylor dispersion based measurements. To overcome this, we developed a novel method to measure the value of the diffusion coefficient based on the direct observation of the substance mass-transfer. Within a flow cell of simple geometry, a sharp front is established between the tracer of interest and a blank solution; the dissolved or suspended substance diffuses transversly to the cell main flow direction and the concentration profile of the front is solution of diffusion equation. The value of D is determined by fitting that solution, that depends on the value of D (to be determined) and the initial condition (known), to the measured profile.

Mixing by porous media

To investigate confined-limited mixing of displacing front within an heterogeneous porous system, we developed a novel experimental set-up to visualize and measure the concentration field at the pore scale, also capturing tens of average pores along the longitudinal and transverse direction to investigate the role of heterogeneity. The images obtained from time-lapse video-microscopy demonstrated the persisting non-well mixed conditions prevailing within pore throats, even at relatively low Pe number (here $Pe = 15$) and for all observation times. Considering the distribution of concentration values through their PDF, we observed that the distribution deviates from the one predicted by a lamellar model developed for a Darcy scale, continuous, system.

As already demonstrated at Darcy scale, where the individual pores are not resolved, we observe that macroscopic measurements of displacement and spreading such as longitudinal projection of concentration field and early times BTC can be well predicted by the classical advection dispersion models. Observations of transport dynamics for longer times, i.e. the BTC for times much larger than the pore volume time scale, are expected to deviate from this classical advection-dispersion framework, since small concentrations fluctuations, associated to flow heterogeneity, would become important (as we verified by means of numerical simulations).

Considering as diagnostic quantity for mixing dynamics the concentration PDF, our measurements show that at pore scale, the presence of solid and impermeable boundaries, the grains, triggers a different mixing dynamics that affect the concentration distribution statistics which deviates from what it would be expected for an invading sharp front within a continuous non-confined domain: from scaling as c^{-1} to $c^{-3/4}$. this key observation indicates that the processes of diffusion, stretch-

ing and merging of lamellas are controlled by fundamentally different kinematics associated to the confinement conditions.

To go even further and assess the impact of the host medium heterogeneity (i.e. the pore throats and grain size distribution), we used two-dimensional flow and transport numerical simulations and particle tracking within the same porous geometry as the one used in our laboratory experiment. In particular, particle tracking simulations allowed us to analyze the Lagrangian stretching and front elongation kinematics of the invading concentration front. We also performed the same numerical investigation (flow, solute transport, particle tracking and Lagrangian statistics) on a Darcy scale field characterized by a similar heterogneity (i.e. broad range of velocity and same ratio between the heterogeneity correlation length λ and the medium size L).

The simulations showed that, while at the Darcy scale the transported solute concentration PDF scales as c^{-1} at all times (as it would be predicted by the lamellar model), at pore scale our experimental observations were confirmed: the concentration PDF only initially scales as c^{-1} to dynamically change scaling towards $c^{-3/4}$. Similar results are obtained for the concentration gradients PDF.

Moreover, the stretching statistics of the fully resolved, and confined, porous system resulted to be controlled by the grain size distribution. We understand this observing that the fluid particles are moving with very similar and slow velocity when they approach a grain. Behind it the moving particles experience the strong and homogeneous elongation that characterizes the tail of the observed statistics. Since in the middle of a pore the fluid velocity is close to the average velocity $\overline{u}$ and close to a grain the velocity approaches zero, the stretching intensity behind a grain is set by the grain size R itself: along that distance the fluid particles get separated because on the one hand they are pinned, on the other hand they get pulled at average velocity $\overline{u}$. This is a fundamentally different stretching mechanism with respect to Darcy scale, continuous fields, there fluid elements are not pinned since their velocity can be very small, but not zero.

Implication for mixing at larger scale

In the context of reactive transport there is an important challenge in predicting where, and how quickly, biological or chemical reactions will take place; depending on the physical heterogeneity of the host medium structure and the complex flow pattern it triggers, as well as on the wide temporal scale over which reactions happen [113]. In order to react, chemical species must be brought in the

vicinity of each other by mixing, therefore as already argued by several studies [77, 25, 79], careful description of mixing mechanisms at the scale at which reactions actually occur (for porous medium it is the pore-scale) is necessary to successfully model mixing-driven reactions. It is in this framework that the results presented in this work could contribute to the development of mixing models that reflects the confining nature of porous media. We showed that diffusion, which ultimately mix solutes, is affected by confinement in its dynamics and time scale.

The authors of a recent work [114] carried a study on landfill leachate, considering a constant (steady state) flux of leachate input in the subsurface: they aim to monitor the degradation of a wide range of chemical species considered as pollutant for groundwater resources such as organic or chlorinated compounds. They built a conceptual model predicting the vertical concentration profile of each species of interest for different phase of the degradation process. The transport and reaction model used in this context is based on bulk quantities of soil properties and consider averaged concentration values. It would be relevant to compare and calibrate such a model with one considering a distribution of soil properties and thus concentration values including mixing mechanisms observed in confined conditions. How degradation time scale is affected and how wide is the range of actual concentrations, compared to the predicted average, is still an open question.

Another extensively studied mixing limited reaction phenomenon in porous media is the transformation of carbon (C) and nitrate (N) by microorganisms in the hyporehic zone (where stream water and groundwater mix). In [115] the authors developed a model based on one-dimensional advection-dispersion reaction equation in order to asses the role played by different downstream sections of the stream as a source or a sink of nitrate, whose parameters control the biochemical processes involving C and N. The model, then, provides concentration value of different species along the stream allowing to asses which section acts as a sink or a source of nitrate. The reaction rates considered are measured in well-mixed conditions, implying that all microorganisms are exposed to the same concentration of C or N. However, in a more realistic scenario concentration gradients are present at the sub pore-scale modifying the dynamics and spatial distribution of biomass which could ultimately modify both reaction rates values and spatial pattern of product distribution. The hyporehic zone is a typical confined environment where the solid matrix hosts biomass growth whose development is intrinsically linked to the presence of local concentration gradients. In order to approach an accurate prediction of transport and reaction dynamics by microorganisms it is essential to describe the fundamental mechanisms that drive mixing at the microscale not only taking into account the heterogeneity of the flow field but also the confined nature of the host medium

structure.

In both above mentioned studies [114, 115] reactions take place at the interface between two fluid bodies (contaminant plume and groundwater or ground and stream water) containing different solutes or biomass concentration which mix along the direction transverse to the main flow. Numerous studies [56, 116, 71, 117, 118] tackled this problem as it is a paradigmatic configuration of many natural or engineering phenomena. The approach is often to determine a transverse dispersion coefficient based on concentration profiles from a conservative tracer simulation [116] or by considering vertically (in the direction transverse to the flow) integrated concentration profile of reactive transport simulation at the pore scale [56]. In both cases pores are considered well-mixed and the confined nature of the host matrix is neglected. In [71] the authors study transverse mixing at the pore-scale using a homogeneous distribution of solid obstacles with an ellipse shape. They showed that the orientation of the ellipse (perpendicular or aligned with the flow) impacts the amount of product formed. In particular more product was formed in the configuration where the solid obstacles are perpendicular to the flow. One of their major result is that mixing is enhanced due to the flow focusing taking place as the streamlines are squeezed in the narrower pores found in the transverse direction, which is not the case when the solid obstacles are positioned aligned with the flow, leading to a higher product formation. They argue that the controlling parameter for this mechanism to occur is the alternation of flow focusing and expansion as fluid is transported through narrow and large pores. This is a very interesting scenario in which confinement could play a role, in this case the mixing time is defined by the diffusive time between two streamlines [113] a distance that decreases as the streamlines are squeezed. However, our results showed that within a pore the diffusive mixing time is different if we consider no-flux boundary conditions. **Integrating the solution of confined diffusion in such a model could lead to a more accurate description of transverse mixing.**

As illustrated by the studies presented above, the models currently used to describe reactive transport are based on the assumption that the concentration within pores are well-mixed and they do not consider the presence of solid boundaries. Within the framework of the lamellar mixing model described in Ch.1, small scale flow heterogeneity is taken into consideration and, thus, non well-mixed conditions. However, the consequences of the presence of the solid grains and the no-flux and no-flow boundary condition imposed on mass flux and fluid flow were up to now unexplored. **With the present work we propose a novel perspective to approach the mixing problem, moving a step forward towards a more realistic description of solute transport, mixing and reaction. In**

particular, we believe that these results will impact the development of novel reactive transport models, where the finite and limited size of pores affect the prediction of reaction rates, from column to field scale.

Perspectives

We demonstrated the role played by confinement i) on diffusion-limited mixing and ii) stretching dynamics observing iii) their impact on the mixing dynamics. An important next step will be to assess, beside these fundamental mechanisms, the process of lamellas coalescence within the pore space. Then, it will be possible to further extend the lamellar model to porous media explicitly taking into account their discrete nature.

In the part of this thesis that considers also advection with microfluidics experiments, we have not discussed any mixing diagnostic quantity based on concentration gradients, such as their PDF or the scalar dissipation rate. This is due to the technical difficulties to distinguish the physically meaningful concentration fluctuations from the electronic noise of the detection camera, that, even for the forefront technology, cannot be neglected. As a perspective, it would be very useful to combine numerical methods to smooth the acquired data, to remove the contribution of the experimental noise while respecting the role played by the walls of the solid grains.

Bibliography

[1] J. Grotzinger and T. Jordan. *Understanding Earth*. W. H. Freeman and compagny, New York, 2010.

[2] J. Bear. *Dynamics of Fluids in Porous Media*. Elsevier, New York, 1972.

[3] L. W. Mays. *Water resources engineering*. Wiley, 2011.

[4] R. A. Freeze and J. A. Cherry. *Groundwater*. Prentice Hall, 1979.

[5] G. M. Masters and W. P. Ela. *Introduction to environmental engineering and science*. Pearson international edition, 2008.

[6] F. Casini and G. M. B. Viggiani. Breakage of an artificial crushable material under loading. *Granular Matter*, 15:661–673, 2013.

[7] P. de Anna, T. Le Borgne, M. Dentz, A. Tartakovsky, D. Bolster, and P. Davy. Flow intermittency, dispersion and correlated continuous time random walks in porous media. *Phys. Rev. Lett.*, 101:184502, 2013.

[8] W. P. Ball, C. H. Buehler, T. C. Harmon, D. M. Mackay, and P. V. Roberts. Characterization of a sandy aquifer material at the grain scale. *J. Contam. Hydrol.*, 5(3):253–295, 1990.

[9] M. B. Hay, D. L. Stoliker, J. A. Davis, and J. M. Zachara. Characterization of the intragranular water regime within subsurface sediments: Pore volume, surface area, and mass transfer limitations. *Wat. Resour. Res.*, 47:W10531, 2011.

[10] W. W. Wood, Kraemer T. F., and P. P. Hearn Jr. Intragranular diffusion: An important mechanism influencing solute transport in clastic aquifers? *Science*, 247:1569–1572, 1990.

[11] J. Jimenez. Oceanic turbulence at millimeter scales. *Sci. Mar.*, 61, 1997.

[12] M. J. Blunt, B. Bijeljic, H. Dong, O. Gharbi, S. Iglauer, P. Mostaghimi, A. Paluszny, and C. Pentland. Pore-scale imaging and modelling. *Adv. Water Resour.*, 51:97–216, 2013.

[13] R. Rusconi, M. Garren, and R. Stocker. Microfluidics expanding the frontiers of microbial ecology. *Annu. Rev. of Biophys.*, in 43:65, 2014.

[14] B. Zhao, C. W. MacMinn, and R. Juanes. Wettability control on multiphase flow in patterned microfluidics. *Proc. Natl. Acad. Sci*, 113:10251–10256, 2016.

[15] P. de Anna, Y. Yawata, R. Stocker, and R. Juanes. Chemotaxis and front chemical gradients shape microbial dispersion in porous media flows. *Nat. Phys.*, 2020.

[16] M. Icardi, G. Boccardo, D. L. Marchisio, T. Tosco, and R. Sethi. Pore-scale simulation of fluid flow and solute dispersion in three-dimensional porous media. *Phys. Rev. E*, 90:013032, 2014.

[17] P. K. Kang, P. de Anna, J. P. Nunes, B. Bijeljic, M. J. Blunt, and R. Juanes. Pore-scale intermittent velocity structure underpinning anomalous transport through 3-D porous media. *Geophys. Res. Lett.*, 41(17):6184–6190, 2014.

[18] M. Holzner, V. L. Morales, M. Willmann, and M. Dentz. Intermittent lagrangian velocities and accelerations in three-dimensional porous medium flow. *Phys. Rev. E*, 92:013015, 2015.

[19] W. P. Ball, C. H. Buehler, T. C. Harmon, D. M. Mackay, and P. V. Roberts. Lagrangian analysis of nonreactive pollutant dispersion in porous media by means of the particle image velocimetry technique. *Wat. Resour. Res.*, 32:2329–2343, 1996.

[20] S. S. Datta, H. Chiang, T. S. Ramakrishnan, and D. A. Weitz. Spatial fluctuations of fluid velocities in flow through a three-dimensional porous medium. *Phys. Rev. Lett.*, 111:064501, 2013.

[21] P. de Anna, B. Quaife, G. Biros, and R. Juanes. Prediction of velocity distribution from pore structure in simple porous media. *Phys. Rev. Fluids*, 2:124103, 2017.

[22] T. Le Borgne, M. Dentz, and E. Villermaux. The lamellar description of mixing in porous media. *J. Fluid Mech.*, 770:458–498, 2015.

[23] C. Dorn, N. Linde, T. Le Borgne, O. Bour, and M Klepikova. Inferring transport characteristics in a fractured rock aquifer by combining single-hole gpr reflection monitoring and tracer test data. *Water Resour. Res.*, 48:W11521, 2012.

[24] D. Jougnot, J. Jiménez-Martínez, R. Legendre, T. Le Borgne, Y. Méheust, and N. Linde. Impact of small-scale saline tracer heterogeneity on electrical resistivity monitoring in fully and partially saturated porous media: insights from geoelectrical milli-fluidic experiments. *Adv. Water Resour.*, 113:295–309, 2012.

[25] C. M. Gramling, C. F. Harvey, and L. C. Meigs. Reactive transport in porous media: A comparison of model prediction with laboratory visualization. *Env. Sci. and Tech.*, 36(11), 2002.

[26] F. Miele, P. de Anna, and M. Dentz. Stochastic model for filtration by porous materials. *Phys. Rev. Fluids*, 4:094101, 2019.

[27] M. E. McClain, E. W. Boyer, C. L. Dent, S. E. Gergel, N. B. Grimm, P. M. Groffman, S. C. Hart, J. W. Harvey, C. A. Johnston, E. Mayorga, W.H. McDowell, and G. Pinay. Biogeochemical hot spots and hot moments at the interface of terrestrial and aquatic ecosystems. *Ecosystems*, 6:301–312, 2003.

[28] D. Scheidweiler, F. Miele, H. Peter, T. J. Battin, and P. de Anna. Trait-specific dispersal of bacteria in heterogeneous porous environments: from pore to porous medium scale. *J. R. Soc. Interface.*, 17:20200046, 2020.

[29] D. Scheidweiler, H. Peter, P. Pramateftaki, P de Anna, and T. J. Battin. Unraveling the biophysical underpinnings to the success of multispecies biofilms in porous environments. 13(7):1700–1710, 2019.

[30] L. Cueto-Felgueroso, M. J. Suarez-Navarro, X. Fu, and R. Juanes. Numerical simulation of unstable preferential flow during water infiltration into heterogeneous dry soil. *Water*, 12(3), 2020.

[31] D.R. Nielsen, M.T. van Genuchten, and J.W. Biggar. Water flow and solute transport processes in the unsaturated zone. *Water Resour. Res.*, 22:89S–108S, 1986.

[32] L. Cueto-Felgueroso, M. J. Suarez-Navarro, X. Fu, and R. Juanes. Interplay between fingering instabilities and initial soil moisture in solute transport through the vadose zone. *Water*, 12(3), 2020.

[33] B. Jha, L. Cueto-Felgueroso, and Juanes R. Fluid mixing from viscous fingering. *Phys. Rev. Lett.*, 106:194502, 2011.

[34] B. X. Primkulov, A. A. Pahlavan, X. Fu, B. Zhao, C. W. MacMinn, and R. Juanes. Signatures of fluid fluid displacement in porous media: wettability, patterns and pressures. *J. Fluid Mech.*, 875:R4, 2019.

[35] J. Jimenez-Martinez, P. de Anna, H. Tabuteau, R. Turuban, T. Le Borgne, and Y. Méheust. Pore-scale mechanisms for the enhancement of mixing in unsaturated porous media and implications for chemical reactions. *Geophys. Res. Lett.*, 42:5316–5324, 2015.

[36] X. Xiaojing Fua, J. Jimenez-Martinez, T. P. Nguyend, J. W. Careyd, H. Viswanathand, L. Cueto-Felguerosof, and R. Juanes. Crustal fingering facilitates free-gas methane migration through the hydrate stability zone. *PNAS*, 117:31660–31664, 2020.

[37] C. W. MacMinn and R. Juanes. Buoyant currents arrested by convective dissolution. *Geophys. Res. Lett.*, 40:2017–2022, 2013.

[38] C. W. MacMinn, M. L. Szulczewski, and R. Juanes. CO2 migration in saline aquifers. Part 2. Capillary and solubility trapping. *J. Fluid Mech.*, 688:321–351, 2011.

[39] H. Darcy. *Les fontaines publiques de la ville de Dijon: exposition et application des principes à suivre et des formules à employer dans les questions de distribution d'eau.* Victor Dalmont, Paris, 1856.

[40] L. A. Dillard and M. Blunt. Development of a pore network simulation model to study non aqueous phase liquid dissolution. *Wat. Resour. Res.*, 36:439–454, 2000.

[41] A. Shakas, N. Linde, T. Le Borgne, and O. Bour. Probabilistic inference of fracture-scale flow paths and aperture distribution from hydrogeophysically-monitored tracer tests. *J. Hydrol.*, 567:305–319, 2018.

[42] O. A. Cirpka, A Olsson, Q. Ju, A. Md. Ragman, and P. Grathwohl. Determination of transverse dispersion coefficients from reactive plume lengths. *Ground water*, 44(2):212–221, 2006.

[43] P.K. Kang, T. LeBorgne, M. Dentz, O. Bour, and R. Juanes. Impact of velocity correlation and distribution on transport in fractured media: Field evidence and theoretical model. *Water Resour. Res.*, 51:940–959, 2014.

[44] M. Flury, H. Flühler, W. A. Jury, and J. Leuenberger. Susceptibility of soils to preferential flow of water: a field study. *Water Resour. Res.*, 30:1945–1954, 1994.

[45] I.E. Forrer, A. Papritz, R. Kasteel, H. Flühler, and D. Luca. Quantifying dye tracers in soil profiles by image processing. *Eur. J. Soil Sci.*, 51:313–322, 2000.

[46] P. W. van der Pas. The discovery of the brownian motion. *Scientiarum Historia*, 13:27–35, 1971.

[47] A. Einstein. Über die von dermolekularkinetischen Theorie der Wärme geforderte Bewegung von in ruhenden Flüssigkeiten suspendierten Teilchen. *Ann. Phys.*, 322:549–560, 1905.

[48] M. von Smoluchowski. Zur kinetischen Theorie der Brownschen Molekularbewegung und der Suspensionen. *Ann. Phys.*, 21:757–780, 1906.

[49] W. Sutherland. A dynamical theory of diffusion for non-electrolytes and the molecular mass of albumin. *Phil. Mag. S.*, 9:781–785, 1905.

[50] H. C. Berg. *Random walks in biology*. Princeton University Press, 1993.

[51] N.G. van Kampen. *Stochastic Processes in Physics and Chemistry*. Elsevier, Amsterdam, third edition, 2007.

[52] D. M. Tartakovsky and M. Dentz. Diffusion in porous media: Phenomena and mechanisms. *Transp. Porous Media*, 130:105–127, 2019.

[53] Frederik Reif. *Fundamentals of statistical and thermal physics*. Mcgraw-Hill Compagny, 1985.

[54] S. B. Pope. *Turbulent Flows*. Cambridge University Press, New York, 2000.

[55] O. A. Cirpka, E. O. Frind, and R. Helmig. Numerical simulation of biodegradation controlled by transverse mixing. *J. Contam. Hydrol.*, 40:159–182, 1999.

[56] C. Knutson, A. Valocchi, and C. Werth. Comparison of continuum and pore-scale models of nutrient biodegradation under transverse mixing conditions. *Adv. Water Resour*, 30:1421–1431, 2007.

[57] A. Boisson, P. de Anna, O. Bour, T. Le Borgne, T. Labasque, and L. Aquilina. Reaction chain modeling of denitrification reactions during a push-pull test. *J. Contaminant Hydrol.*, 148:1–11, 2013.

[58] P. G. Cook, D. K. Solomon, W. E. Sanford, E. Busenberg, L. N. Plummer, and R. J. Poreda. Inferring shallow groundwater flow in saprolite and fractured rock using environmental tracers. *Wat. Resour. Res.*, 32(6):1501–1509, 1996.

[59] G. S. Weissmann, Y. Zhang, E. M. LaBolle, and G. E. Fogg. Dispersion of groundwater age in an alluvial aquifer system. *Wat. Resour. Res.*, 38(10):1198, 2002.

[60] B. B. Dykaar and P. K. Kitanidis. Macrotransport of a biologically reacting solute through porous media. *Wat. Resour. Res.*, 32(2):307–320, 1996.

[61] J.M. Ottino. *The kinematics of mixing: stretching, chaos, and transport*. Cambridge University Press, Cambridge, UK, 1989.

[62] J. Duplat, C. Innocenti, and E. Villermaux. A nonsequential turbulent mixing process. *Physics of Fluids*, 22(3):035104, 2010.

[63] T. Le Borgne, M. Dentz, and E. Villermaux. The lamellar description of mixing in porous media. *J. Fluid Mech.*, 770:458–498, 2014.

[64] Peter K. Kitanidis. The concept of the Dilution Index. *Water Resour. Res.*, 30(7):2011, 1994.

[65] M. Dentz, T. Le Borgne, A. Englert, and B. Bijeljic. Mixing, spreading and reaction in heterogeneous media: a brief review. *J. Contaminant Hydrol.*, 120-121:1–17, 2011.

[66] J. Duplat and E. Villermaux. Mixing by random stirring in confined mixtures. *J. Fluid Mech.*, 617:51–86, 2008.

[67] G. Taylor. Dispersion of soluble matter in solvent flowing slowly through a tube. *Proc. Roy. Soc. A*, 219, 1953.

[68] R. Aris. On the dispersion of a solute in a fluid flowing through a tube. *Proc. Roy. Soc. A*, 253:67–77, 1956.

[69] L. W. Gelhar, C. W. Kenneth, and R. Rehfeldt. A critical review of data on field-scale dispersion in aquifers. *Wat. Res. Resour.*, 28:1955–1974, 1992.

[70] V. Kapoor, L. W. Gelhar, and F. Miralles-Wilhelm. Bimolecular second-order reactions in spatially varying flows: Segregation induced scale-dependent transformation rates. *Water Resour. Res.*, 33(4):527, 1997.

[71] T. W. Willingham, C. J. Werth, and A. J. Valocchi. Evaluation of the effects of porous media structure on mixing-controlled reactions using pore-scale modeling and micromodel experiments. *Environ. Sci. Technol.*, 42(9):3185–3193, 2008.

[72] T. Le Borgne, M. Dentz, and E. Villermaux. Stretching, coalescence and mixing in porous media. *Phys. Rev. Lett.*, 110:204501, 2013.

[73] T. Le Borgne, D. Bolster, M. Dentz, P. de Anna, and A. Tartakovsky. Effective pore-scale dispersion upscaling with a correlated continuous time random walk approach. *Water Resour. Res.*, 47:W12538, 2011.

[74] T. Tel, A. Demoura, C. Grebogi, and G. Karolyi. Chemical and biological activity in open flows: A dynamical system approach.

[75] P. M. Oates. *Upscaling reactive transport in porous media: laboratory visualization and stochastic models*. PhD thesis, Massachusetts institute of technology, 2007.

[76] A. M. Tartakovsky, G. D. Tartakovsky, and T. D. Scheibe. Effects of incomplete mixing on multicomponent reactive transport. *Adv. Water Resour.*, 32(11), 2009.

[77] D. S. Raje and V. Kapoor. Experimental study of bimolecular reaction kinetics in porous media. *Environ. Sci. Technol.*, 34:1234–1239, 2000.

[78] P. De Anna, J. Jimenez-Martinez, H. Tabuteau, R. Turuban, T. Le Borgne, M. Derrien, and Y. Méheust. Mixing and reaction kinetics in poroous media: an experimental pore scale quantification. *Environ. Sci. Technol.*, 48:508–516, 2014.

[79] P. De Anna, J. Jimenez-Martinez, H. Tabuteau, R. Turuban, T. Le Borgne, M. Derrien, and Y. Méheust. Mixing and reaction kinetics in poroous media: an experimental pore scale quantification. *Environ. Sci. Technol.*, 48(13):508–516, 2014.

[80] W. Ranz. Applications of a stretch model to mixing, diffusion, and reaction in laminar and turbulent flows. *AIChE J.*, 25:41–47, 1979.

[81] P. Meunier and E. Villermaux. The diffusive strip method for scalar mixing in two dimensions. *J. Fluid. Mech*, 662:134–172, 2010.

[82] E. Villermaux. Mixing by porous media. *C. R. Mechaniques*, 340:933–943, 2012.

[83] T. Le Borgne, M. Dentz, D. Bolster, J. Carrera, J-R de Dreuzy, and P. Davy. Non-fickian mixing: Temporal evolution of the scalar dissipation rate in heterogeneous porous media. *Adv. in Water Resour.*, 33(12):1468–1475, 2010.

[84] E. Villermaux. Mixing versus stiring. *Annu. Rev. Fluid Mech.*, 51:245–273, 2019.

[85] J. Happel and H. Brenner. *Low Reynolds Number Hydrodynamics*. Martinus Nijhoff Publishers, 1983.

[86] E. Villermaux and J. Duplat. Mixing is an aggregation process. *C. R. Mecaniques*, 331, 2003.

[87] J. J. Hidalgo, L. Cueto-Felgueroso, and R. Juanes. Scaling of convective mixing in porous media. *Phys. Rev. Lett.*, 109:264503, 2012.

[88] B. Jha, L. Cueto-Felgueroso, and R. Juanes. Synergetic fluid mixing from viscous fingering and alternating injection. *Phys. Rev. Lett.*, 111:144501, 2013.

[89] S. Whitaker. *The Method of Volume Averaging*. Springer, New York, 1999.

[90] E. Villermaux and C. Innocenti. On the geometry of turbulent mixing. *J. Fluid Mech*, 393:123–147, 1999.

[91] A. Fick. Über Diffusion. *Ann. Phys*, 170:59–86, 1855.

[92] J. Stetefeld, S. A. McKenna, and T. R. Patel. Dynamic light scattering: a practical guide and applications in biomedical sciences. *Phys. Rev. Lett.*, 8(4):409–427, 2016.

[93] A. Alizahed, C.N. De Castro, and W. Wakeham. The theory of the taylor dispersion technique for liquid diffusivity measurements. *Int. J. Thermophys.*, 1:243–284, 1980.

[94] A. C. Ouano. Diffusion in liquid systems. I. A simple and fast method of measuring diffusion constants. *Ind. Eng. Chem. Fundam.*, 11(2):268–271, 1972.

[95] J. H. Northrop and M. L. Anson. A method for the determination of diffusion constants and the calculation of the radius and weight of the hemoglobin molecule. *J. Gen. Physiol.*, 12(543):543–554, 1928.

[96] A.R Gordon. The diaphragm cell method of measuring diffusion. *Ann. N.Y Acad. Sci.*, 46:285–308, 1945.

[97] J. Lozar, C. Laguerie, and J.P Couderc. Diffusivité de l'acide benzoïque dans l'eau: influence de la température. *The canadian journal of chemical engineering*, 53:200–203, 1975.

[98] Bouguer Pierre. *Essai d'optique sur la gradation de la lumière*. Claude Jombert, Paris, 1729.

[99] J. J. Kipling and R. B. Wilson. Absorption of methylene blue in the determination of surface areas. *J. appl. Chem*, 10:109–113, 1960.

[100] P. T. Hang and G. W. Brindley. Methylene blue absorption by clay minerals. determination of surface areas and cation exchange capacities. *Clay and Clay Minerals*, 18:203–212, 1970.

[101] R. K. Taylor. Cation exchange in clays and mudrocks by methylene blue. *J. Chem. tech. Biotechnol.*, 35A:195–207, 1985.

[102] M. Hamada, P. de Anna, and L. Cueto-Felgueroso. Diffusion limited mixing in confined media. *Phys. Rev. Fluids*, 5:124502, 2020.

[103] J. Heyman, D. R. Lester, R. Turuban, Y. Méheust, and T. Le Borgne. Stretching and folding sustain microscale chemical gradients in porous media. *PNAS*, 111(24):13359–13365, 2020.

[104] D. B. Weibel, W. R. DiLuzio, and G. M. Whitesides. Microfabrication meets microbiology. *Nature Rev. Microbiol.*, 5:208–218, 2007.

[105] J. R. Taylor. *An Introduction to Error Analysis*. University Science Books, 1982.

[106] F. Miele. *Filtration by heterogeneous porous materials*. PhD thesis, University of Lausanne, 2020.

[107] J. R. Shewchuk. Delaunay refinement algorithms for triangular mesh generation. *Comput. Geom.*, 22(1):21–74, 2002.

[108] M. J. Blunt et al. Pore-scale imaging and modelling. *Adv. Water Resour.*, 51:97–216, 2013.

[109] M. J. Blunt. Flow in porous media—pore network models and multiphase flow. *Curr. Opin. Colloid Interface Sci.*, 6:197–207, 2001.

[110] M Dentz, M. Icardi, and J. J. Hidalgo. Mechanism of dispersion in a porous medium. *J. Fluid Mech.*, 841:851–882, 2018.

[111] J. Happel and H. Brenner. *Low Reynolds Number Hydrodynamics*. Martinus Nijhoff Publishers, 1983.

[112] P.V. Danckwerts. The effect of incomplete mixing on homogeneous reactions. *Chem. Eng. Sci.*, 8:93–102, 1958.

[113] A. J. Valocchi, D. Bolster, and C. J. Werth. Mixing-limited reactions in porous media. *Transp Porous Media*, 130:157–182, 2018.

[114] P. L. Bjerg, N. Tuxen, L. A. Reitzel, H. Albrechtsen, and P. Kjeldsen. Natural attenuation processes in landfill leachate plumes at three danish sites. *Groundwater*, 49(5):688–705, 2011.

[115] J. P. Zarnetske, R. Haggerty, S. M. Wondzell, V. A. Bokil, and R. González-Pinzón. Coupled transport and reaction kinetics control the nitrate source-sink function of hyporheic zones. *Water Resour. Res.*, 48:W11508, 2012.

[116] R. C. Ram C. Acharya, A. J. Valocchi, C. J. Werth, and T. W. Willingham. Pore-scale simulation of dispersion and reaction along a transverse mixing zone in two-dimensional porous media. *Water Resour. Res.*, 43:W10435, 2007.

[117] M. Roll, C. Eberhardt, G. Chiogna, O. A. Cirpka, and P. Grathwohl. Enhancement of dilution and transverse reactive mixing in porous media: Experiments and model-based interpretation. *J. Contam. Hydrol.*, 110:130–142, 2009.

[118] T. Willingham, C. Zhang, C. J. Werth, A. J. Valocchi, M. Oostrom, and T. W. Wietsma. Using dispersivity values to quantify the effects of pore-scale flow focusing on enhanced reaction along a transverse mixing zone. *Adv. Water Resour.*, 33:525–535, 2010.